UNIVERSIDADE FEDERAL DO ESPÍRITO SANTO
CENTRO TECNOLÓGICO

PROGRAMA DE PÓS-GRADUAÇÃO EM ENGENHARIA AMBIENTAL

CRISTINA LIMA DE MORAIS

PARTICLES EMISSION AND TRANSPORT DUE TO WIND EROSION ON BEDS AND STOCKPILES: LOCAL AND NON-LOCAL ASPECTS OF TURBULENT FLUID FLOW DYNAMICS.

Vitória
May 2024

CRISTINA LIMA DE MORAIS

PARTICLES EMISSION AND TRANSPORT DUE TO WIND EROSION ON BEDS AND STOCKPILES: LOCAL AND NON-LOCAL ASPECTS OF TURBULENT FLUID FLOW DYNAMICS.

Thesis submitted to Programa de Pós-Graduação em Engenharia Ambiental of Centro Tecnológico da Universidade Federal do Espírito Santo, for the doctoral degree in Environmental Engineering.

Supervisor: Prof. Jane Meri Santos, PhD.

Co-supervisors: Prof. Bruno Furieri, PhD.
Prof. Maria Clara S. Ferreira, PhD.
Prof. Jean-Luc Harion, PhD.

Vitória
May 2024

Ficha catalográfica disponibilizada pelo Sistema Integrado de Bibliotecas - SIBI/UFES e elaborada pelo autor

---

M827p

Morais, Cristina Lima de, 1992-
Particles emission and transport due to wind erosion on beds and stockpiles : Local and non-local aspects of turbulent fluid flow dynamics / Cristina Lima de Morais. - 2024.
152 p. : il.

Orientadora: Jane Meri Santos.
Coorientadores: Bruno Furieri, Maria Clara S. Ferreira, Jean Luc Harion.
Tese (Doutorado em Engenharia Ambiental) - Universidade Federal do Espírito Santo, Centro Tecnológico.

I. Santos, Jane Meri. II. Furieri, Bruno. III. Ferreira, Maria Clara S.. IV. Harion, Jean-Luc. V. Universidade Federal do Espírito Santo. Centro Tecnológico. VI. Título.

CDU: 628

UNIVERSIDADE FEDERAL DO ESPÍRITO SANTO
CENTRO TECNOLÓGICO
PROGRAMA DE PÓS-GRADUAÇÃO EM ENGENHARIA AMBIENTAL

Particle emission and transport due to wind erosion on beds and stockpiles: local and non-local aspects of turbulent fluid flow dynamics

Cristina Lima de Morais

Banca Examinadora:

Prof.ª Dr.ª Jane Meri Santos
Orientadora – PPGEA/CT/UFES

Prof. Dr. Bruno Furieri
Coorientador – PPGEA/CT/UFES

Prof.ª Dr.ª Maria Clara Schuwartz Ferreira
Coorientadora – IFES/Vitória

Prof. Dr. Jean-Luc Harion
Coorientador – IMT Nord Europe

Prof.ª Dr.ª Taciana Toledo de Almeida Albuquerque
Examinadora Interno – PPGEA/CT/UFES

Prof. Dr. Neyval Costa Reis Júnior
Examinador Interno – PPGEA/CT/UFES

Prof.ª Dr.ª Angela Ourivio Nieckele
Examinador Externo – DEM/PUC-Rio

Prof. Dr. Rafael Sartim
Examinador Externo – Centro de Pesquisa e desenvolvimento da ArcelorMittal

ELISA VALENTIM GOULART
Coordenadora do Programa de Pós-Graduação em Engenharia Ambiental
UNIVERSIDADE FEDERAL DO ESPÍRITO SANTO

Vitória/ES, 03 de maio de 2024

ACKNOWLEDGEMENTS

A Deus, meu pai, O Senhor da minha vida. Sem Ele eu não estaria viva e nem poderia escrever esse texto nesse momento. Deus, por intermédio de Jesus Cristo, mudou a minha história, me fez superar todas as dificuldades, usou pessoas e situações para me socorrer quando eu estava afundando. Deus me surpreendeu de formas que não tenho palavras para descrever. Como diz o ditado: “Do crente ao ateu, ninguém explica Deus!”. Logo, eu na minha insignificância, não seria a primeira a explicar o que Deus é nem o que Ele significa para mim. Dedico toda minha gratidão a Ele por tudo que já se foi e por tudo que está por vir. Uma vez ouvi de uma pessoa uma frase que nunca mais me deixou: “A fé em Deus humilha todas as circunstâncias”. E o que mais eu tive na vida foram “circunstâncias”. Por isso, muito obrigada meu Deus!

À minha ilustre mãe, Ivanete, meu grande amor. Tem uma frase de Carl Sagan que já foi reescrita, adaptada para novelas, mas eu deixo aqui a minha versão: Diante da vastidão do tempo e da imensidão do universo, é um imenso prazer para mim dividir um planeta e uma época com você sendo a minha mãe! Tudo, exatamente tudo, inclusive essa tese, começou quando Deus me fez nascer sua filha. Foi você que disse que só estudando eu conseguiria mudar a minha vida. E assim foi. Te amo desde sempre!

Às minhas queridas amigas Kézia, Thaís e Karol, nas quais eu sempre encontrei apoio e um ombro para chorar minhas lágrimas e para compartilhar minhas alegrias desde quando as conheci. Vocês são um tesouro para mim. Vocês são vidas que eu faço questão na minha vida. Em meio a falsidades mascaradas de amizade que eu encontrei nos últimos anos, vocês foram âncoras para eu me agarrar e não sair por aí divagando, achando que não era possível achar nada bom nas pessoas. O afeto sincero de vocês significa muito para mim.

À Professora Jane Meri Santos por me permitir ter seguido com ela todos esses anos. Uma grande pesquisadora, uma referência nos estudos de qualidade do ar. Foi um prazer para mim ser sua aluna e ter tido a oportunidade de discutir várias questões com uma cientista do seu gabarito. Gostaria de dizer que você transmitiu a mim a centelha e o prazer do abstrato, da divagação que te é tão cara no trabalho científico. Às vezes não vemos essa centelha porque ora acende, ora apaga dentro de mim. Mas ela existe. Manter a centelha acesa é mais sobre mim do que sobre você. Só tenho gratidão. Você foi muitas vezes além da nossa relação profissional, teve empatia por mim e me ajudou sempre que teve oportunidade. Obrigada!

Ao Professor Bruno Furieri. Além de professor, foi de fato meu companheiro de dissertação e tese. Eu nunca vou conseguir retribuir tudo que ele fez por mim. Foram inúmeras horas de trabalho, reuniões, correções e escrita feitas em parceria. Eu cheguei até aqui não somente porque Bruno quis me ajudar. Mas porque ele fez questão. Ele se importou comigo e com meu trabalho. Isso não tem preço. É um ser humano de inteligência incomum, cujo pensamento vai além em qualquer situação. Foi uma honra para mim ser sua aluna. Obrigada por fazer parte da minha história. Obrigada por todas as oportunidades cujas portas você abriu para mim. Apesar dos laços sanguíneos nos limitarem, eu te considero um irmão.

À Professora Maria Clara pelo apoio, amizade e orientação desde o mestrado. Maria Clara é apelido. Na verdade, é Santa Maria Clara! Quando não se encontrava uma explicação para um problema, ao se recorrer a ela acontecia um milagre: ela mostrava cientificamente onde estavam as explicações para nossas dúvidas. Você foi essencial.

Ao professor Neyval Costa Reis Junior pelo grande entusiasmo demostrado ao contribuir com meu trabalho e me ajudar nas horas que eu precisei desde o período do mestrado. Obrigada por todo tempo que você investiu na minha tese através das longas reuniões que tivemos.

Ao professor Jean-Luc Harion do IMT Nord Europe pela grande contribuição para minha pesquisa e por ter me recebido na França e me orientado nos dois meses que fiquei lá. Pessoa mais querida e paciente não há.

Aos companheiros de laboratório Laize, Matheus, Andressa e João, que fizeram dos meus dias, dias mais felizes e da minha jornada, uma jornada mais leve. Eu moraria naquele laboratório se fosse requisito para encontrar vocês todos os dias.

À Dominique e à Alice, duas bebês que nasceram nesse período, filhas de pessoas maravilhosas. O mundo ficou melhor depois que vocês chegaram. O surgimento de novas vidas é lindo. Inspira, emana amor.

Aos demais colegas e colaboradores do PPGEA que contribuíram para que eu concluísse minha tese.

À CAPES, à FAPES e ao CNPQ pelo apoio financeiro ao programa de pós-graduação em Engenharia Ambiental da UFES.

À minha amada mãe, Ivanete de Souza Lima.

Aos meus amados gatos, Sara Jane, Nina Maria e Bruno.

Ao meu amado padrinho, Abner de Freitas Heringer (*in memoriam*).

Alegrem-se sempre.

Orem continuamente.

Deem graças em todas as circunstâncias,

pois esta é a vontade de Deus para vocês em Cristo Jesus.

(1Tessalonicenses 5:16-18)

ABSTRACT

This study aims to provide a comprehensive understanding of particle behavior in both local and non-local contexts. We analyze the influence of different configurations of successive stockpiles on the re-emission potential of particles from their surroundings using the USEPA model. This analysis is important for industries that store granular materials in open yards, as it helps to understand the impact of stockpile arrangements on particle emission. However, the USEPA model relies on an empirical equation and has gaps in its consideration of non-erodible particles and their effects on turbulent structures. Additionally, the friction velocity distribution used in the model is derived from previous RANS numerical simulations, which may not be the most accurate. Moving from a non-local to a local perspective, we assess the influence of non-erodible particles on the development of fluid flow structures at the particle level. We examine the role of turbulent structures in particle entrainment through LES simulations, which provide detailed information about the flow field. These simulations allowed us to generate probability density distributions of friction velocity for smooth and rough beds, which can be used to improve or develop more accurate environmental stochastic prediction models. Finally, we evaluate the similarity requirements of wind flow, particle entrainment, and particle transport in wind tunnel experiments to ensure they accurately represent real-scale scenarios. By addressing these similarity requirements, we discuss the conditions under which wind tunnel experiments can reliably simulate real conditions, which is essential for the future applicability of our findings.

Keywords: Particles emission. Particle beds. Granular Stockpiles. Large-Eddy Simulation. Similarity analysis.

RESUMO

Este estudo tem como objetivo proporcionar uma compreensão abrangente do comportamento de partículas levando em consideração aspectos locais e não locais. Analisamos a influência de diferentes configurações de pilhas sucessivas no potencial de reemissão de partículas de seus arredores usando o modelo USEPA. Esta análise é importante para indústrias que armazenam materiais granulares em pátios abertos, pois ajuda a entender o impacto das disposições das pilhas na emissão de partículas. No entanto, o modelo USEPA baseia-se em uma equação empírica e possui lacunas na consideração de partículas não-erodíveis e seus efeitos nas estruturas turbulentas. Além disso, a distribuição de velocidade de fricção usada no modelo é derivada de simulações numéricas RANS anteriores, que podem não proporcionar resultados mais precisos. Passando de uma perspectiva não local para uma local, avaliamos a influência de elementos não-erodíveis no desenvolvimento de estruturas turbulentas a nível de partículas. Examinamos o papel das estruturas turbulentas no entranhamento de partículas por meio de simulações LES, que fornecem informações detalhadas sobre o campo de escoamento. Essas simulações nos permitiram gerar distribuições de densidade de probabilidade da velocidade de fricção para leitos lisos e rugosos, que podem ser usadas para melhorar ou desenvolver modelos estocásticos mais precisos para estimativa de emissão de partículas. Finalmente, avaliamos os requisitos de similaridade do escoamento do vento, entranhamento de partículas e do transporte de partículas em experimentos em túnel de vento para garantir que representem cenários em escala real com precisão. Ao abordar esses requisitos de similaridade, discutimos as condições sob as quais experimentos em escala de túnel de vento podem simular de forma confiável condições reais, o que é essencial para a aplicabilidade futura de nossas descobertas.

Palavras-chave: Emissão de partículas. Leito de partículas. Pilhas de estocagem. Simulação de Grandes Escalas. Análise de similaridade.

LIST OF FIGURES

LIST OF TABLES

LIST OF SYMBOLS

Acronyms

CFD	Computational Fluid Dynamics
LES	Large Eddy Simulation
RANS	Reynolds averaged Navier-Stokes
SST	Shear-Stress Transport
USEPA	United States Environmental Protection Agency

Roman symbols

A, M, N	Numeric coefficients	
a	Slope of the line of the relationship between CR e H	
A	Domain cross-sectional area	m^2
A_{ij}	USEPA stockpile subareas	m^2
b	Rough element width	m
CR	Non-erodible particle cover rate	%
CR_i	Initial cover rate	%
d	Distance from nearest wall in $\mathrm{k}-\omega$ SST model	m
D	Particle diameter	m
D_{NE}	Diameter of non-erodible particles	m
E	Total emitted mass in the USEPA model	g
E_f	Mass emitted	kg
F_1, F_2	Mixing functions in $\mathrm{k}-\omega$ SST model	
F_a	Cohesion force	N
F_d	Drag force	N
F_l	Lifting force	N
F_g	Gravitational force	N
g	Gravitational force	m/s^2
h	Stockpile height	m
h_r	Rough element height	m
H	Eroded height	m
H_f	Final eroded height	m
k	Turbulent kinetic energy	m^2/s^2
K	USEPA particle size multiplier	
m	Raupach et al. (1993) model parameter	
$\dot{m}$	Mass flow at the domain entrance	kg/s
n_r	Number of rough elements	
N	Number of disturbances in the USEPA model	
p	Static pressure	Pa
P	USEPA model erosion potential	kg/m^2
$R"$	Friction velocity ratio from Raupach et al. (1993)	
R_{fric}	Friction velocity ratio	
R_{MIN}	Minimum value of $\mathrm{R_{fric}}$	
S_{bed}	Bea area	m^2

S_{ij}	Strain rate tensor	$1/s$
S_{floor}	Basal area of rough elements	m^2
$S_{frontal}$	Front area of rough elements	m^2
S_{θ,u^*}	Stockpiles subareas in Caliman model (2017)	m^2
T	Temperature	°C
u^*	Friction velocity	m/s
u_r^*	Mean friction velocity on an erodible surface under the influence of roughness	m/s
u_s^*	Mean friction velocity on a surface without the influence of roughness.	m/s
u_s	Surface velocity at 25 cm from the pile in the USEPA model	m/s
$u_{\boldsymbol{r}}$	Free stream wind velocity in USEPA model	m/s
u_t^*	Particle threshold friction velocity	m/s
u_{10}^+	Fastest velocity among USEPA model perturbations	m/s
U_∞	Free stream velocity	m/s
V_{bed}	Bed volume	m^3
V_{tot}	Total volume occupied by particles	m^3
x	Cartesian coordinates	
z	Vertical direction	

Greek symbols

$\alpha, \beta, \sigma_k, \sigma_\omega$	k − ω SST model constants	
$\alpha_1,\ \beta_1, \sigma_{k1}, \sigma_{\omega 1}$	k − ω SST model constants from k − ω model	
$\alpha_2,\ \beta_2, \sigma_{k2}, \sigma_{\omega 2}$	k − ω SST model constants from k − ε model	
α_{NE}	Mass fraction of non-erodible particles	%
β^*	Empirical constant of k − ω model	
γ	Surface energy that characterizes cohesion	kg/s^2
δ	Boundary layer height	m
ε	Kinetic energy dissipation	m^2/s^3
θ	Flow inclination angle	°
θ_p	Potential temperature	
λ	Density of rough elements	
μ	Dynamic viscosity	$N\ s/m^2$
μ_t	Turbulent viscosity	$N\ s/m^2$
ν	Kinematic viscosity	m^2/s^2
ξ	Angle of repose of a granular material	°
ρ	Fluid density	kg/m^3
ρ_{bed}	Bed density	kg/m^3
ρ_p	Particle density	kg/m^3
σ	Ratio between the basal area and the frontal area of the roughness elements in Raupach et al. (1993) model	
τ	Total shear stress	N/m^2
τ_z	Vertical component of shear stress	N/m^2
τ_{ij}	Stress tensor	N/m^2
$\tau_s^{"}$	Maximum shear stress on a surface without the presence of nonerodible elements	N/m^2

φ	Volume fraction	
ω	Specific turbulent dissipation rate	$1/s$

Subscript

i, j, k	Indexical notation
ref	Reference values

Superscript

$-$	Mean values, filtered values
$+, \sim$	Dimensionless values

CONTENTS

1. INTRODUCTION

Wind erosion is a significant natural process involving the movement of particles induced by wind forces. This complex phenomenon involves interactions between particles, fluid flow, surfaces, and between the particles themselves. Aerodynamic forces, primarily drag and lift created by wind flow, play a crucial role in moving particles. These forces are influenced by turbulent perturbations from the mean flow and can be described by the friction velocity, a characteristic parameter of the internal boundary layer linked to surface shear stress. On the other hand, gravity and cohesion forces significantly influence particle-surface and particle-particle interactions. The threshold friction velocity, which is strongly affected by particle size, represents the minimum friction velocity required to initiate particle movement. When the flow friction velocity at the surface is lower than the threshold friction velocity ($u^* < u_t^*$), particles remain on the surface; if the opposite occurs ($u^* > u_t^*$), particles are set in motion (Shao, 2008).

Wind erosion is a common issue on stockpiles of granular material in industrial plants. These stockpiles act as fugitive sources of particulate matter exposed to wind flow, contributing to atmospheric particulate matter concentrations. The dust emissions resulting from wind erosion, although seemingly insignificant in terms of material loss for industries, can lead to increased particulate concentrations in the atmosphere, resulting in loss of (Huang et al., 2009; Wu et al., 2005), soiling of surfaces (Tiwary and Colls, 2010), damage to vegetation (Farmer, 1993; Onder and Dursun, 2006), and risks to human health (An et al., 2018; Bové et al., 2019; Hadley et al., 2018; Miller, 2020; Seaton et al., 2020; Sigaux et al., 2019). Therefore, accurately estimating particulate matter emissions is essential for developing effective dust control policies and making informed decisions regarding environmental licensing.

Wind flowing over surfaces composed of loose material can transport particles for long distances or even to the near surroundings. How does airflow put particles in motion? How do particles behave according to their size, shape, chemical composition, and wind conditions? These are extremely important questions to the understanding of aeolian erosion. Although this natural process regards atmospheric emissions of particles that can cause an impact on human health, most work found in the literature concerns erosion of soil particles in the order of 0.2-30 mm, while particles of air pollution interest are in the order of 2.5-100 μm. A wind tunnel is a useful tool to simulate aeolian erosion and is very much used to model, at smaller scale, particles emission and their mode of transportation, allowing simulations in a controlled environment not possible in fields measurements, see for instance, the recent works of Marshall et al. (2021), Jiang et al. (2021), Jiang et al. (2022), Mina et al. (2022) and Zhang et al. (2022). However, despite these advantages, a small-scale study can compromise the reliable reproduction of the large-scale phenomena.

It is well known that to obtain full similarity between a phenomenon occurring on a reduced scale (model) and real scale (prototype), it is necessary to achieve geometric, kinematic, and dynamic similarities. Geometric similarity means that the model has the same shape and proportional dimensions as the prototype. Kinematic similarity states that the model and the prototype must develop similar fluid flow. Dynamic similarity indicates that the ratio of different forces acting on the fluid particles and boundary surfaces must be identical in both scales. Raffaele et al. (2021) discussed that studies on similarity requirements for wind tunnel simulation of aeolian erosion started many years ago with the efforts of several authors, mainly for snow drift (Strom et al., 1962; Snyder, 1972; Kind, 1976; Iversen, 1980; Anno, 1984; White, 1996). However, it is important to point out that geometric, kinematic, and dynamic similarities cannot be satisfied simultaneously if one is dealing with aeolian erosion (Aliabadi, 2018; Sherman, 2020; Raffaele et al., 2021). In addition, Reynolds number (Re) independence, approximately 10^5 (Kato and Hanafusa, 1996; Woodruff and Zingg, 1953), claimed as the condition in which turbulence is such that variations between the model and the prototype could be neglected is questionable. Chew et al. (2018) argued that only the Reynolds independence is not enough to guarantee the same behavior on prototype and model in a similar flow, since it seems that Re is highly influenced by the geometry considered. In general words, there would be different Reynolds number of independence for different cases. A major problem emerges for the geometric similarity of particles. For most scenarios concerning applications of air pollution interest, the particles used in wind tunnels should be extremely small to meet similarity to real scale which is even more difficult if erosion is occurring in stockpiles, for instance. This would lead to strong cohesive influences, a very complex phenomenon that might not be happening in real scale particles. Another issue is that working with very small particles leads to enormous technical difficulties, for instance, health and safety for those running the experiments and acquisition of appropriate particles in terms of size distribution and composition, if not to use the material of interest is an option. These are some of the reasons why studies on cohesion and hence, fine particles, are still very limited. Other important questions arise from the complexity of the turbulent flow itself.

Small particles, less than 10 μm in diameter, may remain in the atmosphere for days before being washed out by rain or impacted out into some obstacle, as vegetation or buildings. Therefore, industries and environmental control agencies need to estimate these emissions for the development of dust control policies and for environmental licensing considering the particle size distribution and the presence of non-erodible elements on wind erosion events. The most used model to estimate emissions due to wind erosion from stockpiles was proposed by the United States Environmental Protection Agency (USEPA, 2006a). Despite being developed based on experimental and field data, the model, however, has limitations. The model can underestimate emissions and has limited applicability to more specific scenarios. Only two shapes of stockpiles and three wind incidence angles are considered. In addition, the model does not consider the proportion of erodible and non-erodible particles in the mixture of granulated materials.

Many studies have used Computational Fluid Dynamics (CFD) to determine parameters used in the USEPA model to turn the model applicable to different scenarios regarding the shape of the pile and the direction of the incident wind using RANS (Reynolds Averaged Navier-Stokes) approach for turbulence modeling (Badr and Harion, 2007; Toraño et al., 2007; Diego et al., 2009; Turpin and Harion, 2010; Furieri et al., 2012; Derakhshani et al., 2013; Liu et al., 2018; Ferreira et al., 2019b). Others, like Romeo et al. (2017), proposed changes in the US EPA methodology by recommending a new approach to how gusts, that usually cause erosion, should be considered in the model to improve accuracy. Furieri (2012) proposed changes at the core of the US EPA emission model to include the effects of non-erodible particles, the larger ones, well-known in the literature for limiting the action of the wind by creating zones of low shear stress, not allowing the surrounding smaller particles to be emitted (Iversen et al., 1991; Neuman and Mckenna, 1995; López, 1998; Gillies et al., 2006; Turpin et al.,2010; Toure et al., 2011; Ferreira et al., 2013; Furieri et al., 2014; Smith et al., 2015; Swet and Katra, 2016; Mingari et al., 2017; Miri et al., 2017).

Caliman (2017) and Ferreira et al. (2019a) went further, developing a new emission model for both particle beds and stockpiles using a simple equation based on the emitted volume and in the estimation of the eroded height considering the effects of the non-erodible particles. Their model is an advance of the model proposed by Descamps et al. (2005) for beds and could be applied in several stockpile shapes and directions of the incident wind. The stockpile surface is divided into subareas with the same average shear stress and then the model is applied as if each subarea were a small, inclined bed of particles.

In Descamps et al. (2005) study, the erosion ceases only when the surface is completely covered by non-erodible particles, an assumption not realistic because of the low shear stress zones created by non-erodible particles. This is the gap solved in Ferreira et al. (2019a) model. However, Descamps et al. (2005) considered in their model the cohesive effects between small particles due to the cohesion forces using a probability density function (PDF), and the effects of the turbulent structures that can cause the emission of particles (Niño and Garcia, 1996; Séchet, 2000). These vortexes would appear with statistical spatial periodicities depending on the flow patterns and on the presence or not of particles. A deficiency of the model proposed by Descamps et al. (2005) comes from the hypothesis that the values of the mean spatial periodicities in the longitudinal and transversal directions of the flow obtained numerically by Jimenez and Moin (1991) for a smooth surface can be used for a surface composed of non-erodible particles (rough surface).

The complex association developed between the local turbulent air flow patterns and the presence of non-erodible roughness elements represents a challenge for wind erosion studies. Nevertheless, the development of turbulent structures and particle entrainment is central to particle emission models (Descamps et al., 2005; Ferreira et al., 2019b). This makes Large-Eddy Simulation (LES) an adequate approach to predict the turbulence flow structures and the shear stress (or friction velocity) distribution developed during the flow of the wind over rough surfaces in wind erosion events. The shear stress distribution plays an important role, as it is responsible for the movement of particles. In traditional approaches, the shear stress has been analyzed using deterministic models. Deterministic models in fluid mechanics are those that attempt to predict the behavior of the fluid with absolute certainty, based on well-defined physical equations. For example, the Navier-Stokes equations represent a deterministic model that describes fluid motion accurately but gives only averaged terms to help predicting particles emission behavior and quantification (Badr and Harion, 2005; Turpin and Harion, 2009; Turpin et al., 2010; Furieri et al., 2012, 2013, 2014; Ferreira, et al., 2019b; Ferreira, et al., 2019a; Ferreira et al., 2020).

The stochastic nature of shear stress has led to a paradigm shift toward a more probabilistic perspective over the years, exploring the concept of PDFs to describe the innate variability and uncertainty in shear stress distribution (Savage and Jeffrey, 1951; Antonia, 1977; Dreeben and Pope, 1997; Keshavarzy and Ball, 1997; Miyagi et al., 2000; Cheng et al., 2003; Colella and Keith, 2003; Cheng, Tang and Zhu, 2004; Reeks, 2005; Cheng, 2006; Richefeu, et al., 2006; Sarmiento and Falcon, 2006; Dentoni et al., 2022; Zou et al., 2022). This probabilistic modeling also recognizes the complexity and variability inherent in natural processes related to shear stress, such as particle emission, where parameters such as material heterogeneity, the characteristics and distribution of roughness elements, and environmental conditions can significantly impact the shear stress. The aim of this study is to investigate the turbulence structures near a rough wall in which the rough elements would represent non-erodible particles in a bed or in a stockpile of granular material exposed to the atmospheric flow to evaluate how these turbulence structures could influence particles emission during a wind erosion event and identify patterns on the friction velocity distribution on the ground that could assist an emission model.

This thesis aims to improve the physical understanding of particle emissions and transport resulting from wind erosion of granular materials in beds and stockpiles, considering local and non-local aspects of turbulent fluid flow dynamics. The specific objectives include analyzing the influence of different configurations of successive stockpiles on the re-emission potential of particles from their surroundings, assessing the impact of non-erodible particles on the development of fluid flow structures responsible for the entrainment of erodible particles, and evaluating the similarity requirements of wind flow, particle entrainment, and particle transport in wind tunnel experiments to achieve a representative simulation of real-scale scenarios.

This understanding is important for developing improved simulation techniques and predictive models for mitigating wind erosion impacts in natural and industrial environments. Additionally, this thesis discusses theoretical issues concerning representing real-scale particle dynamics in wind tunnels, supporting future experimental studies in this field.

This thesis is organized into seven chapters. Chapter 2 presents the objectives of the thesis. Chapter 3 presents the literature review. Chapter 4 describes the research on wind erosion pursued by the Air Quality Research Group at the Federal University of Espírito Santo, contextualizing this thesis with their published articles. Chapter 5 outlines the experimental works and numerical simulations performed by other authors and presents the methodology for conducting LES in the present thesis to evaluate local turbulence structures linked to the presence of non-erodible particles. Chapter 6 presents the obtained results organized into three sections, being the last two section organized into a paper and a technical note, respectively. Finally, Chapter 7 concludes the work, summarizing the research findings, highlighting their contributions to environmental science and granular material management, and providing recommendations for future work.

2. OBJECTIVES

2.1. General objective

Improving the physical understanding of particles emission and transport resulting from wind erosion of granular materials in beds and stockpiles considering local and non-local aspects of turbulent fluid flow dynamics.

2.2. Specific objectives

- Analyzing the influence of different configurations of successive stockpiles on re-emission potential of particle from its surroundings.
- Assessing the influence of non-erodible particles on the development of fluid flow structures responsible for the entrainment of erodible particles.
- Evaluating the similarity requirements of wind flow, particle entrainment and particle transport in wind tunnel experiments aiming a representative simulation of real scale scenarios.

3. LITERATURE REVIEW

In this section, a review of the literature on wind erosion is presented, encompassing the physics that have shaped the current understanding of this phenomenon. The review will explore many aspects of wind erosion, including the fundamental mechanics of particle movement induced by aerodynamic forces, the influence of turbulent flow, and the impact of surface roughness and non-erodible particles on erosion dynamics.

3.1. Forces acting on particle's emission

Particles emission is mainly influenced by aerodynamic forces, which tend to remove them from the surface (such as drag force F_d and lift force F_l) and by forces that resist to their movement (such as gravity force F_g and cohesive force between particles F_c), as shown in **Figure 1** (Caliman, 2017):

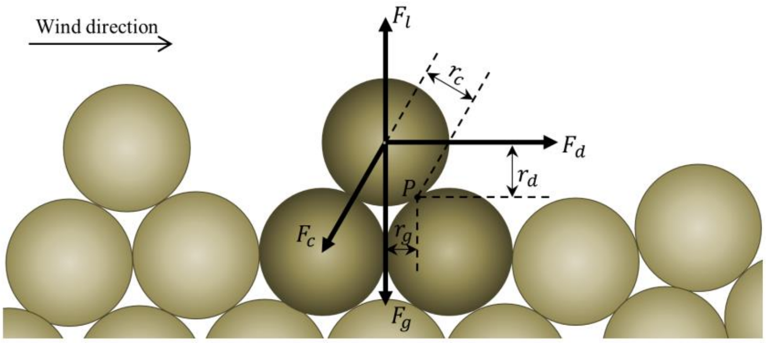

Figure 1. Forces acting on the particle subjected to a velocity gradient: lift, drag, cohesion and gravity (Caliman, 2017).

3.1.1. Motivating forces of particles movements: drag and lift forces

The drag and the lift forces or, the aerodynamic forces, are the ones responsible for the particle's movement in the air. The drag force arises from pressure differences between the frontal and the wake region of the particle and from *momentum* transfer from the surrounding fluid to the particle through molecular motion or the so-called viscous effect. It can be defined either as the force in the opposite direction of the relative velocity one exerted by the fluid on the particle This force can be approximated by (Shao, 2008):

$$F_d = K_d {D_p}^2 \rho {u^*}^2 \qquad (1)$$

where K_d is a dimensionless empirical parameter function of the particle Reynolds number ($Re_p^* = u^* D_p / \nu$) suggested to have a magnitude around 4 (Shao and Lu, 2000) and D_p is the particle diameter [m].

On the other hand, an aerodynamic lift arises from a shear in the flow, which results in a normal pressure gradient to the shear in the direction of decreasing velocity. The aerodynamic lift can be approximately by (Shao, 2008):

$$F_l = K_l {D_p}^2 \rho {u^*}^2 \qquad (2)$$

where K_l is a dimensionless empirical parameter suggested to have a magnitude around 2 by Shao and Lu (2000).

3.1.2. Restrictive forces of particles movements: gravity and cohesive forces

3.1.2.1. Dust and powder

There are two terms that are very similar in the scientific literature: *dust* and *powder*. These two words can be easily applied to the same material due the particle size associated with both, usually below 100 µm (Baitimerov et al., 2018; Duran, 2000; Mullis et al., 2013; Y. Shao, 2008). The difference, however, remains at the origin of the material. Powders are usually manufactured for some purpose, as for medicines for instance. Dusts get this name when the materials have a natural origin on the Earth's surface or when they are related to non-positive factors (not being a rule), such as dust emission from roads, buildings, industrial sites and industrial processes, that can cause some risk to the environment or to the human health. As these work concerns about air pollution, the term *dust* will be used going forward.

3.1.2.2. Constraints mechanisms of dust movement related to particle's properties

When dusts flow, the micro particles within them move relative to each other. The mechanisms that control these movements are: (i) friction, (ii) mechanical interlocking, (iii) liquid bridging, (iv) cohesion and (v) gravity (Clayton, 2019).

Smooth particles tend to move easily relative to each other because of the lower friction acting at the contact points. The level of friction between them will be influenced by the chemical nature of the material and also by surface properties as can be seen in **Figure 2a**, that shows the friction mechanism between particles.

When the particles have a shape that results in substantial mechanical interlocking (**Figure 2b**), they will strongly resist to the movement, even if their surface friction is low. However, if the particles have a more rounded morphology, they are more likely to past one another, even if they still under other mechanisms influences.

Liquid bridging, showed in **Figure 2c**, is known for promoting a negative impact on dust mobility. This is not always true, but liquid bridging can, for sure, constrain the flow. Liquids between dust particles, usually adsorbed moisture, tend to coat their surface, forming bridges that do not allow the free movement of one particle. However, water can help dissipate electrostatic charge improving flow properties. The challenge is to assure that the grains have sufficient moisture to minimize the electrostatics effects, but not enough to create capillary bonds reducing the probability of movement.

Figure 2d shows the inter-particulate forces of attraction (often called cohesive forces for similar particles). This kind of interaction is derived from a combination of van der Waals forces and electrostatic charge on the surface of the particles that acts holding them close to their neighbors. As result, agglomerates can be formed and, the particles can be not able to move.

In unconsolidated dust, the ability of a particle to begin to flow is largely dependent on the gravitational force acting on it, i.e., its weight (**Figure 2e**). Generally, the higher their influence, i.e., the particles size or particle density, the lower is the ability of particle to move.

In the present work, among all these mechanisms that inhibit the particles movement, only the effects of gravity and cohesion will be analyzed. The particles will be considered perfectly round with a completely smooth surface. As first approach, moisture will not be included.

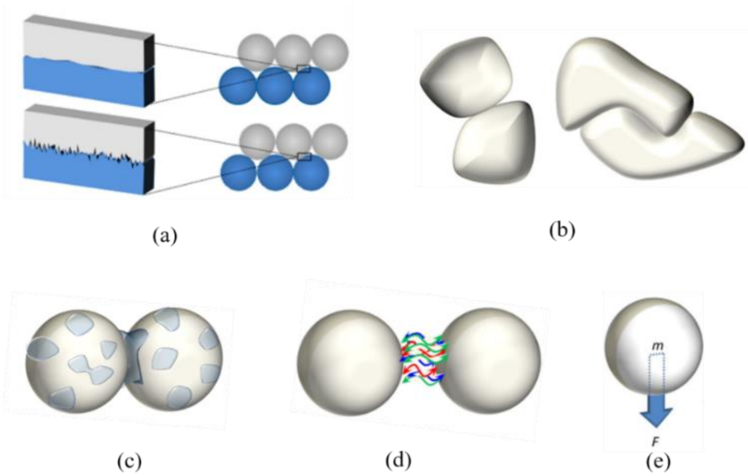

Figure 2. Mechanisms behind dust movement. (a) friction, (b) mechanical interlocking, (c) liquid bridging, (d) inter-particulate forces of cohesion and (e) gravity (Clayton, 2029).

3.1.2.3. Gravitational force

In the Earth's atmosphere the external force is the gravitational force g [m/s²], and for a particle of diameter d [m], with density ρ_p [kg/m³]:

$$F_g = \frac{\pi}{6} {D_p}^3 (\rho_p - \rho) g \tag{3}$$

where ρ_f is the density of the fluid [kg/m³].

3.1.2.4. Inter-particle force of cohesion

At this point another distinction must be done. The term *cohesion* quantifies the strength of particle-particle interactions while the term *adhesion* is a measure of the propensity of particles to stick to a different surface or material (Clayton, 2019). So, the main subject of this section is the cohesion.

The cohesive force consists of (i) van der Waals, (iii) electrostatic, (iii) capillary (when moisture is considered which is not the case of the present project) and (iv) chemical binding forces (formed when salts, mainly in soils, interact with clay particles and form chemical bonds, subject also not discussed in the present work). The values of inter-particulate forces can vary widely, depending on the chemical composition of the particles, their shape and surface texture, bulk water content, and processing history (Clayton, 2019). Cohesive forces can be considered the most challenging of all particle-particle interactions and are difficult to quantify and model precisely (Clayton, 2019; Shao, 2008). However, their influence dominates, particularly when the dust is required to flow. It is very important, therefore, that these forces are well understood. Some works tried to quantify the components of the cohesive particle interactions in a deterministic way. It will be presented expressions only for the estimation of the van der Waals and electrostatic forces, once the other forces responsible for the cohesive effect appear in scenarios that will not be the aim, a priori, of the present project.

The van der Waals forces are responsible for the attraction between uncharged particles of very small diameter. For a small spherical particle of diameter D_p with a separation, d, from a same-sized particle, one approximation for a van der Waals force between the two particles in *vacuum* $d/D_p \ll 1$is:

$$F_{iv} = \frac{h_w}{32\pi d^2} D_p \tag{4}$$

where h_w is a coefficient varying between $10 - 18\ J$ and $10 - 21\ J$, depending on the material. The smallest value of δ is conventionally considered to be 0.4 nm, because below this distance, repulsion between the particles can be noticed (Theodoor and Overbeek, 1985). For $d/D_p >$ 0.2, the van der Waals attraction becomes negligible, being of the order of the Brownian forces.

The electrostatic force applicable to dust emission is the non-conductor force. For smooth and ideally spherical particles, they can be written as:

$$F_{ie} = \frac{\pi B_p V^2 D_p}{2d} \tag{5}$$

where V is the contact potential difference, which generally ranges from 0 to about 0.5 volts, d is the separation between the two adhering particles and B_p is the permittivity of free space.

3.2. Take-off criterion

3.2.1. Deterministic approach of the threshold friction velocity of particles

The aerodynamic forces acting on the particles are associated with the near-surface wind drag. Thus, it is a function of the friction velocity u^*, characteristic of the boundary layer flow representing the conceptual value of the surface shear:

$$u^* = \sqrt{\tau/\rho} \tag{6}$$

where τ is the shear strees $[Pa]$ and ρ is the fluid density $[kg/m^3]$.

It is also important to define, for the study of particle movement, the threshold friction velocity u_t^*, which is the minimum friction velocity required for particle movement to be initiated. When the friction velocity at the surface does not reach the threshold friction velocity of the material ($u^* < u_t^*$), the particles tend to remain on the surface. When the opposite occurs ($u^* > u_t^*$), the movement of the particles begins. The threshold friction velocity is essentially a property of the agglomerated granular material and its agglomeration form. It describes the surface's ability to withstand wind erosion and is affected by several factors such as particle and fluid specific mass, particle diameter, gravity effects, humidity and cohesive effects.

Nevertheless, under ideal conditions, such as the absence of moisture and the cohesive effects between particles, u_t^* can be expressed as a function of particle diameter. Bagnold (1941) was one of the firsts to develop an expression for u_t^* based on the balance of forces acting on particles (Kok et al., 2012). However, Bagnold's proposal has limitations such as considering the balance only between drag and gravity forces and not being defined for small diameters. Thus, subsequent experimental and theoretical studies emerged resulting in other expressions for u_t^*.

Figure 3 shows the curves of the main studies related to the subject up to the most recent by Shao and Lu (2000). Shao and Lu (2000), unlike Bagnold (1941), proposed an expression that also considers cohesive forces, important for small diameter particles. Shao and Lu (2000) particle emission criterion is:

$$u_t^* = 0{,}11 \sqrt{\frac{\rho_p - \rho}{\rho} gD + \frac{\gamma}{\rho D}} \tag{7}$$

where ρ_p is the particle density $[kg/m^3]$, ρ is the fluid density $[kg/m^3]$, D is the particle diameter $[m]$, g is the gravity acceleration $[m/s^2]$ and γ is the surface energy that characterizes the cohesion $[N/m$ or $kg/s^2]$. Shao and Lu (2000) recommend values of γ in the range 1,65×10^{-4}e 5,00×10^{-4}kg/s^2. Kok and Renno (2009) used the value of 2,86×10^{-4} kg/s^2 that obtained experimentally. Shao and Klose (2016) used the values 0,75×10^{-4} e 1,5×10^{-4} kg/s^2 as can be seen in **Figure 3**. It is also important to highlight two points in **Figure 3**. First the Shao and Lu (2000) curve is plotted with different values of γ, 0.75×10^{-4} and 1.5×10^{-4} kg/s^2. Shao and Klose (2016) do not explain why they were using different values, but a considerable shift is observed when γ increases, meaning that the criterion that determines the particle erodibility is very sensitive to this variable. The problem that emerges from this statement is that, for right prediction of the particle take-off, the γ value for the material to be considered must be known. However, the inter-particle forces between small particle are not well determined, bringing a source of uncertainty to the study of dust emission.

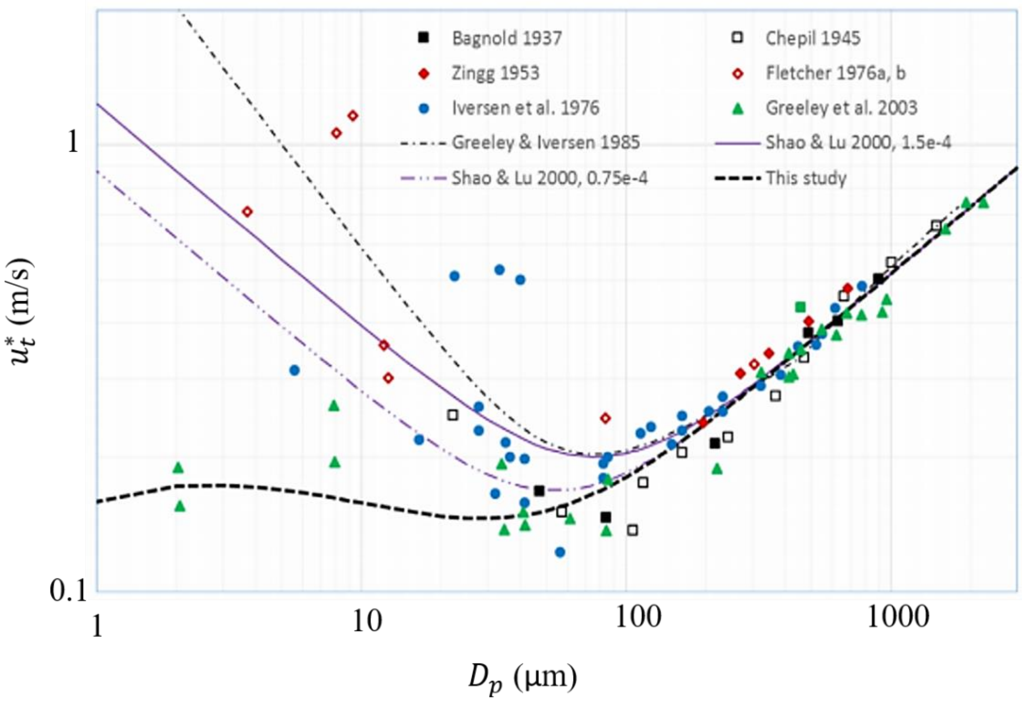

Figure 3. Threshold friction velocity as function of particle size (Shao and Klose, 2016). The lines represent analytic expressions and the dispersed points, experimental data.

3.2.2. Stochastic nature of threshold friction velocity of dust

As already discussed, the cohesive forces are influenced by wide number of very complex factors. So, it seems rational to consider inter-particle cohesion and the threshold friction velocity for dust particles, as a stochastic variable which satisfies some probabilistic distribution. Laboratory experiments (Y. Shao, 2008) indicate that a wide range of dispersion in the measurements of cohesive forces may occur for nearly identical macroscopic conditions. This dispersion increases with decreasing of particle size, and the spread can be as large as several orders of magnitude.

In other words, while it is meaningful to define a threshold friction velocity through the deterministic approach for sand-sized particles as described in the previously section, it is not meaningful to do the same for dust particles. It is possible to see in **Figure 3** that the experimental data for small particles are very dispersed not being possible to observe the same coherent results between the authors as those observed for the large ones.

It is necessary obtain a distribution of the cohesive forces for dust particles, or at least, its statistical parameters, and then work with it to estimate the threshold friction velocity properly. Zimon (1982) suggested that the cohesive force can be described using a log-normal distribution:

$$p(f_i) = \frac{1}{F_i\sqrt{2\pi}\sigma_{F_i}} exp\left\{-\frac{[\ln F_i - \ln \bar{F}_i]^2}{2\sigma_{F_i}^2}\right\} \tag{8}$$

$\bar{F}_i(d)$ [mdyn] and $\sigma_{F_i}(d)$ [μm] are given by:

$$\bar{F}_i(d) = \exp{(4.3569 - 0.2138d + 0.0018d^2)} \tag{9}$$

$$\sigma_{F_i}(d) = 4.1095 - 0.04761d \tag{10}$$

where $\bar{F}_i$ is the mean value of the cohesive force, σ_{F_i} is the geometric standard deviation and d is the particle diameter for particles smaller than 100 μm. **Figure 4** shows $p(f_i)$ for different-sized spherical glass particles of different diameters resting on a steel surface, using the data of Zimon (1982). It is important to note how $p(f_i)$ varies with particle size. In **Figure 4** the geometric standard deviation for the log-normal distribution, σ_{F_i}, is inversely proportional to the particle size. For particles with a diameter around 100 μm, the distribution function $p(f_i)$ shows a narrow peak, while for smaller particles $p(f_i)$ spreads much more widely.

So far, no direct measurements of the threshold friction velocity for fine particles was found. As it is to be directly related by the cohesive force, as a first approach, it can be hypothesized that the distribution of the threshold friction velocity should be close to a log-normal distribution.

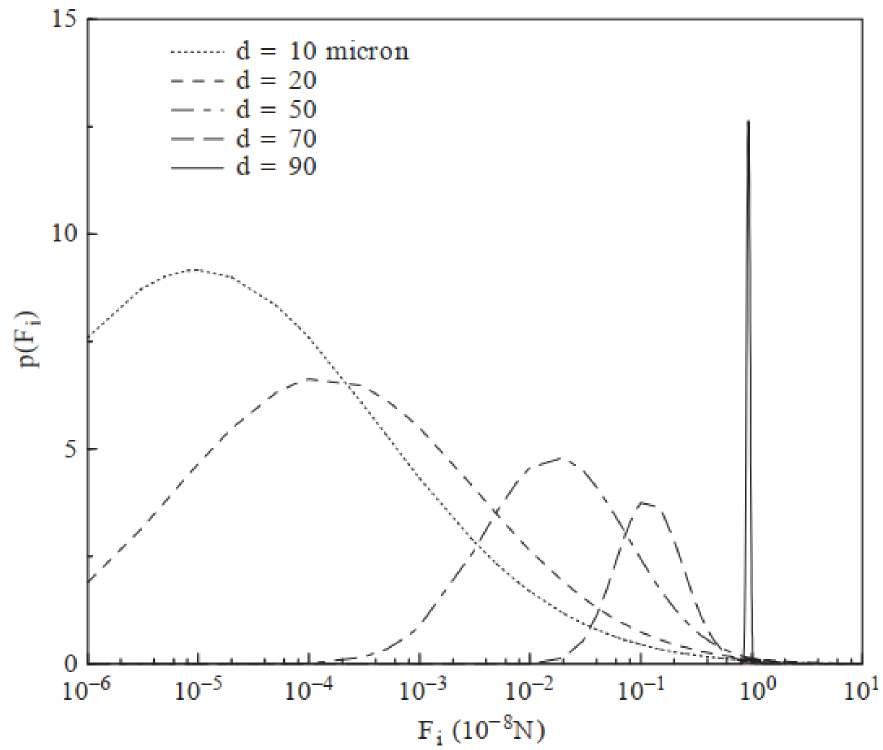

Figure 4. Probability density functions of cohesive force for spherical glass particles on steel for five different particle-size groups, as determined by Zimon (1982). The probability density functions can be approximated as log-normal distributions which have an increasing geometric standard deviation for smaller particles.

3.3. Other important effects on dust emission

3.3.1. Non-erodible particles effect or pavement effect

The analysis of dust emission in the presence of non-erodible particles exposed to a turbulent wind flow is usually carried out by means of the wall shear stress distribution. Non-erodible elements modify the flow around them, reducing the friction velocity in its surroundings. Therefore, their do not allow the particles threshold friction velocity to be reached. This effect is well known in the literature (Brown et al., 2008; Descamps et al., 2005a; Gillette and Stockton, 1989a; Gillies et al., 2007, 2006; Iversen et al., 1991a; King et al., 2005; Marshall, 1971a; Raupach et al., 1993a) and is called pavement effect. **Figure 5** shows a particle bed before and after the pavement. The black particles are non-erodible, and the white ones are erodible. **Figure 5a** shows the beginning of erosion and **Figure 5b** shows the end of erosion where particles are no longer emitted. It is possible to observe that even though white particles were available, they were not emitted due to the protective effect of the non-erodible black particles.

(a) (b)

Figure 5. (a) Bed before pavement and (b) bed after pavement (Caliman, 2017).

Studies on the influence of non-erodible elements in wind flow led to mathematical formulations that described the evolution of friction velocity as a function of bed properties.

Raupach et al. (1993) developed an expression for the shear stress partition due to the presence of non-erodible elements as a function of elements density λ:

$$R^{"} = \frac{u_s^*}{u_r^*} = \left[\frac{\tau_s^{"}}{\tau}\right]^{1/2} = \left[\frac{1}{(1 - m\sigma\lambda)(1 + m\beta\lambda)}\right]^{1/2} \quad (11)$$

where u_s^* is the average friction velocity [m/s] on a surface without the influence of roughness, u_r^* is the average friction velocity on an erodible surface under the influence of roughness [m/s], $\tau_s^{"}$ is the maximum shear stress on a surface without the presence of non-erodible elements [Pa], τ is the total shear stress on a surface under the influence of roughness [Pa], m (< 1) is a parameter that accounts for differences between the average shear stress on the bed surface and the maximum shear stress on the surface at any point, σ is the ratio between basal area and frontal area of the roughness elements and β is the ratio between the drag coefficient for isolated roughness elements and the drag coefficient for the surface.

Turpin et al. (2010) performed simulations of beds composed by non-erodible elements to also investigate the friction velocity on the erodible surface. The work evaluated the parameter R_{fric}, defined by:

$$R_{fric} = \frac{u_r^*}{u_s^*} = \frac{1}{R^{"}} \quad (12)$$

where u_r^* is the average friction velocity on an erodible surface under the influence of roughness [m/s] and u_s^* is the average friction velocity [m/s] on a surface without the influence of roughness. This parameter reflects the evolution of friction velocity with the increase in the number and height of rough elements as the aeolian erosion occurs. Turpin et al. (2010) found considerable differences in friction velocity for configurations with the same density λ and different b/h ratios, indicating that it is strongly influenced by the properties of non-erodible particles on the bed surface. Then, they proposed a mathematical formulation different from the formulation of Raupach et al. (1993) to remove the explicit dependence on λ and include other properties:

$$1 - R_{fric} = A(CR)^{M}\left(S_{frontal}/S_{floor}\right)^{N} \tag{13}$$

where A, M and N are constants from numerical simulations, CR is the cover rate of non-erodible particles, $S_{frontal}$ is the frontal area of the elements [m²] and S_{floor} is the basal area of the elements [m²]. The ratio $S_{frontal}/S_{floor}$ for cylindrical elements is given by:

$$\frac{S_{frontal}}{S_{floor}} = \frac{4}{\pi}\frac{\bar{h}_r}{\bar{D}_{NE}} \tag{14}$$

where $\bar{D}_{NE}$ and $\bar{h}_r$ are, respectively, the average diameter [m] and the average height [m] of the non-erodible elements.

The simulations carried out by Turpin et al. (2010) were validated with results from previous studies comparing the ratio of measured and modeled friction velocities (Crawley and Nickling, 2003; Gillette and Stockton, 1989a; Gillies et al., 2007; Lyles and Allison, 1975; Marshall, 1971a; McKenna Neuman and Nickling, 1995; Musick and Gillette, 1990).

In the simulations carried out by Turpin et al. (2010), roughness or non-erodible particles were represented as cylinders. The authors justified that in **Equation (13)** when using the relationship between the areas, $S_{frontal}/S_{floor}$, the drag coefficient depended only on this ratio and no longer on the shape of the rough element. Furthermore, the use of this dimensionless area parameter would better incorporate the influence of element shape on friction velocity than the previously suggested dimensionless length parameter h/b (**Figure 6**).

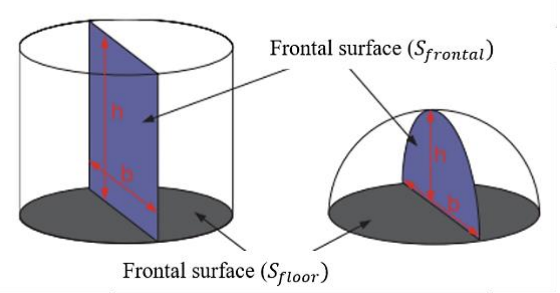

Figure 6. Schematic representing parameters h, b, $S_{frontal}$ and S_{floor} (Turpin et al., 2010).

Figure 7a shows the typical behavior of surfaces composed by erodible and non-erodible elements. The initial increase of the emitted mass is due to the movement of the particles that had their threshold friction velocity reached by the wind flow shear stress, the erodible ones. Over time, the emitted mass flux decays and the emitted mass remains constant. This phenomenon, where emission is no longer observed is called pavement and happens even when erodible particles are available. This occurs due the presence of the non-erodible particles. The effects of non-erodible elements are widely studied (Descamps et al., 2005b; Ferreira et al., 2019b; Furieri et al., 2013c; Gillette and Stockton, 1989b; Gillies et al., 2015; Iversen et al., 1991b; Li and Shao, 2003; Marshall, 1971b; Miri et al., 2017b; Raupach et al., 1993b; Tan et al., 2013; Turpin et al., 2010b) and are understood as a creation of low shear stress zones downstream particles of larger diameter (**Figure 7b**) that do not allow the threshold friction velocity of the surrounding particles to be reached. Therefore, this effect must be considered in emission models to provide more realistic results.

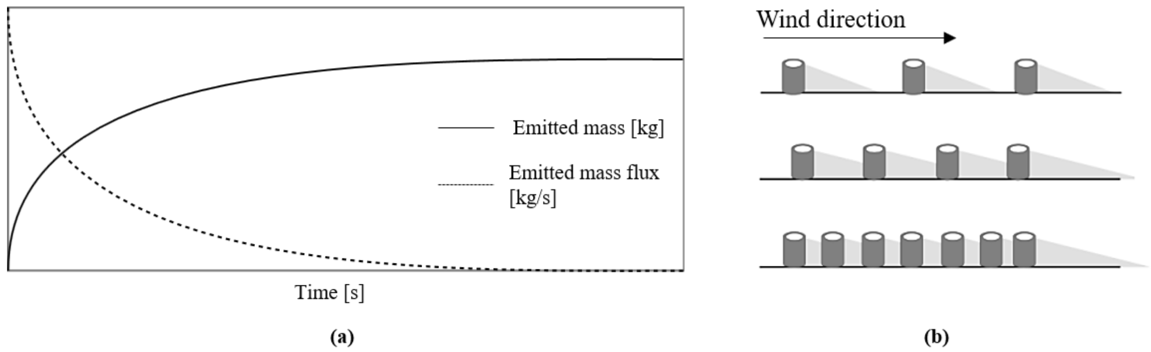

Figure 7. Schema of (a) temporal evolution of emitted mass and emitted mass flow on a surface composed of erodible and non-erodible particles until the pavement and (b) bed showing the low shear stress downstream the non-erodible elements. Adapted from Nickling and McNeuman (2009).

3.3.2. Turbulent structures effect

In a turbulent boundary layer different regions can be found associated with the velocity distribution as can be seen in **Figure 8** (Davidson, 2015). The dimensionless velocity, u^{+}, is define by $u^{+} = u/u^{*}$, and the dimensionless wall coordinate, y^{+}, by $y^{+} = yu^{*}/\nu$, with the y-axis normal to the wall. Particles emission generally occurs in the inner region of the turbulent boundary layer which are divided into the viscous sublayer, buffer layer and the logarithmic layer (You and Wan, 2017). According to Ziskind et al. (1995), fine particles, subject of the present work, are generally immersed in the viscous sublayers. Exactly on this sublayer, an interesting phenomenon has its origin, and it has been claimed as the mechanism responsible for the most part of the turbulence production. There is a consensus among the researchers that the turbulence is mainly produced close to the walls due to a repetitive cycle of intermittent events called turbulent bursts (Davidson, 2015; You and Wan, 2017).

The viscous sublayer is continually disturbed by turbulent inrushes and bursts going deep in the near wall region where becomes very unstable. You and Wan (2017), as shown in **Figure 9**, describes the development of explosions with the following words: “a decelerated region is formed due to the wall skin friction and is then subject to the effect of an upstream large-scale disturbance of a high axial velocity. At the transition from the overflowing disturbance to the decelerated region, a strong shear layer is developed and induces an abrupt ejection (burst) of fluid from the decelerated region towards the turbulent core. Chaotic motions are caused by the violent interactions at the shear layer between the ejecting fluids and the faster overflowing fluids. Some chaotic motions induce the wall Ward flow (inrush) that could reach all the way up to the wall”.

Therefore, when fluid is ejected from the wall there is a high probability of particles been carried out from the viscous sublayer to the outer region.

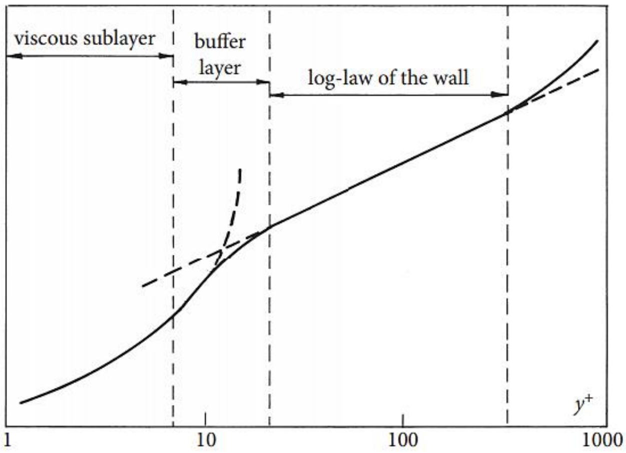

Figure 8. Boundary layer velocity profile of u^+ *versus* y^+ (Davidson, 2025).

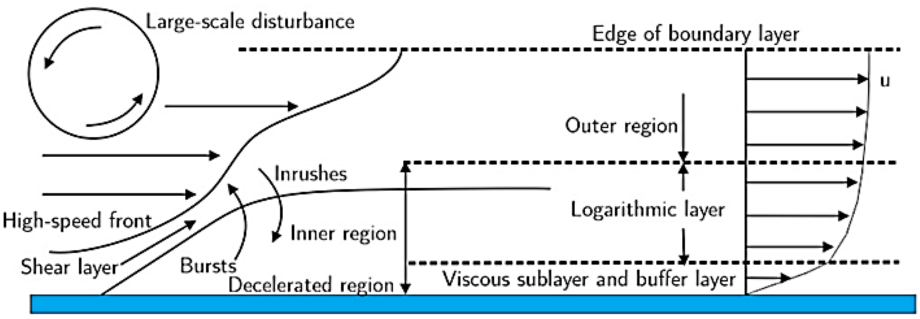

Figure 9. A schematic of the turbulent boundary layer and the development of bursts and inrushes (You and Wan, 2017).

3.4. Modes of particle motion and mechanisms for dust emission

According to Bagnold (1941), depending on particle diameter, there are three modes of particles motion: suspension, saltation and creep. **Figure 10** (Shao, 2008) shows the modes of particle motion for soil particles during an erosion event. Long and short terms refer to the time that small particles, up to 70 μm, can remain dispersed on the atmosphere, days and hours respectively. Saltation is the movement that particles perform when they leave and, due its weight, return to the surface. Modified saltation occurs when the particle has its diameter between 70 – 100 μm. Particles with diameter larger than 500 μm perform the creep motion, rolling over the surface.

Shao (2008) proposes that are three mechanisms in which particles of small diameters, interest of the present project, are suspended: Aerodynamic lift, saltation bombardment, and disaggregation. In aerodynamic lift, particles are lifted from the bed surface directly by aerodynamic forces (Loosmore and Hunt, 2000). However, this mechanism occurs in a small probability compared to the two others. This happens because, for very small particles, the importance of gravity and aerodynamic forces decreases as the inter-particle cohesion becomes important. Saltation bombardment or sandblasting (Alfaro et al., 1997) causes small particles emission by the impact of the large ones on the surface overcoming the binding forces that act to maintain the grains on the bed. According to Shao et al. (1993), the saltation bombardment is one order more effective than the aerodynamic lift. Disaggregation or auto-abrasion occurs when a set of dust particles attached to sand grains (usually under natural conditions) disintegrate during a strong wind erosion event. Shao (2008) reinforces that the importance of this mechanism is probably like that of saltation bombardment. Schemes of mechanisms for dust emission are shown in **Figure 11**.

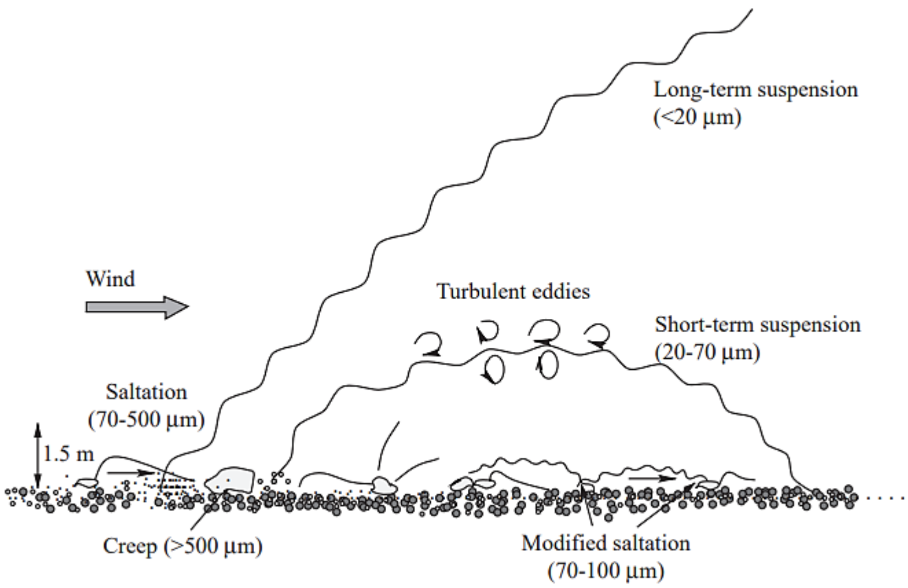

Figure 10. An illustration of creep, saltation and suspension of soil particles during an erosion event (Shao, 2008; Pye, 1987).

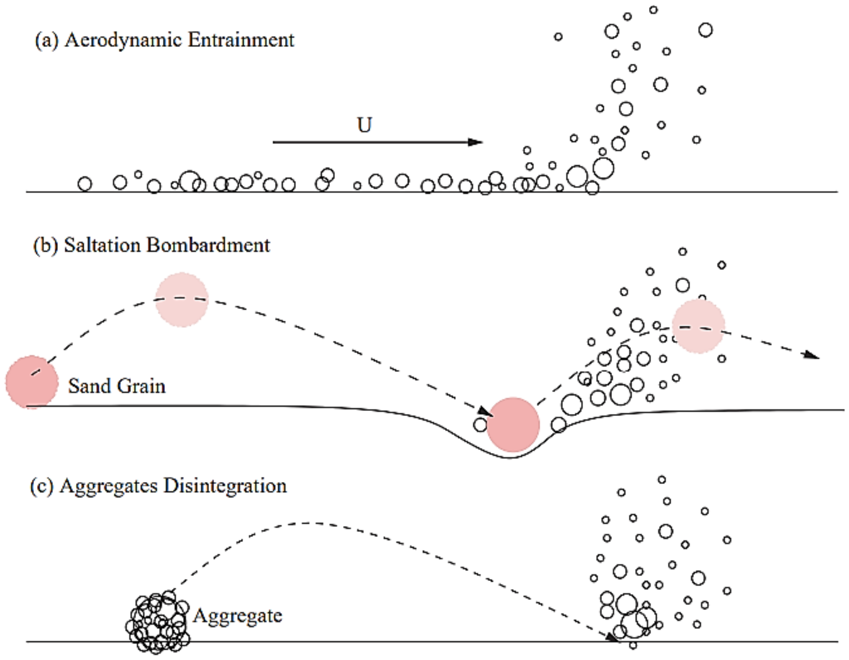

Figure 11. Mechanisms for dust emission (Shao, 2000).

3.5. Emission models for particles bed

Descamps et al. (2005) developed a model to quantify the temporal evolution of the mass flow in a bed of particles with a wide particle sizes distribution exposed to turbulent flow. The authors considered the temporal decrease of aerodynamic forces acting on the particles and, consequently, the temporal evolution of the distribution of these particles on the bed surface. It was the first job to model the pavement phenomenon. However, Descamps et al. (2005) assumed that erosion ceases when the bed is completely covered by non-erodible particles, disagreeing then, with experimental results. In addition, the authors included in the model the influence of turbulent bursts on the particle's emission. They used results from numerical simulations on smooth surfaces to estimate the frequency of occurrence of the vortexes, which indeed do not reflect the reality of particles bed surfaces.

Kok et al. (2014) developed a model for the particle flow emitted by erodible soils dependent only on variables whose values are normally available, such as wind speed and soil properties. The model considers that saltation can influence the emission of other particles by the impact caused when the saltating particles return to the bed. In addition, it includes the cohesion between the smaller diameter particles, being valid then, for a wide particle size distribution.

However, this model has the limitation of not estimating the variation of the emitted mass flow over time, considering, therefore, that the amount of erodible particles is unlimited.

Klose et al. (2014) proposed a new approach for a model that considers turbulent convection in particles emission. Based on numerical simulations, a new method for describing the amount of instantaneous movement flow was developed, as well as corrections for considering cohesion because of humidity and for considering the presence of non-erodible elements. However, the correction for including the effects of non-erodible elements still has basement limitations, because the model has not been compared with experimental results requiring further investigations about its validity.

Zou et al. (2015) proposed a conceptual model for material emitted during erosion considering a wide range of factors involved in the phenomenon. The particle size distribution, salt and organic matter content, liquid water content, frozen water content, snow cover and plant roots are considered as bed anti-erodibility factors; vegetation and gravel cover are considered factors of roughness interference; and all these factors are expressed as shear forces. By comparing a standard graph of the amount of emitted mass as a function of shear stress and the corresponding graph resulting from experimental tests, the model allows that data at reduced scales to be extrapolated to field scales. However, the estimate is still theoretical, having no basement or experimental validation.

Hoonhout and Vries (2016) presented a model that considers the spatial and temporal variation of the availability of sediments at the height and on the bed surface. Simulations of the spatial and temporal properties of the surface are performed to estimate variations that interfere in the emission process, such as particle size distribution and the protective effect created by rough non-erodible elements that emerge from the surface with wind erosion. The model's performance was assessed through hypothetical case studies and experimental results obtained from the literature, showing that it still needs to be further investigated.

Ferreira et al. (2019a) proposes a model for beds composed by a simple equation that calculates the emitted mass through the emitted volume:

$$E_f = (1 - \alpha_{NE})\rho_{bed} H_f S_{bed} \tag{15}$$

where α_{NE} is the mass fraction of non-erodible particles, $\rho_{bed} = \varphi \rho_P$ $[kg/m^3]$, φ is the volume fraction of the mixture, ρ_P is particles density $[kg/m^3]$, H_f is the final eroded bed height e S_{bed} is the bed superficial area $[m^2]$.

Ferreira et al. (2019) estimated H_f considering the pavement effect caused by the presence of non-erodible particles based on the studies by Turpin et al. (2010) as shown in **Equation (16)**:

$$1 - R_{fric} = A\left(aH_f + CR_i\right)^M \left(\frac{4H_f}{\pi \overline{D}_{NE}}\right)^N \quad (16)$$

where A, M and N are constants obtained from numerical simulations, CR_i is the initial cover rate of non-erodible particles, $\overline{D}_{NE}$ is the mean height of non-erodible elements[m], R_{fric} is the variable that represents the evolution of the bed friction velocity through the ratio u_r^*/u_s^*, where u_r^* is the average friction velocity on an erodible surface under the influence of roughness [m/s] and u_s^* is the average friction velocity [m/s] on a surface without the influence of roughness.

3.6. Emission models for stockpiles

The most widely used emission model for stockpiles on industrial sites was proposed by the United States Environmental Protection Agency (USEPA, 2006b). The USEPA model quantify the total emission (E), in g, from eroded stockpiles surfaces by:

$$E = \mathrm{K} \sum_{i=1}^{N} \sum_{j=1}^{M} P_{ij} A_{ij} \quad (17)$$

The particle size multiplier K for the equation varies with the aerodynamic size of the particle as shown in **Table 1**.

Table 1. Particle size multipliers based on diameter (USEPA, 2006).

Particle size multipliers			
$30\ \mu m$	$< 15\ \mu m$	$< 10\ \mu m$	$< 2{,}5$ µm
1,0	0,6	0,5	0,075

The erosion potential [g/m²] for a dry exposed surface is:

$$\begin{cases} P = 58\,(u^* - u_t^*)^2 + 25(u^* - u_t^*) \\ P = 0 \text{ for } u^* \leq u_t^* \end{cases} \quad (18)$$

where u^* is the friction velocity [m/s], u_t^* is the threshold friction velocity [m/s] (minimum friction velocity at which particles starts its movement). When the friction velocity at the surface does not reach the threshold friction velocity of the material ($u^* < u_t^*$), the particles tend to remain on the surface and P goes to zero. When the opposite occurs ($u^* > u_t^*$), the movement of the particles begins. The threshold friction velocity is essentially a property of the agglomerated granular material and its agglomeration form. It describes the surface's ability to withstand wind erosion and is affected by several factors such as particle and fluid specific mass, particle diameter, gravity effects, humidity, and cohesive effects.

The US EPA emission model lists, according to **Table 2**, threshold friction velocity for different materials obtained by portable wind tunnel. However, it is also possible to obtain the threshold friction velocity experimentally in laboratory wind tunnel and theoretically (Bagnold, 1941; Foucaut and Stanislas, 1996; Iversen and White, 1982; Shao and Lu, 2000).

Table 2. Threshold friction velocity u_t^* of some materials from USEPA.

Material	Threshold friction velocity [m/s]
Overburden	1.02
Scoria (roadbed material)	1.33
Ground coal (surrounding coal pile)	0.55
Uncrusted coal pile	1.12
Scraper tracks on coal pile	0.62
Fine coal dust on concrete pad	0.54

In the US EPA model, regions over the stockpile surface with the same values of normalized velocity distribution (u_s/u_r) are grouped into subareas. The variable u_s and u_r are, respectively, the surface velocity measured at 25 cm from the stockpile surface and the reference wind velocity measured, for example, at 10 m height. The normalized velocity distribution (u_s/u_r) for two stockpiles shapes (cone and oval shape) and three incident angles (20°, 40°, and 90°) was determined US EPA. **Figure 12** shows the subareas with same u_s/u_r over the stockpiles.

From this strategy, each subarea of the stockpile is considered as individual diffuse source, M is the number of subareas, P_{ij} is the erosion potential of each subarea [g/m²], and A_{ij} is the area of each subarea [m²] in **Equation (17)**. The subscript i refers to the i-th disturbances N (number of material addition or removal operations exposing new erodible areas) and the subscript j refers to the j-th subarea of the stockpile surface.

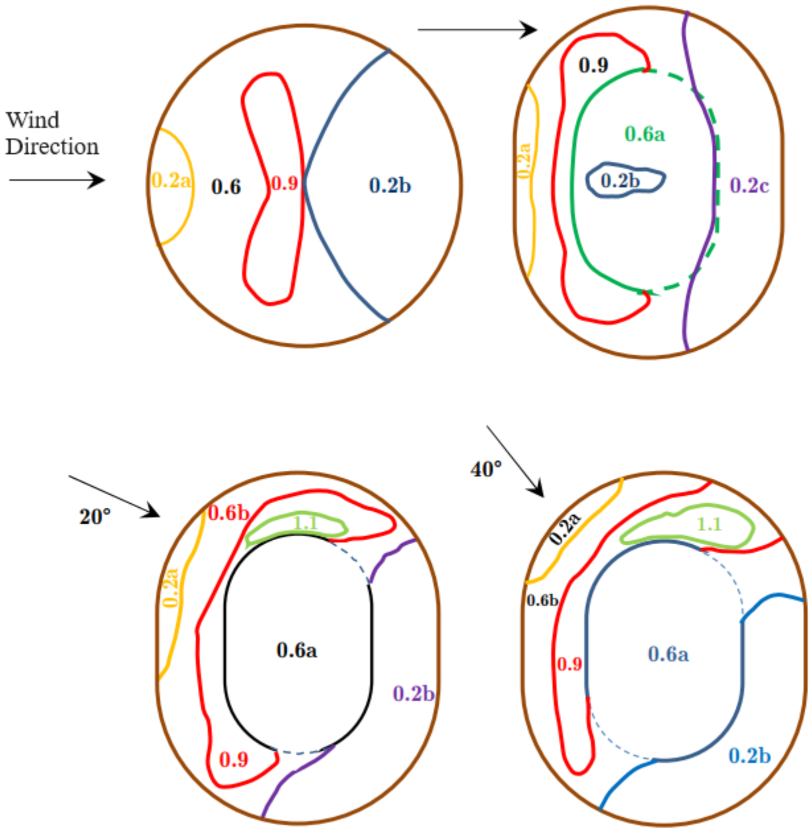

Figure 12. Normalized velocity distribution u_s/u_r of stockpiles from left to right: cone shape, oval shape with flat top (both with 90° wind direction), oval shape with flat top and wind direction 20°, and oval shape with flat top and wind direction 40°. Adapted from USEPA (2006b) (Nascimento, 2014).

Finally, the normalized velocity distribution (u_s/u_r) is used to calculate the friction velocity u^*over the stockpile surface. The roughness of each stockpile surface is considered during the calculation of the friction velocity based on the normalized velocity obtained near the wall:

$$u(z) = \frac{u^*}{\kappa} ln({}^{z}/{z_0}) \tag{19}$$

where $u(z)$ e is the free stream velocity [m/s] measured at a reference height, u^* is the friction velocity [m/s], κ is the von Karman constant, z is a reference height [m] and z_0 is the surface roughness height [m].

According to the US EPA emission model for diffuse sources of particulate matter, the friction velocity may be obtained from **Equation (19)** with the calculated velocity value at a given distance from the wall. The distance from the wall used in field measurements (full scale) is about 25 cm and the velocity measured is called u_s. The roughness height (z_0) is mainly dependent on the particle size distribution on each source. After manipulations on **Equation (19)** we are able to estimate the friction velocity as shown in **Equation (20)**:

$$u^* = \frac{\kappa}{ln\left(^{z}/_{z_0}\right)} u_s \tag{20}$$

An interesting fact in the US EPA modelling is the consideration of the effects of gusty winds on the erosion. For a given period, the gust wind (u_{10}^{+}) alters the value of the measured velocity by a ratio with the free stream mean velocity (u_r) that generated the erosion pattern. **Equation (21)** presents the final form of the friction velocity estimation which is dependent mainly on the gust wind velocity and on the roughness height:

$$u^* = \frac{\kappa}{ln\left(^{z}/_{z_0}\right)} \left(\frac{u_s}{u_r}\right) u_{10}^{+} \tag{21}$$

In order to explicitly account the effects of non-erodible particle on the emitted mass, Furieri (2012) developed the following expression for the erosion potential:

$$P_{mod} = b_1(\%EP)^{b_2}\,(u^* - u_t^*)^2 + c_1(\%EP)^{c_2}(u^* - u_t^*) \tag{22}$$

where $\%EP$ is the proportion of erodible particles. The constants b_1, b_2, c_1 and c_1 was found by the least squared method by fitting the experimental emitted mass results performed for stockpiles models with 50%, 65%, 80% and 90% of EP for the stream velocities of 6, 7 and 8 m/s. The values found were 0.0047, 3.90, -0.0007 and 3.90, respectively. Furieri (2012) obtained good agreement between the modified model and experimental results. In addition, the results lead to conclude that the USEPA model is very useful when the mixture has a high proportion of non-erodible particle, but it fails when this proportion decreases.

Taking advantage of dividing the stockpile into subareas, it is also possible apply the model of Ferreira et al. (2019a) developed for beds. The difference, however, remains in the criterion that controls the division. In Caliman (2017) and de Morais et al. (2018), an oblong stockpile was divided in subareas that presented the same angles θ in which the fluid flowed over the pile:

$$\theta = \text{arcsen}(\tau_z/\tau) \tag{23}$$

where τ is the shear stress over the stockpile surface and τ_z its vertical component, both, obtained numerically. Then, using the relation proposed by Iversen and Rasmussen (1994) it is possible to re-evaluate the particle threshold friction velocity for a flat surface ($u_t^*(0)$) and the one in an inclined surface ($u_t^*(\theta)$):

$$\frac{u_t^*(\theta)^2}{u_t^*(0)^2} = \cos\theta + \frac{\sin\theta}{\tan\xi} \tag{24}$$

where ξ is the angle of internal friction.

4. CONTEXTUAL REVIEW

This chapter presents a contextualization of this thesis regarding the research work on wind erosion on stockpiles of granular materials pursued by the air pollution research group at the Federal University of Espirito Santo.

4.1.1. Influence of non-erodible particles on aeolian erosion of granular material

Furieri et al. (2013a) focused on the analysis of the mean wall friction velocity on a surface composed by roughness elements exposed to a turbulent boundary layer. These roughness elements represent non-erodible particles over an erodible surface of an agglomeration of granular material. Furieri et al. (2013a) performed numerical simulations of the wind flow over a bed containing rough elements with non-uniform diameter-to-height ratios to evaluate the friction velocity evolution as the aeolian erosion occurs. From Furieri et al. (2013a) numerical simulations it was verified that **Equation (13)** from Turpin et al. (2010) work is also valid for a distribution of rough elements with different diameter-to-height ratios for cover rates of up to 12%.

On the other hand, instead of evaluating the wind erosion at particle level as Furieri et al. (2013a), Furieri et al. (2013b) experimentally studied the effects of non-erodible particles on wind erosion of oblong stockpiles models composed by sand. The tested configurations consisted of two different values of non-erodible particles cover rates, and three free stream velocities. The results from Furieri et al. (2013b) showed that the accumulation of non-erodible particles induces the pavement effect (cessation of erosion by the protective effect of non-erodible particles reflected by low shear zones around them that do not allow the minimum friction velocity of potentially erodible particles to be reached) in some regions of the pile. Furieri et al. (2013b) showed that, as the time goes by is possible to observe that the mass flow of particles decays faster when the pile is composed of a greater quantity of non-erodible particles, indicating that increasing the quantity of these elements in a mixture could reduce the amount of particles emitted.

Following the line of studies on the effect of non-erodible particles on particle emission, until 2019, there was no approach that reliably predicts the reduction in emissions caused by presence of non-erodible particles on an aggregate surface. So, Ferreira et al. (2019a) proposes an analytical model for beds composed by a simple equation that calculates the emitted mass through the final eroded bed height (H_f) (**Equation (15)**). To estimate H_f considering the pavement effect, Ferreira et al. (2019a) performed a series of simulations on rough beds to found the constants A, M and N for Turpin et al. (2010) equation **(Equation (13))** for non-erodible particle cover rates of up to 40%. In addition, wind tunnel experiments were carried out in order to broaden knowledge of the pavement phenomenon and validate the modelling. A bimodal particle size distribution of sand with white erodible and black non-erodible particles was used for three tested velocities and for two different non-erodible proportions. Three experimental measurements were carried out by continuous weighing of the emitted mass. Good agreement between the modelled and experimental emitted mass results was found paving the way for a possible application of the model to emission estimates from stockpiles which was done by De Morais et al. (2018).

De Morais et al. (2018) proposed to apply the Ferreira et al. (2019a) emission model developed for beds composed by bimodal granulometry to prediction of particle emission from stockpiles composed by multimodal granulometry. The specific objective was to evaluate the linearity of the relation between CR and H considering the presence of a multimodal distribution of particle sizes to validate the mathematical model applied to stockpiles with wind tunnel data. De Morais et al. (2018) proved analytically that the relationship between CR and H may still be considered linear for the tested mixture of particles. In addition, De Morais et al. (2018) applied the emission model developed by Ferreira et al. (2019a) for beds to oblong stockpiles. The modelled emission, when compared with experimental data, showed that the physical tendency of the aeolian erosion phenomenon was well predicted. The model proved to be useful in comparative analysis between scenarios but not in absolute values due to errors found.

4.1.2. Particles emission from ground areas surrounding stockpiles

Furieri et al. (2012) aimed to investigate the airflow characteristics in the near-ground surroundings of a single oblong stockpile for different wind flow directions. Wind tunnel experiments using an oil-film surface coating technique were carried out for near-wall flow visualization. Numerical simulation results were used to allow comparison analysis of flow features. The experimental investigations were performed in a wind tunnel in which a scaled-down stockpile model was set up. A single oblong stockpile was chosen with its shape and dimensions representative of typical coal storage piles. This model was made in wood to a scale ratio of 1:200. As the incoming wind flow direction is well known to highly influence the flow topology over the stockpile, three airflow angles of incidence were investigated: 90°, 60° and 30° for a single free-stream velocity. Numerical contours of wall shear stress and the flow visualization by the oil film technique for the tested configurations showed good agreement. Furieri et al. (2012) concluded that for the stockpile-oriented 90° to the wind main direction, typical topology of flow around wall-mounted obstacles were observed, notably a wake zone downstream the pile including two main counter-rotating vortices.

Furieri et al. (2014) moved forward quantifying the emission of particles from the stockpile surface using the United States Environmental Protection Agency (USEPA) emission model. The US EPA emission model is the most used model to estimate emissions from storage surface. It is known that friction velocity is not constant on the surface of the pile since the pile acts as an obstacle and modifies the flow around it. Therefore, depending on the geometry of the pile, different shear stress distributions may be found. The US EPA model takes this information as a basis and divides the pile into regions of the same normalized velocity u_s/u_r (where u_s is the surface velocity at 25 cm from the pile and u_r is the wind velocity at the free surface). Furieri et al. (2014) took advantage of the same strategy of US EPA model aiming to quantify the contribution of dust re-emission from the areas surrounding the piles in the total emission of an open storage yard. To obtain the total emission it was also necessary to estimate the particles emission from oblong stockpiles surfaces. Considering three angles of incidence of the incoming wind flow (30°, 60° and 90°), results of friction velocity from numerical modelling of fluid dynamics were used in the US EPA model to determine dust emission on and around a single stockpile. After the calculations using US EPA emission model, it was found that as the wind velocity increases, the contribution of particles re-emission from the ground area around the pile in the total emission also increases. The dust emission from the pile surface is higher for piles-oriented 30° to the wind direction. On the other hand, considering the ground area around the pile, the 60° configuration is responsible for higher emission rates (up to 67 %).

4.1.3. Influence of obstacles and their configuration on particles emission

Ferreira et al. (2019b) study aimed to investigate, through numerical and experimental simulation, the impact of different configurations of parallel stockpile piles on wind erosion and the effect on emissions of the proportion of non-erodible particles. The parameters analyzed were (i) wind velocity, (ii) the orientation of the piles to the main flow direction and (iii) the gap distance between the piles. Wind tunnel experiment was conducted in six configurations: one isolated pile and two successive piles separated by gaps of 0.9h and 1.8h (h is the pile height) oriented to 60° and 90° with respect to the main wind flow direction. The particles in the piles had a bimodal particle size distribution consisting of sand that was erodible (white) and non-erodible (black) in the investigated velocity range. The contrasting colors enabled the visualization of the non-erodible sand accumulation. Numerical simulations with identical configurations were performed to obtain the mean field of the wall shear stress distribution allowing the association with the experimental erosion patterns. The emitted mass was experimentally quantified as the difference between the initial and final stockpile weights. The comparison between the experimental and numerical results for the tested configurations showed that the most eroded areas are related to high levels of shear stress. Besides, the incoming wind flow, the presence of a parallel stockpile and the gap between them clearly influence the shear stress distribution over the stockpile surfaces. Ferreira et al. (2019b) conclude, mainly, that the downstream stockpile had a large impact on the aeolian erosion as it was highly eroded. The first assumption is that the downstream stockpile was highly eroded because of the impact of the particles emitted from the upstream stockpile. In addition, the emissions of the two consecutive stockpiles were greater than twice the emissions from an isolated stockpile for both orientations. Emissions were lower for configurations in which the piles were perpendicular to each other and to the incoming wind flow.

4.1.4. Lagrangian approach for simulation of suspension and deposition of particulate matter

Nascimento (2014) aimed to investigate the dispersion and deposition of particulate matter emitted from an oblong stockpile surface. The Euler-Lagrange modelling for the atmospheric dispersion of particles was used, being the Eulerian description for wind airflow and the Lagrangian description for particle movement. To account turbulent effects, Large-Eddy Simulation (LES) was performed. In general, the particle concentration varies mainly from 0.10

to 10.6 μg/m³, except for two zones on the sides, with values around 20.6 μg/m³. This could indicate that (i) the stockpile sides are responsible for the highest particles emissions, and this large amount of particles are dragged, and the same values are observed in the plume along with the entire domain or/and (ii) at the end of the domain many particles lost kinetic energy and deposited. Despite this, as expected, the plume spread vertically and horizontally along the flow direction. The authors observed that particles, along the flow direction, above the stockpile height, reach velocities close to the free stream velocity. Particles with larger velocity, above free surface velocity, was also observed in regions where the fluid is accelerated. A recirculation zone developed downstream the stockpile, as expected. In this recirculation zone particles are in large quantities and their velocity is very low. Despite this, the particles in this region have the smallest diameters, probably because they were emitted from the stockpile surface, at zero velocity, not having enough kinetic energy to escape from the turbulence formed downstream the stockpile.

5. METHODOLOGY

The first specific objective is analyze the influence of different configurations of successive stockpiles on re-emission potential of particle from its surroundings. The experimental work and numerical simulations used to achieve this objective were conducted by Furieri (2012) and are briefly described in section 5.1.1 and 5.2.1, respectively. The contribution of the present thesis regards the analysis of the influence of different configurations of successive stockpiles on the estimation of particle re-emission from its surroundings. The methodology to calculate the total particles emission from the stockpiles is based on US EPA emission model and can be found in 5.2.2. Results are presented in Section 6.1.

The second specific objective is to assess the influence of non-erodible particles on the development of fluid flow structures responsible for the entrainment of erodible particles. To achieve this objective, numerical simulations using LES were performed in the present thesis as described in section 5.2.3, and their validation was carried out using the experimental data of Durst et al. (1987) and the direct numerical simulations of Kim et al. (1987) for smooth wall described in section 5.1.2 and 5.1.3, respectively. The methodology applied to calculate the probability function distribution of the friction velocity on the rough surface is described in section 5.2.4. Results are presented in form of a scientific paper in Section 6.2.

The third specific objective consists in evaluating the similarity requirements of wind flow, particle entrainment and particle transport in wind tunnel experiments. To evaluate the similarity requirements for a representative wind tunnel simulation of real scale scenarios, only theoretical arguments were used. The Buckingham Pi Theorem was applied in the present thesis to help finding dimensionless numbers to describe the relative effect of cohesive and gravity forces that can explain the non-erodibility of particles. Additionally, Stokes number was used to discuss similarity in saltation and suspension movements of erodible particles. Results are presented in form of a technical note in Section 6.3.

5.1. Description of experimental works used in this study

The experimental work conducted by Furieri (2012) is shortly described in section 5.1.1. His experimental data were used to investigate the impact of wind flow affected by the presence of multiple obstacles on particles emission from granular stockpiles.

The experimental work conducted by Durst et al. (1987) and the direct numerical simulation of Kim et al. (1987) are described in sections 5.1.2 and 5.1.3, respectively. Their data were used to validate the numerical simulations performed to assess the influence of non-erodible particles on the development of fluid flow structures responsible for the entrainment of erodible particles.

5.1.1. Furieri (2012) experimental work

Furieri (2012) experimental work aimed to evaluate and quantify the erosion potential of regions around successive piles. Full details of the experimental work can be found in Furieri (2012). The experiment was conducted in the wind tunnel facilities at the Industrial Energy Department (IMT Nord Europe, Douai, France). The surface oil-film technique was used to investigate the fluid flow pattern over and around successive wood stockpiles surfaces. This experimental approach offers two-dimensional visualization with a good spatial resolution of the shear stress distribution associated to aeolian erosion. This technique consists of coating an oil mixture over a given wall exposed to flow friction. A thin layer of the mixture is coated over a surface around an object in which the wall flow pattern is analyzed. Wind flow overpasses the test section with oil-film mixture layer and creates some changes to its initial pattern. Due to friction forces, the wall flow features are then revealed, and color variation is directly linked to wall shear stress distribution on the coated surface.

The oil-film mixture used in this work had three components: (i) oil, (ii) small particles which are the solid part (yellow colored powder in the present work) and (iii) a chemical agent which allows the mixing between the other two components. As proposed by Desreumaux and Bourez (1989), the paraffin oil was used as the oil part and the oleic acid as the mixing component. Several tests were performed to adjust the proportion of each component to the values that allowed the experiments to be carried out: 128 g/m² of paraffin oil, 5 g/m² of yellow dye and 23 drops/m² of oleic acid. The experimental work was performed in the wind tunnel presented in **Figure 13**. A photographic camera with resolution of 6 million pixels was placed right above the scaled-down successive stockpiles models capture the oil movement according to the wind flow. The wood stockpiles placed in the wind tunnel were built considering the proportion of 1:200 relative to a full-scale coal stockpile (38° of angle of internal friction).

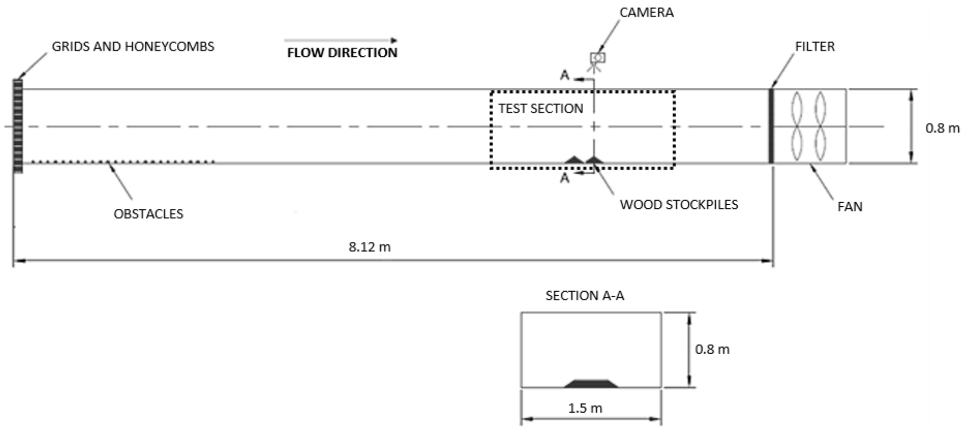

Figure 13. Schema of wind-tunnel experimental set-up for fluid flow over and around two successive stockpiles (the dimensions are in meters).

Table 3 presents the stockpiles dimensions and the experimental cases. For all tested configurations, the free stream velocity of 6.5 m/s was used. Successive shots at each 15 min were taken until no significant modification between two consecutive photographs was identified. At this time, usually 5 hours, the experiments were stopped.

Table 3. Experimental configuration investigated.

Pile configuration and dimensions	Wind direction	Gap*		Free-stream velocity
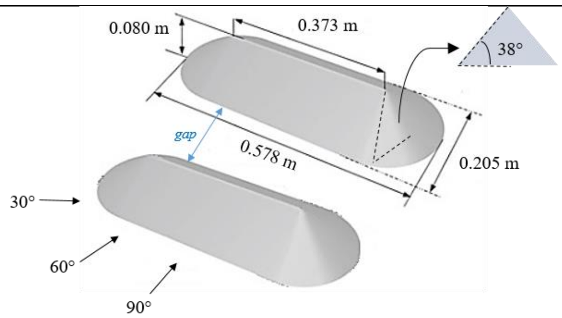	30°	1e	30°	6.5 m/s
	60°	2e	60°	
	90°	2e	90°	

5.1.2. Experimental work of Durst et al. (1987)

Durst et al. (1987) performed their investigation in a closed-circuit wind tunnel. It consisted of chamber with wire meshes followed by a contraction with an area ratio of 10:1 entering an 8 m long test section. The cross-sectional shape of the wind tunnel was octagonal with an internal diameter of 1.5 m. The entire roof of the test section was adjustable to permit flow investigations at zero longitudinal pressure gradient. The investigated boundary layer developed along a flat plate made of Formica 6 m long which was installed horizontally inside the test section 30 cm from the tunnel floor.

The traversing mechanism used in Durst et al. (1987) study for the hot-wire probes was installed inside the wind tunnel and was driven by an automatic, externally located position control. For measurements close to the wall, the relative motion of the probe was also checked independently by means of a precision dial gauge of 1 um positioning accuracy. Special care was taken to position the prongs of the probe parallel to the wall in order to approach the surface as closely as possible and to minimize flow disturbances by the wire prongs and probe support. At higher flow velocities, the hot-wire probes were inclined with respect to the wall surface by up to about 5° in order to permit measurements inside the viscous sublayer of the flow. Streamwise velocity measurements were performed with standard hot-wire anemometer equipment consisting of DISA P05 gold-plated boundary-layer probe operated with a DISA 55M01 constant temperature anemometer. The overheat ratio for the hot wire was 1.8 and the wire was calibrated for this fixed overheat in the range 0.3 m/s-40 m/s using the modified DISA 55D90 calibration equipment. All hot-wire data, including the calibration data, were recorded on-line by a data acquisition system based on a Hewlett-Packard minicomputer facilitated with a fast- Fourier Analyzer.

5.1.3. Direct numerical simulation data of Kim et al. (1987)

Kim et al. (1987) performed a direct numerical simulation of a turbulent channel flow (here presented as experimental data). The unsteady Navier-Stokes equations were solved numerically at a Reynolds number of 3300, based on the mean centerline velocity and channel half-width, with 3962880 grid points (192x129x160, in x, y z). All essential turbulence scales were resolved on the computational grid and no sub grid model was used. A large number of turbulence statistics were computed and compared with the existing experimental data at comparable Reynolds numbers.

For the Reynolds number considered, the streamwise and spanwise computational size were 2300 and 1150 in wall units, respectively. With this computational domain, the grid spacings in the streamwise and spanwise directions are respectively $\Delta x^+ = 12$ and $\Delta z^+ = 7$ in wall units. The first mesh point away from the wall was at $y^+ \approx 0.05$, and the maximum spacing (at the centreline of the channel) was 4.4 wall units. The initial velocity field used by Kim et al. (1987) was obtained from the large-eddy simulation of Moin and Kim (1982).

5.2. Mathematical and numerical modelling

The setup of the numerical simulations over two stockpiles models carried out by Furieri (2012) is presented in section 5.2.1. These data were used in the present thesis as input data to evaluate the influence of different configurations of successive stockpiles on the estimation of particle re-emission from its surfaces and surroundings. The numerical simulations set up of Furieri (2012) considered steady-state flow. According to the author, this approach was chosen because the simulation objectives focused on average flow characteristics and not on short-term transient variations. The objective of these numerical simulations was to obtain the distribution of shear stress on and around stockpiles and obstacles in the final stage of erosion, which is used in the US EPA model to estimate particles emission. Besides, variations between the beginning and end of erosion which, in terms of wind gusts, are very fast. Thus, the steady regime allowed a reasonable approximation as seen in previous works presented in the literature review. The turbulence model $k - \omega$ Shear-Stress Transport (SST) was used. It is well-suited for steady-state simulations of complex boundary layer flows under adverse pressure gradients. The model was chosen based on a study performed by Badr and Harion (2005) who simulated analogous configurations under similar flow conditions and compared the results obtained using different closure models.

The setup of the numerical simulation of fluid flow over a bed containing non-erodible elements performed for the present thesis is presented in section 5.2.3. The data obtained from these numerical simulations were used to assess the influence of non-erodible particles on the development of fluid flow structures responsible for the entrainment of erodible particles. The Large-Eddy Simulation (LES) was used to account for the turbulence effects. This technique resolves part of the large scales of turbulence, therefore, does not allow for a steady state solution. Thus, simulation was carried out in a transient regime. In this case, the temporal variations of the shear stress (or friction velocity) are important for the construction of Probability Density Functions (PDFs) from the time series of friction velocity used to as a probabilistic approach given the stochastic nature of the erosion phenomenon. It is important to point out that the validation of the numerical simulations was performed only for the smooth wall as there was no experimental data available to validate the simulations concerning the rough wall.

5.2.1. Fluid flow on and around successive stockpiles (Furieri, 2012)

The three-dimensional equations of mass and momentum conservation were solved using the software Ansys Fluent®. The chosen turbulence model was $k - \omega$ SST. The steady-state regime was also considered. The mesh was produced by extrusion of triangular cells defined on stockpiles walls and the ground surface. The size of the first wall cell was chosen to be at least $z^+ \approx 4$ in agreement to requirements by the use of turbulence model ($k - \omega$ SST) without any wall functions ($z^+ < 5$), building a mesh of more than 5 million elements. **Figure 14** shows the domain dimensions and boundary conditions.

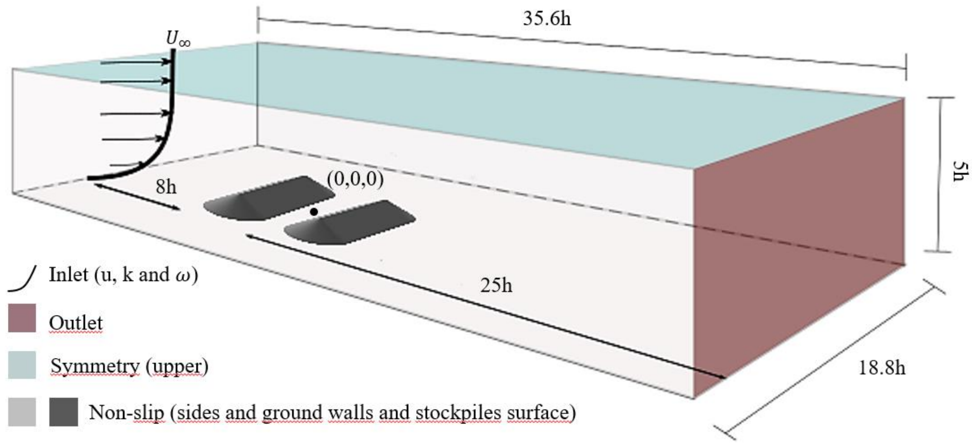

Figure 14. Domain dimensions and boundary conditions. The origin of the domain is between the stockpiles. The coordinate x represents the streamwise direction, y represents the spanwise direction and z the domain height.

Full details of the numerical simulations can be found in Furieri (2012). The numerical result from his work was used as input data for the calculations of emitted mass performed in the present thesis.

5.2.2. US EPA emission model

In order to evaluate the influence of different configurations of two successive stockpiles on the estimation of particle emission from its surfaces and surroundings four gusts were considered: 5, 6.5, 10 and 15 m/s. Coal was considered on both stockpile surface and the surrounding regions (threshold friction velocity equals 0.35 m/s according to Turpin and Harion (2009). The emissions were calculated for the erodible area surrounding the pile (ESEA) and for the pile erodible area (EPEA) to discuss the influence of the tested configurations in global particles emission. The emission for erodible areas surrounding the pile (SEA) and pile erodible area (PEA) were also calculated. All calculations of particles emission were performed through US EPA model already described in the Literature Review, Section 3.6.

5.2.3. Turbulent flow over a bed containing non-erodible particles

It is important to highlight that the emission calculations were performed using the US EPA model. In this model, the friction velocity assumes a value at a specific location in the stockpile or bed surface. However, the friction velocity is a stochastic variable and can vary in time and space as a function of the surface properties and the turbulent structures that develop when the wind flows over it.

The present work calculates the friction velocity using the numerical simulations results. The physical model consists of a bed composed of 20% of cylindrical non-erodible elements surrounded by smooth wall that represent the erodible particles. As the wind flows over the bed surface, it is expected to identify coherent turbulent structures development and their upward movement that can be associated with the emission of particles. The stochastic nature of friction velocity was accounted in the emission model by means of Probability Density Functions (PDFs) determined from the time series of friction velocity over the particle bed calculated using the Large-Eddy Simulations (LES) technique. The PDFs obtained for a smooth wall, represented by the top wall of the wind tunnel, and the PDFs obtained for a rough wall, represented by the bed surface containing non-erodible particles were compared. It was considered that the top of the domain could keep all the characteristics of a smooth bed as long as the distance of up to $y^+ = 30$ from the wall is respected. It is important to point out that the validation of the mathematical model and the numerical solution of the smooth wall of the computational domain, was achieved by means of the work of Durst et al. (1987) and Kim et al. (1987).

Figure 15 shows the computational domain representative of the physical model, the roughness elements, and its dimensions in wall units. Ansys Meshing® software was used to construct a hexahedral mesh of 4,188,797 elements whose details are shown in **Figure 16**. **Figure 16a** shows the refinement in the top and bottom. **Figure 16b** shows the mesh of the roughness elements inside the domain.

To reach LES model requirements, the minimum element size on the walls was about 10^{-4} m and the time step 2.5×10^{-5} s. The minimum size was obtained considering $y^+ = \frac{yu^*}{\nu} < 1$.

Taking the Kolmogorov length scale (l_0) as an important parameter, which is 4.8×10^{-5} m in this case, the minimum filter size (Δ) was assumed as 8.5×10^{-5} m, thus, $\Delta > l_0$. In a domain with rough elements the appropriate time step can be estimated by $\Delta t = 0.002T_c$ (Xie et al., 2008) where $T_c = H_{elements}/u^*$. As the element height is 0.002 m and the estimated friction velocity is 0.12 m/s, the maximum value for Δt is 0.00004 s. Thus, Δt was chosen as 2.5×10^{-5} s.

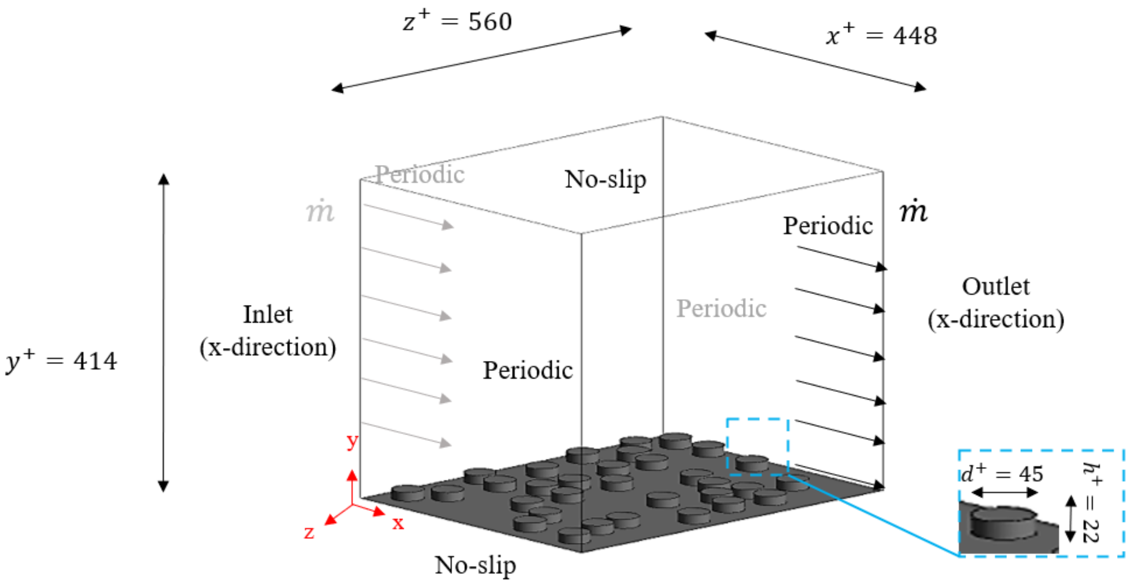

Figure 15. Schema of the computational domain, its dimensions in wall units and the boundary conditions applied.

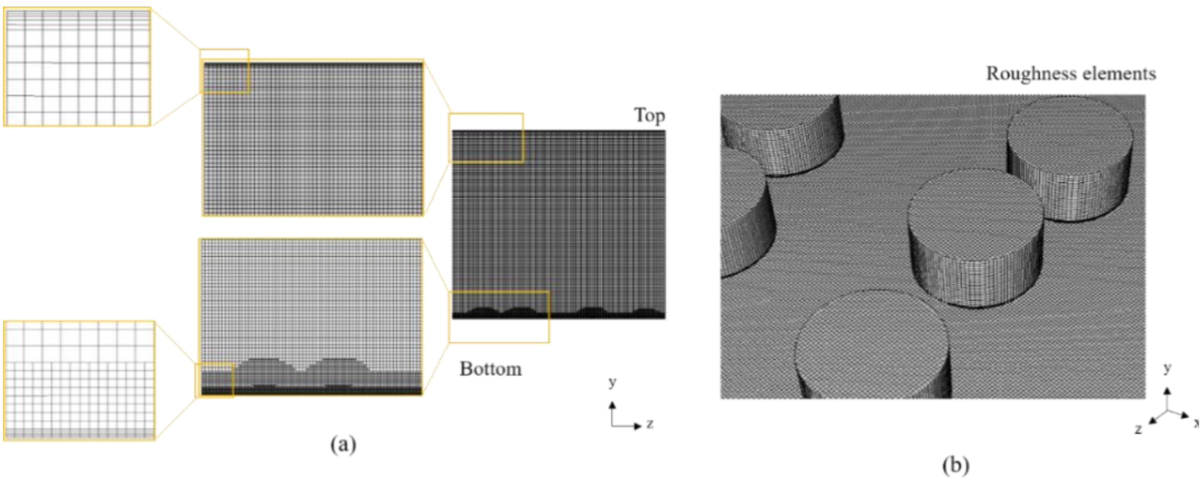

Figure 16. (a) Mesh details of the side showing the refinement in the solid walls and (b) of the roughness elements.

The Large Eddy Simulation (LES) model was initially proposed by Smagorinsky (1963) for atmospheric flow prediction and first applied to engineering research by Deardorff (1970a) and

Schumann (1975). The model is based on the Kolmogorov (1941) energy cascade theory stating that most of kinetic energy of turbulence is injected from the mean flow to the smallest wave numbers of vortices (or eddies), i.e., the largest ones. In the inertial subrange of the energy cascade only energy transfer occurs between the vortices by the successive breaking of them into smaller and smaller ones. The process comes to an end with the viscous dissipation of the smallest vortices in the form of heat. **Figure 17** shows the energy cascade (k is the wave number) LES consists of applying, on the governing fluid flow equations, a spatial filtering operation to separate the larger and smaller eddies in a certain cutoff width (Δ). During spatial filtering, information relating to filtered-out turbulent eddies is destroyed. The method proposes to directly solve the scales larger than the cutoff width and account the small scales effects through models (sub-grid-scale SGS models), since they have a small fraction of energy and are considered to have universal and isotropic behaviors.

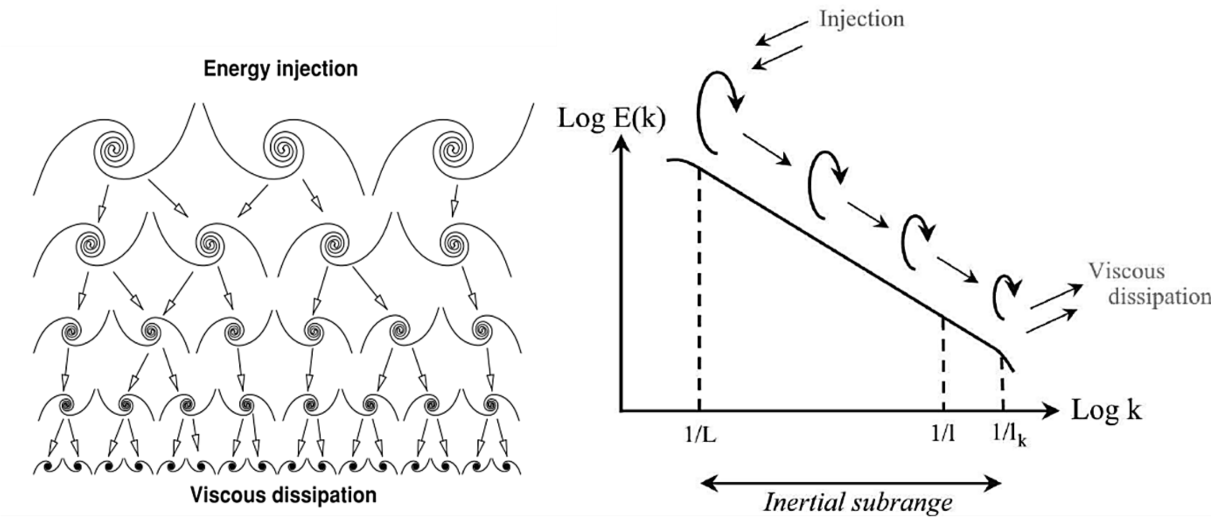

(a) (b)

Figure 17. Energy cascade where k is the wave number. Adapted from (Nazarenko, 2011).

The filtering process consists of a convolution operation between a filter function (G) and any flow variable ($f\ (x_i, t)$), varying in time (t) and space (x_i), that will always be a sum of the resolved larger scales ($\overline{f}\ (x_i, t)$) and the modeled smaller scales ($f\ '(x_i, t)$):

$$f\ (x_i, t)\ =\ \overline{f}\ (x_i, t)\ +\ f\ '(x_i, t) \tag{25}$$

where i = 1, 2, 3 and the overbar represents the spatial filtered variables. So, applying the filter operation:

$$\overline{f}(x_i,t) = \iiint_{-\infty}^{+\infty} G(x_i, x_i', \Delta)\, f\,(x_i,t)\,dx_i \tag{26}$$

According to Versteeg and Malalasekera (2007), despite there are several filters, such as Gaussian and sharp cut-off filters, the top-hat or box filter, presented in **Equation (27)** is used in finite volume implementations of LES. **Figure 18** shows the energy spectrum after filtering operation for some filters.

$$\mathrm{G}(x_i) = \begin{cases} \dfrac{1}{\Delta^3} & \text{if } |\mathrm{x_i}| \leq \dfrac{\Delta}{2} \\ 0 & \text{otherwise} \end{cases} \tag{27}$$

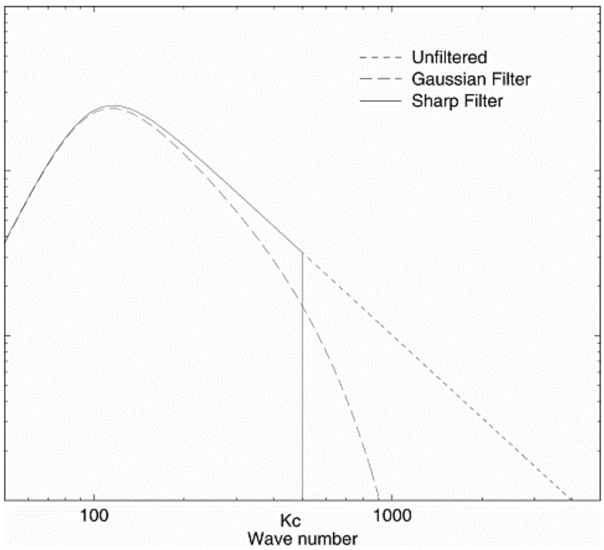

Figure 18. Energy spectrum of the unfiltered and filtered solutions. Filters considered are a projective filter (sharp cutoff filter) and a smooth filter (Gaussian filter) with the same cutoff wave number of 500 (Sagaut, 2006).

In theory, cutoff width (Δ) can be defined as any size, but it is pointless to select a cutoff width smaller than the grid size. This happens because, in this type of computation, only a single nodal value of each flow variable is taken on each grid cell, so all finer detail is lost anyway. The most common is to take the cutoff width to be of the same order as the grid size (Versteeg and Malalasekera, 2007):

$$\Delta = \sqrt[3]{\Delta_1 \Delta_2 \Delta_3} \tag{28}$$

Thus, applying the top-hat filter, the filtered variable is reduced into a finite integration in a finite space:

$$\overline{f}(x_i,t) = \frac{1}{\Delta^3} \iiint_{-\Delta/2}^{\Delta/2} f\,(x_i,t)dx_i \tag{29}$$

Continuity and Navier-Stokes time-dependent flow equations after applying a filter are:

$$\frac{\partial \bar{u}_i}{\partial x_i} = 0 \tag{30}$$

$$\frac{\partial \bar{u}_i}{\partial t} + \frac{\partial}{\partial x_j}\left(\overline{u_i u_j}\right) = -\frac{1}{\rho}\frac{\partial \bar{p}}{\partial x_i} + \nu \frac{\partial}{\partial x_j}\left(\frac{\partial \bar{u}_i}{\partial x_j} + \frac{\partial \bar{u}_j}{\partial x_i}\right) \tag{31}$$

A closure problem arises in **Equation (31)** due the non-linear term $\overline{u_i u_j}$ that cannot be solved. In order to find a solution for this problem, Leonard (1974) proposed the following approach in order to rewrite the non-linear term considering that the decomposition $u_i = \overline{u_i} + u_i'$ can be applied.

Decomposing the term $\overline{u_i u_j}$:

$$\overline{u_i u_j} = \overline{(\overline{u_i} + u_i')(\overline{u_j} + u_j')} \tag{32}$$

and performing the distributive property, we obtain:

$$\overline{u_i u_j} = \overline{\overline{u_i}\,\overline{u_j}} + \overline{\overline{u_i} u_j'} + \overline{u_i' \overline{u_j}} + \overline{u_i' u_j'} \tag{33}$$

The terms that do not depend only on large scales are grouped:

$$C_{ij} = \overline{\overline{u_i} u_j'} + \overline{u_i' \overline{u_j}} \tag{34}$$

$$R_{ij} = \overline{u_i' u_j'} \tag{35}$$

where C_{ij} is the Cross-stress tensor, related to the interaction between the resolved and sub-grid scales and R_{ij} is the SGS Reynolds stress tensor, which reflects the effects of the sub-grid eddies.

The decomposition of the non-linear term results in the following filtered equation:

$$\frac{\partial \bar{u}_i}{\partial t} + \frac{\partial}{\partial x_j}\left(\overline{\overline{u_i}\,\overline{u_j}}\right) = -\frac{1}{\rho}\frac{\partial \bar{p}}{\partial x_i} + \nu \frac{\partial}{\partial x_j}\left(\frac{\partial \bar{u}_i}{\partial x_j} + \frac{\partial \bar{u}_j}{\partial x_i}\right) - \frac{\partial \tau_{ij}}{\partial x_j} \tag{36}$$

where τ_{ij} is called subgrid-scale (SGS) stress tensor defined as (Sagaut, 2006):

$$\tau_{ij} = C_{ij} + R_{ij} \tag{37}$$

Note that we still have a problem with the filtered **Equation (36)**. We would need to apply the filter again in the term $\overline{\overline{u}_i \overline{u}_j}$. Some mathematical assumptions and manipulations lead to:

$$\overline{\overline{u}_i \overline{u}_j} = \left(\overline{\overline{u}_i \overline{u}_j} - \bar{u}_i \bar{u}_j\right) + \bar{u}_i \bar{u}_j \tag{38}$$

$$\overline{\overline{u}_i \overline{u}_j} = L_{ij} + \bar{u}_i \bar{u}_j \tag{39}$$

where the L_{ij} tensor is called the Leonard tensor and represents the interactions between the large scales.

Thus, the filtered equation is:

$$\frac{\partial \bar{u}_i}{\partial t} + \frac{\partial}{\partial x_j}\left(\bar{u}_i \bar{u}_j\right) = -\frac{1}{\rho}\frac{\partial \bar{p}}{\partial x_i} + \nu \frac{\partial}{\partial x_j}\left(\frac{\partial \bar{u}_i}{\partial x_j} + \frac{\partial \bar{u}_j}{\partial x_i}\right) - \frac{\partial \tau_{ij}}{\partial x_j} \tag{40}$$

where the subgrid-scale stress tensor is:

$$\tau_{ij} = C_{ij} + R_{ij} + L_{ij} = \overline{u_i u_j} - \bar{u}_i \bar{u}_j \tag{41}$$

Clark et al. (1979) suggested to express the sum of these tensors as a Taylor expansion of the filtered velocity field. Based on this assumption, Findikakis and Streeter (1979) have developed an approximate expression for these terms calculating them explicitly as a function of filtered velocity field:

$$C_{ij} + L_{ij} \cong \frac{\Delta_i}{12}\frac{\partial \bar{u}_i}{\partial x_j}\frac{\partial \bar{u}_j}{\partial x_i} \tag{1}$$

Other expression for these terms can be also find in Ferziger (1977). However, other authors have reported that these two tensors could be neglected.

Shaanan et al. (1975) estimated that for a convective transport scheme of second order, the Leonard and Cross-stress tensors can be neglected. On the other hand, Silveira-Neto et al. (1993), in numerical experiments on a sudden expansion, showed that even for third order schemes these two tensors can be negligible compared to the SGS Reynolds stress tensor being more of an order of magnitude smaller, results compared to those obtained years before by Amtonopoulos-Domis (1981). So, it is possible assume that $\tau_{ij} = R_{ij}$.

The problem remains in finding R_{ij} in order to achieve the closure for momentum equation. The most widely used SGS models are based on the concept of turbulent viscosity that relates the SGS stress tensor with resolved-flow strain rates according to Boussinesq (1877) approximation. The SGS Reynolds stress tensor are taken to be proportional to the local rate of strain of the resolved flow ($\bar{S}_{ij}$):

$$\bar{S}_{ij} = \frac{1}{2}\left(\frac{\partial \bar{u}_i}{\partial x_j} + \frac{\partial \bar{u}_j}{\partial x_i}\right) \tag{42}$$

$$R_{ij} = -2\mu_{SGS}\bar{S}_{ij} + \frac{1}{3}R_{ii}\delta_{ij} = -\mu_{SGS}\left(\frac{\partial \bar{u}_i}{\partial x_j} + \frac{\partial \bar{u}_j}{\partial x_i}\right) + \frac{1}{3}R_{ii}\delta_{ij} \tag{43}$$

where μ_{SGS} is the dynamic sub-grid-scale viscosity.

The Smagorinsky-Lilly sub-grid model was used based on similar studies (Xie and Castro, 2006; Xie et al., 2008). The original model of Smagorinsky is based on the hypothesis that the production and dissipation of the small scales are equal, leading to the following equation:

$$\mu_{SGS} = \rho(C_s\Delta)^2\bar{S} \tag{44}$$

where $\bar{S} = \left(2\bar{S}_{ij}\bar{S}_{ij}\right)^{1/2}$ and C_s is the Smagorinsky constant, which varies according to the flow characteristics.

Differently from the original Smagorinsky SGS model, in the Smagorinsky-Lilly SGS model, the SGS turbulent viscosity is modelled by:

$$\mu_{SGS} = \rho(L_s)^2\bar{S} \tag{2}$$

where $L_s = min(\kappa d, C_s\Delta)$ (L_s is the Smagorinsky length analogous to the Prandtl's mixing length associated with sub-grid scales), κ is the Von Kármán constant, d is the distance to the closest wall, C_s is the Smagorinsky constant, and Δ is the local grid scale ($\Delta = (\Delta x\Delta y\Delta z)^{1/3}$).

This SGS model proposed by Lilly is a damping function that ensures a reduction of the turbulent viscosity to capture well the energy contained within the viscosity-affected layer in the near wall regions. The Smagorinsky constant is strongly dependent on the type of the flow due the effect of the mean flow strain or shear. This indicates that the behavior of the small eddies is not as universal as supposed at first and that an accurate LES modeling might require case-by-case adjustment of C_s (Versteeg and Malalasekera, 2007). This dependence has important side effects when dealing with parietal flows, due to the high velocity gradients that cause excessive production of SGS turbulent viscosity. Thus, the Smagorinsky-Lilly SGS model represents a solution for the to the biggest limitation of the original Smagorinsky model.

As it is not always possible to determine a constant for each case, the values used are usually searched in the literature. There are many acceptable proposals for the value of the Smagorinsky constant. Lilly (1966, 1967) suggested values of C_s between 0.17 and 0.21. Rogallo and Moin 91984) values between 0.19 and 0.24. However, based on Deardorff (1970b) work, Rogallo and Moin (1984) also established that high values of C_s promote excessive damping near solid walls, suggesting that C_s equal to 0.1 would be most appropriate.

In the present thesis, the chosen value was C_s equal to 0.1, which is commonly used to simulate fluid flows over similar geometries (Xie et al., 2008).

To obtain initial conditions for LES, Reynolds Averaged Navier-Stokes (RANS) simulations was performed using the $k - \omega$ Shear-Stress Transport (SST) model. For both simulations, RANS and LES, the boundary conditions are shown in **Table 4**. For upstream and downstream (x-direction) boundaries the periodicity condition with mass flow rate of 0.0051 kg/s was assumed. On the lateral sides (z-direction), the periodicity condition was also assumed, but the fluid flows in order that the mass balance within the domain is guaranteed. For top and bottom boundaries and rough surface it was assumed non-slip conditions.

Table 4. Mathematical and physical meanings of the boundary conditions.

Domain Location	Boundary conditions	
Upstream and downstream boundaries	$\dot{m} = \rho_f U_\infty A = 0.0051$ kg/s where A is the cross-sectional area of the computational domain and U_∞ the free stream velocity.	Periodicity condition. The mass flow rate at the entrance is equal to the mass flow rate at the outlet.
Lateral boundaries	-	Periodicity condition.
Top and bottom boundaries and rough surface	$\bar{u}_i = 0$	No-slip condition. The flow assumes the velocity of the wall.

It is important to point out that the mass flow rate is set on the upstream and downstream boundaries (x-direction) of the domain. On the sides (z-direction), the fluid flows in order that the mass balance within the domain is guaranteed.

Ansys Fluent® Computational Fluid Dynamics software was used to solve the governing equations. The discretization is performed by the software using finite volume, a method in which conservation equations are described in integral form for each volume. Patankar (1980) and Versteeg and Malalasekera (2007) give details about this method. **Table 5** presents the discretization schemes used. It is important to highlight that the convergence of the simulation was evaluated based on the mean velocity, root square mean, skewness, and flatness in the x direction. When these parameters no longer showed changes over time, it was considered that the simulation had converged.

For the model validation, typical turbulence statistics results obtained using LES were compared with experimental and Direct Numerical Simulation (DNS) data of Durst et al. (1987) and Kim et al. (1987), respectively. The validation of the mathematical model and the numerical solution for the turbulent incompressible flow was performed considering the smooth wall as reference since no experimental data was available for the rough wall investigated in the present work.

Table 5. Solution methods used in the simulations.

Term	Model	Interpolation scheme
Pressure-velocity coupling	RANS, LES	SIMPLEC
Gradient	RANS, LES	Green-Gauss cell based
Pressure	RANS, LES	Second order
Momentum	RANS	Second order upwind
Turbulent kinetic energy	RANS	Second order upwind
Specific dissipation rate	RANS	Second order upwind
Transient formulation	LES	First order implicit
Momentum	LES	Bounded central differencing

Durst et al. (1987) carried out investigations of probability density distribution of the streamwise velocity fluctuations $(u - \bar{u})$ normalized by the Root Mean Square (RMS) value. Their measurements were compared with LES results from the present work in the following dimensionless distance from the wall (y^+): 2.788, 5.015, 12.575, and 28.430.

Kim et al. (1987) modeled a turbulent flow over a smooth open channel using the direct numerical simulation (DNS) technique. Normalized general characteristics of computed turbulence statistics as velocity, Root Mean Square (RMS), Skewness $(S(u'))$, and Flatness $(F(u'))$, respectively, in function dimensionless distance from the wall (y^+) described below for x-direction, for instance, were compared with LES results from the present work.

$$u^+ = \frac{(u - \bar{u})}{u^*} \tag{45}$$

where u is the velocity in x-direction [m/s], $\bar{u}$ is the mean velocity [m/s], and u^* is the friction velocity [m/s] taken at smooth wall.

$$\frac{u_{RMS}}{u^*} = \frac{\sqrt{\overline{u'^2}}}{u^*} \tag{46}$$

where u' is the velocity fluctuation [m/s] in x-velocity.

$$S(u') = \frac{\overline{u'^3}}{\left(\overline{u'^2}\right)^{3/2}} \tag{47}$$

$$F(u') = \frac{\overline{u'^4}}{\left(\overline{u'^2}\right)^{2}} \tag{48}$$

An online tool was used to extract numerical data from images of plots of works of Durst et al. (1987) and Kim et al. (1987).

5.2.4. Calculation of the probability density distribution of the friction velocity in a turbulent boundary layer

From the numerical simulations we obtained the products of velocity fluctuations ($u'v'$, $v'w'$) at points in the smooth and rough domains. The friction velocity was calculated by the definition of shear stress:

$$\tau = \rho\sqrt{(u'v')^2 + (v'w')^2} \tag{49}$$

where τ is the shear stress [Pa], ρ is the air density [kg/m^3], and u', v', and w' is the velocity fluctuations in x, y and z [m/s] directions, respectively. Manipulating **Equation (49)** we find the friction velocity:

$$\frac{\tau}{\rho} = \sqrt{(u'v')^2 + (v'w')^2} \tag{50}$$

$$\sqrt{\frac{\tau}{\rho}} = \sqrt{\sqrt{(u'v')^2 + (v'w')^2}} \tag{51}$$

$$u^* = [(u'v')^2 + (v'w')^2]^{\frac{1}{4}} \tag{52}$$

Using the time records, the Probability Density Function (PDF) was calculated. Before calculating the PDF, the u^* data was divided into intervals:

$$\Delta u^* = \frac{u^*_{max} - u^*_{min}}{N_c} \tag{53}$$

where max m and min represents the maximum and minimum values of u^*, respectively. N_c is the number of classes.

The $p(u_i^*)$ was calculated by dividing the number of occurrences of each interval (N_i) by the total sample size (N) multiplied by the interval width (Δu^*):

$$p(u_i^*) = \frac{N_i}{N\Delta u^*} \tag{54}$$

6. RESULTS

Section 6.1 presents the results concerning the first specific objective which consists in investigating of the influence of different configurations of successive stockpiles on the estimation of particle re-emission from its surfaces and surroundings in a non-local point of view.

Section 6.2 shows the results concerning the second specific objective which consists in the assessment of the influence of non-erodible particles on the development of fluid flow structures responsible for the entrainment of erodible particles. The results are presented as a full paper not yet submitted for publication. It shows a qualitative and quantitative evaluation, at particle level, of the turbulent structures development and its influence on smooth and rough walls by means of quadrant, omega criterion and Probability Density Functions (PDF) analysis.

Section 6.3 presents the theoretical discussion of the similarity requirements of wind flow, particle entrainment and particle transport in wind tunnel experiments. The results are presented as a technical note not yet submitted for publication.

In the Appendix, we present additional works carried out during the pursuit of this thesis related to the thesis subject. The works are collaborative research articles led by other researchers from the Air Quality Research Group at the Federal University of Espirito Santo.

6.1. The influence of multiple stockpiles on particles re-emission of its surroundings

The potential re-emission from the ground around successive stockpiles was effectively calculated as the mass emitted from the erodible stockpiles surroundings (ESEA) using the US EPA emission model. Additionally, the emission from the erodible surface of the stockpiles (EPEA) was also estimated for later comparison with the re-emitted massfrom the surrounding areas (ESEA/EPEA). **Figure 19** shows heatmaps for all tested cases, where cooler colors mean lower emission values and warmer colors indicate higher emission values.

Figure 19a shows EPEA, the emission from piles erodible area for different configurations and wind velocities. The pile configuration variable shows various stockpiles configurations (one pile, two piles with gap of 1e, two piles with gap of 2e) at different wind directions (30°, 60°, 90°). The wind speed variable shows different wind gusts tested (5 m/s, 6.5 m/s, 10 m/s, 15 m/s). It is observed that, for instance, two piles oriented 60° to the incoming flow with 1e gap considering 15 m/s, there is a maximum value recorded at around 10 g. Lower values (in blue) are predominant at lower wind speeds and in single stockpiles configurations.

Figure 19b shows ESEA, the emission from surrounding erodible area for different configurations and wind velocities, which is evaluated as re-emission since most of the particles around the piles probably come from the stockpiles themselves. For two piles oriented 60° to the incoming flow with 1e gap considering 15 m/s, there is an even higher maximum value recorded, above 20 g. The pattern is similar to the first map (**Figure 19a**), but with higher overall values, especially at higher wind velocities.

Figure 19c shows the percentage relationship between the ESEA and EPEA values. Again, for two piles oriented 60° to the incoming flow with 1e gap considering 15 m/s, the result shows a significant value, indicating a high percentage ratio. Single stockpiles configurations and lower wind velocities show smaller values, suggesting that the relative effect is less pronounced under these conditions.

In general words, successive stockpiles configurations at 60° and 90° to the incoming flow under higher wind velocities (10 m/s and 15 m/s) tend to show the highest values of emission, in both absolute and relative values. Lower wind velocities (5 m/s and 6.5 m/s) and single stockpile configurations tend to have lower values, suggesting less particle re-emission under these conditions. It has been shown that as the wind velocity increases, the contribution of the surrounding areas of the piles increases more rapidly than the contribution of the piles themselves. It was also found that for stockpiles oriented 60º to the incoming flow, the emitted mass from the surrounding areas was higher than the mass emitted from the stockpiles while for stockpiles oriented 90º to the incoming flow the re-emission from the surrounding areas were the lowest one compared to the other investigated scenarios. This leads us to the conclusion that the intermediate case would be one where the piles are oriented 30° to the incoming flow. The heatmaps presented in **Figure 19** help identify conditions that lead to greater re-emissions potential, important information for open industrial yards management and wind erosion control strategies implementation.

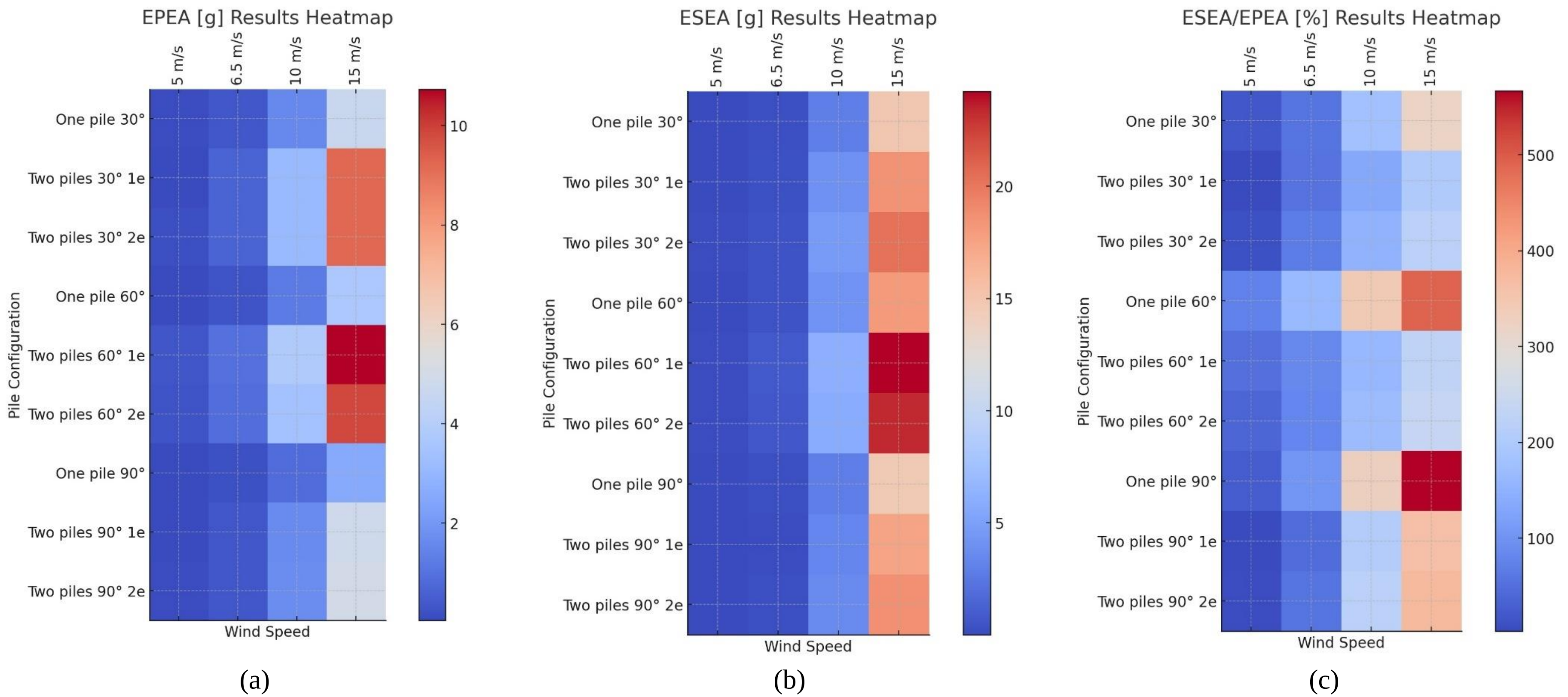

Figure 19. Heatmap presenting emission from pile erodible area (EPEA), emission from surrounding erodible area (ESEA), and the ration between EPEA and ESEA estimated from numerical results of Furieri (2012) and from US EPA emission model methodology for four wind gusts, three wind directions (30°, 60°, and 90°), and two gaps (1e and 2e)

6.2. Analysis of turbulent structures on a bed containing non-erodible particles

The paper performs a local analysis of turbulent structures development from wind flow over a granular bed containing non-erodible particle using the Large-Eddy Simulations technique to simulate the fluid flow and evaluates how these turbulent structures can influence particles emission. The coherent turbulent structures are associated with upward particles movement linked to emission. Most importantly, it identifies patterns of friction velocity distribution using Probability Density Functions obtained from the time series of friction velocity that could assist the development or improvement of emission models.

Coherent turbulent structures and friction velocity on a particles bed exposed to wind erosion containing non-erodible particles as rough elements

C. L. Morais [a], B. Furieri [a], M. C. S. Ferreira [b], J.-L. Harion [c], N. C. Reis Jr [a], J. M. Santos [a]

[a] *Federal Universisity of Espírito Santo, Departament of Environmental Engineering, 29075-910, Brazil*

[b] *Federal Institute of Education, Science and Technology of Espírito Santo, Mathematics Coordination, 29040-780, Brazil*

[c] *IMT Nord Europe, EI, F-59500, France*

Abstract: *This paper investigates key aspects of wind erosion, focusing on near wall turbulent structures, and the description of friction velocity distribution on particles bed containing non-erodible particles. It highlights the role of rough elements (non-erodible particles) in coherent turbulent structures development and the possible relationship with particle entrainment. It examines statistical distributions of wind friction velocity, providing insights into the variability of aerodynamic forces exerted on the surface. From the observation of the turbulent structures developed on the smooth and rough surfaces it was clear that the fluid flow is quite different in both cases. On the rough bed, it was possible to observe that the fluid remains in the ejection and sweep motions for most part of time, according to quadrant analysis. The analysis of the friction velocity probability density function for both smooth and rough beds indicates that the Gamma distribution provides a suitable model. For the smooth wall, the Gamma distribution with a mean of 2.46 and a mean of 0.06 shows good agreement, as validated by the NMSE criterion. Similarly, for the rough surface, the Gamma distribution with a mean of 2.6 and a mean of 0.05 also demonstrates a good fit according to the NMSE criterion. These findings underscore the ability of the Gamma distribution in accurately describing the friction velocity probability density function for varying surface conditions. Exposed that, the present work takes a step forward in the investigation of techniques to perform probabilistic description of the friction velocity for a bed containing non-erodible particles that could be used to improve emission models.*

Keywords: *Turbulent structures, wind erosion, non-erodible particles, dust emission, shear stress on rough surfaces*

1 Introduction

Fugitive dust emissions induced by the wind from stockpiles and beds (flat surfaces, as roads and regions surrounding stockpiles) in industrial plants can result in material loss and, at the same time, increase the concentrations of particles, being responsible for loss of visual range (Wu *et al.*, 2005; Huang *et al.*, 2009), soiling of surfaces (Tiwary and Colls, 2010) and significant risks to the human health (Novak et al., 2015; An et al., 2018; Hadley et al., 2018; Bové et al., 2019; Sigaux et al., 2019; Miller, 2020; Seaton et al., 2020) depending on the particles composition and size. For instance, small particles, less than 10 μm in diameter, may remain in the atmosphere for days before being washed out by rain or impacted out into some obstacle, as vegetation or buildings. Therefore, industries and environmental control agencies need to estimate these emissions for the development of dust control policies and for environmental licensing. The most used model to estimate emissions due to wind erosion from stockpiles was proposed by the United States Environmental Protection Agency (USEPA, 2006). Despite been developed based on experimental and field data, the model, however, has limitations. The model can underestimate emissions and has limited applicability to certain scenarios. For instance, only two shapes of stockpiles and three wind incidence angles are considered. In addition, the model does not consider the proportion of erodible and non-erodible particles in the mixture of granulated materials.

Many studies have used Computational Fluid Dynamics (CFD) to determine certain parameters used in the USEPA model to turn the model applicable to different scenarios regarding to the shape of the pile and the direction of the incident wind using RANS (Reynolds Averaged Navier-Stokes) approach for turbulence modeling (Badr and Harion, 2007; Toraño et al., 2007; Diego et al., 2009; Turpin and Harion, 2010; Furieri et al., 2012; Derakhshani et al., 2013; Liu et al., 2018; Ferreira et al., 2019b). Others, as Romeo et al. (2017), proposed changes in the USEPA methodology by recommending a new approach to how gusts, that usually cause erosion, should be considered in the model to improve accuracy.

Furieri (2012) proposed changes at the core of the USEPA emission model to include the effects of non-erodible particles, the larger ones, well-known in the literature for limiting the action of the wind by creating zones of low shear stress, not allowing the surrounding smaller particles to be emitted (Iversen et al., 1991; Neuman and Mckenna, 1995; López, 1998; Gillies et al., 2006; Turpin et al.,2010; Toure et al., 2011; Ferreira et al., 2013; Furieri et al., 2014; Smith et al., 2015; Swet and Katra, 2016; Mingari et al., 2017; Miri et al., 2017).

Caliman (2017) and Ferreira et al. (2019a) went further developing a new emission model for both particles beds and stockpiles using a simple equation based on the emitted volume and in the estimation of the eroded height considering the effects of the non-erodible particles. Their model is an advance of the model proposed by Descamps et al. (2005) for beds and could be applied in several stockpiles shapes and directions of the incident wind. The stockpile surface is divided into subareas with the same average shear stress and then the model is applied as if each subarea were a small inclined bed of particles.

In Descamps et al. (2005) study, the erosion ceases only when the surface is complete covered by non-erodible particles, an assumption not realistic because of the low shear stress zones created by non-erodible particles that is the gap solved in Ferreira et al. (2019a) model. However, Descamps et al. (2005) considered in their model the attractive effects between small particles due to the cohesion forces using a probability density function (PDF), and the effects of the turbulent bursts, coherent structures that can cause the emission of particles (Niño and Garcia, 1996; Séchet, 2000). These vortexes would appear with statistical spatial periodicities depending on the flow patterns and on the presence or not of particles. A deficiency of the model proposed by Descamps et al. (2005) comes from the hypothesis that the values of the mean spatial periodicities in the longitudinal and transversal directions of the flow obtained numerically by Jimenez and Moin (1991) for a smooth surface can be used for a surface composed of non-erodible particles (rough surface).

The complex association developed between the local turbulent air flow patterns and the presence of non-erodible roughness elements represents a challenge for wind erosion studies. Nevertheless, the turbulent structures development and particle entrainment is central to particle emission models. (Descamps et al., 2005; Ferreira et al., 2019b). This makes Large-Eddy Simulation (LES) an adequate approach to predict the turbulence flow structures and the shear stress (or friction velocity) distribution developed during the flow of the wind over rough surfaces in wind erosion events.

The shear stress distribution plays an important role, as it is responsible for the movement of particles. In traditional approaches, the shear stress has been analyzed using deterministic models. Deterministic models in fluid mechanics are those that attempt to predict the behavior of the fluid with absolute certainty, based on well-defined physical equations. For example, the Navier-Stokes equations represent a deterministic model that describe fluid motion accurately but gives only averaged terms to help predicting particles emission behavior and quantification (Badr and Harion, 2005; Turpin and Harion, 2009; Turpin et al., 2010; Furieri et al., 2012, 2013, 2014; Ferreira, et al., 2019b; Ferreira, et al., 2019a; Ferreira et al., 2020).

The stochastic nature of shear stress has led to a paradigm shift toward a more probabilistic perspective over the years, exploring the concept of PDFs to describe the innate variability and uncertainty in shear stress distribution (Savage and Jeffrey, 1951; Antonia, 1977; Dreeben and Pope, 1997; Keshavarzy and Ball, 1997; Miyagi et al., 2000; Cheng et al., 2003; Colella and Keith, 2003; Cheng, Tang and Zhu, 2004; Reeks, 2005; Cheng, 2006; Richefeu, et al., 2006; Sarmiento and Falcon, 2006; Dentoni et al., 2022; Zou et al., 2022). This probabilistic modeling also recognizes the complexity and variability inherent in natural processes related to shear stress such as particle emission, where parameter such as material heterogeneity, the characteristics and distribution of roughness elements, and environmental conditions can significantly impact the shear stress.

The aim of this study is to investigate the turbulence structures near a rough wall in which the rough elements would represent non-erodible particles in a bed or in a stockpile of granular material exposed to the atmospheric flow to evaluate how these turbulence structures could influence particles emission during a wind erosion event and identify patterns on the friction velocity distribution on the ground that could assist an emission model.

2 Numerical modeling of turbulent flow over rough and smooth surfaces

The physical model consists of an infinite bed formed by a mixture of erodible and non-erodible particles in a neutral atmosphere. Non-erodible particles are represented by random fixed cylindrical roughness elements and the erodible surface by the smooth region around them. The cover rate (CV) of non-erodible is taken as 20% (area occupied by the cylinders in relation to the total area of the rough bed). **Figure 1** shows the computational domain representative of the physical model, the roughness elements, and its dimensions in wall units.

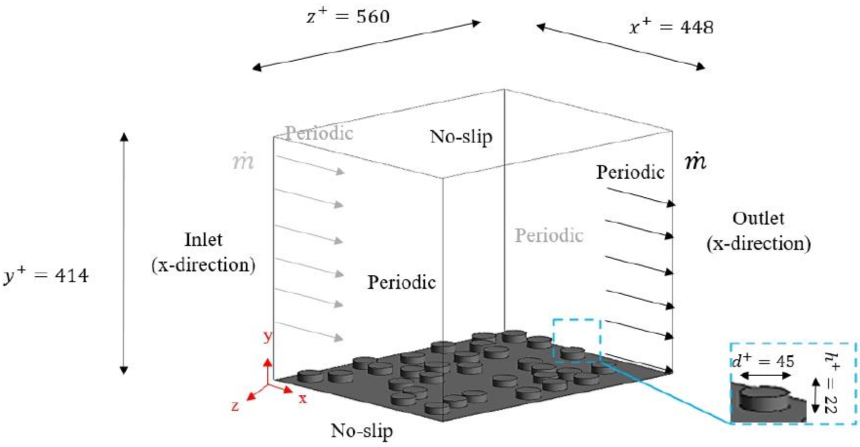

Figure 1. Schematic representation of the computational domain, its dimensions in wall units and the boundary conditions applied.

The turbulent and incompressible flow was modeled using the Large Eddy Simulation (LES) approach, thus, the governing equations used are the filtered equations of mass and momentum conservation (Equations 1 and 2, respectively).

$$\frac{\partial \bar{u}_i}{\partial x_i} = 0 \tag{1}$$

$$\frac{\partial \bar{u}_i}{\partial t} + \frac{\partial(\bar{u}_i \bar{u}_j)}{\partial x_j} = -\frac{1}{\rho}\frac{\partial \bar{p}}{\partial x_i} + \nu \frac{\partial}{\partial x_j}\left(\frac{\partial \bar{u}_i}{\partial x_j} + \frac{\partial \bar{u}_j}{\partial x_i}\right) - \frac{\partial \tau_{ij}}{\partial x_j} \tag{2}$$

where x_i represents the cartesian coordinates [m], $\bar{u}_i$ represents the resolved velocity components [m/s], t is time [s], ρ is the fluid density [kg/m³], $\bar{p}$ is the filtered pressure [Pa or N/m²], ν is the kinematic viscosity [m²/s], and τ_{ij} is the subgrid-scale (SGS) stress tensor ($\overline{u_i u_j} - \bar{u}_i \bar{u}_j$) [m²/s²]. The overbar indicates spatial filtering. The SGS stress tensor can be estimated by $\tau_{ij} = -2\mu_{SGS}(\bar{S}_{ij} - 1/3\delta_{ij}\,\tau_{kk})$, where μ_{SGS} is the SGS turbulent viscosity and $\bar{S} = \left(2\bar{S}_{ij}\bar{S}_{ij}\right)^{1/2}$. The turbulent viscosity μ_{SGS} was modeled as proposed by Smagorinsky-Lilly (Versteeg and Malalasekera, 2007) (Equation 3).

$$\mu_{SGS} = \rho (L_s)^2\, \bar{S} \qquad (3)$$

where $L_s = min(\kappa d, C_s\Delta)$ (L_s is the Smagorinsky length analogous to the Prandtl's mixing length associated with sub-grid scales), κ is the Von Kármán constant, d is the distance to the closest wall, C_s is the Smagorinsky constant, and Δ is the local grid scale ($\Delta = (\Delta x \Delta y \Delta z)^{1/3}$). C_s was assumed equal to 0.1, which is a value commonly used to simulate fluid flows over similar geometries (Xie et al., 2008).

The governing equations were discretized using the finite volume method implemented in the commercial software Ansys Fluent® 19.0 for the numerical solution. The SIMPLEC algorithm was employed for the pressure-velocity coupling. The spatial discretization of gradients was performed using the Green-Gauss Cell Based method, for pressure the second order, and for momentum central differencing scheme. The second-order method was used for the time derivative. Ansys Meshing® 19.0 software was used to construct a mesh of 4,188,797 elements whose details are shown **Figure 2**. **Figure 2a** shows the refinement on the top and bottom. **Figure 2b** shows the mesh of the roughness elements inside the domain.

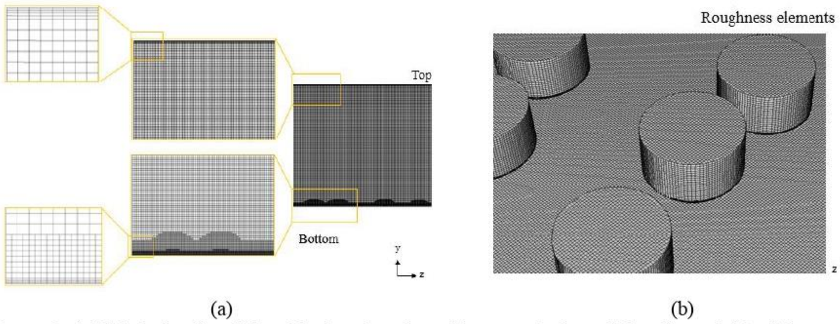

Figure 2. (a) Mesh details of the side showing the refinement in the solid walls and (b) of the roughness elements.

To reach LES model requirements, the minimum element size on the walls was about 10^{-4} m and the time step 2.5×10^{-5} s. The minimum size was obtained considering $y^+ = yu^*/\nu < 1$. Taking the Kolmogorov length scale (l_0) as an important parameter, which is 4.8×10^{-5} m in this case, the minimum filter size (Δ) was assumed as 8.5×10^{-5} m, thus, $\Delta > l_0$. In a domain with rough elements the appropriate time step can be estimated by $\Delta t = 0.002T_c$ (Xie et al., 2008) where $T_c = H_{elements}/u^*$. As the element height is 0.002 m and the estimated friction velocity is 0.12 m/s, the maximum value for Δt is 0.00004 s. Thus, Δt was chosen as 2.5×10^{-5} s.

For upstream and downstream (x-direction) boundaries, the periodicity condition and mass flow rate of 0.0051 kg/s was assumed. On the lateral sides (z-direction), the periodicity condition was also assumed, restraining mass conservation. For top and bottom boundaries and rough surface, non-slip conditions were assumed (**Figure 1b**). To obtain initial conditions for LES, Reynolds Averaged Navier-Stokes (RANS) simulations was performed using the $k-\omega$ Shear-Stress Transport (SST) model.

To evaluate the evolution of the flow from a smooth surface to the appearance of rough elements, the initial conditions are represented by a smooth surface. Also, the top of the domain keeps all the characteristics of a smooth bed with y^+ up to 30.

3 Model validation

For the model validation, typical turbulence statistics results obtained using LES were compared with experimental and Direct Numerical Simulation (DNS) data of Durst et al. (1987) and Kim et al. (1987), respectively. The validation of the mathematical model and the numerical solution for the turbulent incompressible flow was performed considering the smooth wall as reference since no experimental data was available for the rough wall investigated in the present work. **Figure 3** shows a schematic configuration of the set of points and planes chosen for analysis in the smooth top wall and ground wall with rough elements.

Durst et al. (1987) carried out investigations of probability density distribution of the streamwise velocity fluctuations in a turbulent wall boundary layer using hot-wire anemometry. Their measurements were performed in the following set of points: $y^+ = 2.788$, 5.015, 12.575, and 28.430 (shown in blue in **Figure 3a)**. Thus, in the numerical simulations, **Figure 3a** represents the top wall (smooth) and Figure 3b represents the bottom rough wall containing the non-erodible elements.

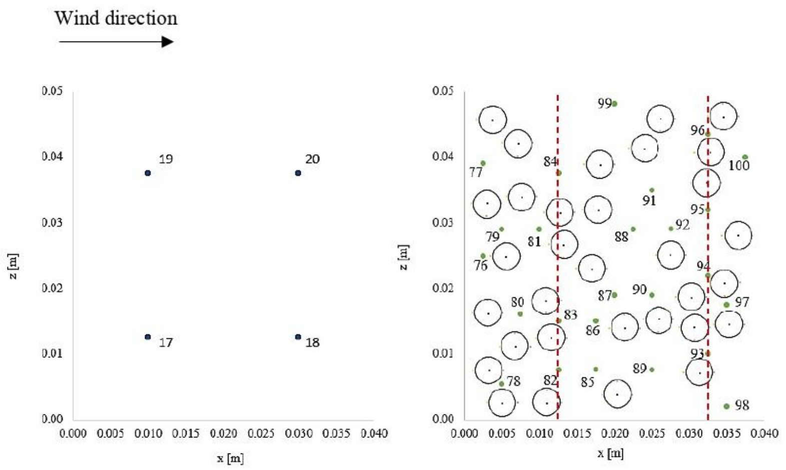

(a) (b)

Figure 3. Schematic configuration of the set of points of interest for analysis (a) smooth top wall and (b) ground wall with rough elements. In (a) all points (in blue) in the smooth wall are 0.034 m from the wall in y-axis (vertical) from top to bottom. In (b) all points (in green) in the rough wall are 0.001 m from the wall in y-axis (vertical) from bottom to top. Highlighted (in red) in (b) are the locations of the two planes where information was taken for the analysis carried out in the present work.

Figure 4 shows the instantaneous probability density distribution of streamwise velocity fluctuations normalized by the local rms-value of the velocity fluctuation for different dimensionless wall distance y^+. Qualitatively, the comparison between the results shows that the values measured by Durst et al. (1987) are in good agreement with the simulated values using LES in the present work.

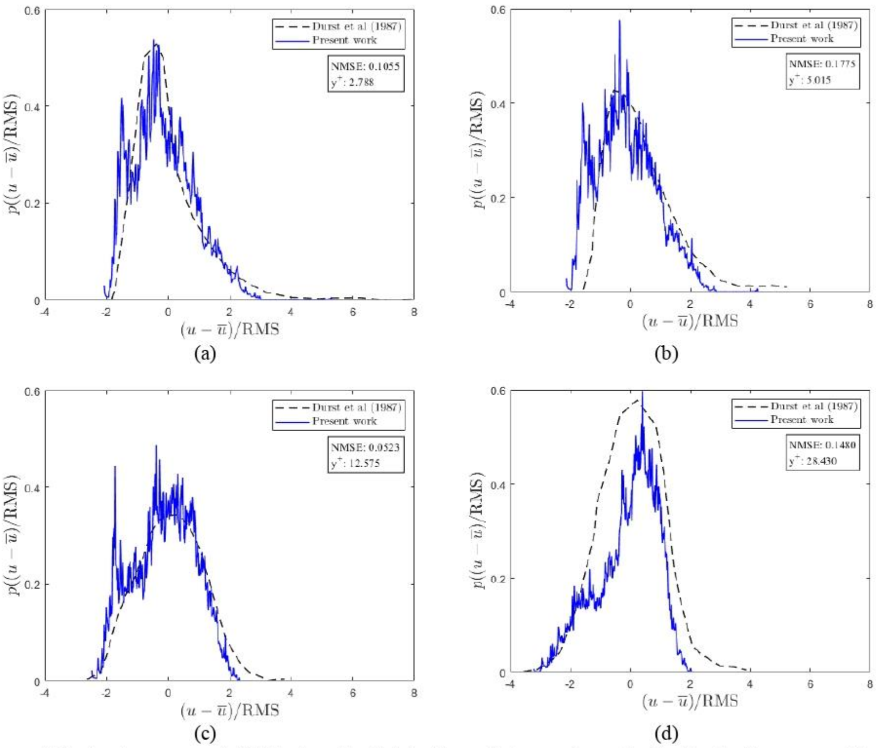

Figure 4. Instantaneous probability density distribution of streamwise velocity fluctuations normalized by the local rms-value of the velocity fluctuation taken at different y^+: (a) 2.788, (b) 5.015, (c) 12.575, and (d) 28.430.

In order to verify quantitatively if the data from Durst et al. (1987) and the data from the present work come from similar PDFs, the normalized mean square error (NMSE) was calculated between the two data sets (Equation 4).

$$NMSE = \frac{\|f_1 - f_2\|^2}{\|f_1\|^2} \tag{3}$$

where f_1 is the reference data, in this case the data from Durst et al. (1987) and f_2 is the data obtained in the present work. For the present validation, the NMSE was chosen as it is a straightforward and intuitive metric, providing a quantitative measure of similarity between two data distributions by calculating the normalized squared error between the two PDFs than the commonly used tests in the literature, such as Kolmogorov-Smirnov (KS) and Anderson-Darling (AD) (Mohd Razali and Bee Wah, 2011; Boyerinas, 2016; Arnastauskaitė, Ruzgas and Bražėnas, 2021).

For all y^+ tested, the value of NMSE varied from 0.0523 to 0.1775. These values are smaller than one, indicating that comparing the data using this metric, lead us to conclude that the simulated values are very close to the values obtained experimentally by Durst et al. (1987).

Additional validation was performed using the data obtained by Kim et al. (1987) who modeled a turbulent flow over a smooth open channel using the direct numerical simulation (DNS) technique. General characteristics of computed turbulence statistics agreed with experimental results. The comparison with results using LES revealed good agreement between the two data sets, as shown in **Figure 5**. The dimensionless profiles of velocity ($u^+ = u/u^*$, where u^* was assumed 0.16 m/s as the average value at the smooth wall) as a function of distance from the wall (y^+) obtained in the simulations, shown in **Figure 5a**, demonstrate good agreement with the data of Kim et al. (1987). The viscous layer extends approximately to $y^+ = 5$. In this layer, the effects of viscosity are considerably more important than the effects of turbulence. The profile presents a linear form, that is, $y^+ = u^+$. Between $y^+ = 5$ e $y^+ = 30$ one can observe a transition zone between linear and logarithmic profiles. From $y^+ > 30$ is expected that the profile assumes a logarithmic form, however, the present analysis is limited to $y^+ = 30$.

Comparison of the root mean square (RMS) profiles in the x, y and z directions shown in **Figure 5b.1**, **Figure 5b.2** and **Figure 5b.3**, indicates a good correspondence between LES and DNS data. Variations along the boundary layer are well reproduced, highlighting the ability of LES simulations to capture turbulent wind fluctuations. The value and vertical position of the maximum RMS of the longitudinal fluctuation are very close between the present study and the one from Kim et al. (1987). Proper identification of this peak is important because it indicates the region of maximum turbulence production.

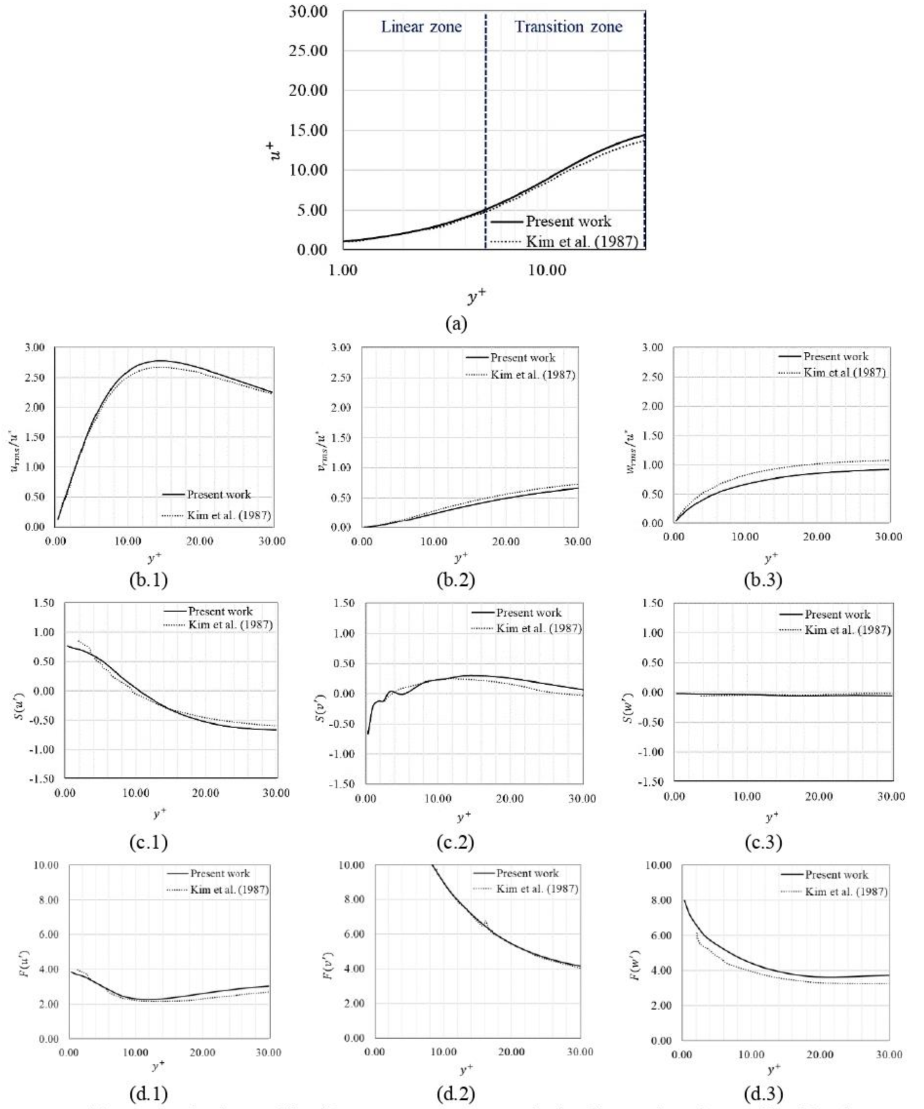

Figure 5. (a) Mean velocity profile, (b) root-mean-square velocity fluctuations (normalized by the mean friction velocity of 0.16 m/s), (c) skewness and (d) flatness in x, y, and z directions.

The results of the skewness (**Figure 5c.1**-**c.3**) and flatness (**Figure 5d.1**-**d.3**) profiles for the x, y, and z directions also show good fitting, reflecting the ability of the simulations to reproduce not only the central moments, but also the asymmetry and shape of the turbulence distribution.

Exposed that, by comparing the data simulated in the present work with the data from Durst et al. (1987) and Kim et al. (1987), we can conclude that good agreement was obtained for both turbulent statistics and probability density functions on the smooth wall. This allows us to continue further analysis.

4 Near wall turbulent structures in a bed with rough elements

One widely used tool in turbulent flow analysis is the Omega criterion (Ω- criterion), which helps identify and visualize turbulent structures based on the vorticity dynamics within the flow field. The Omega criterion examines the behavior of vorticity and its alignment with the principal strain rate tensor to locate regions of intense vortical activity, which often correspond to coherent turbulent structures. **Figure 6** shows the distribution of three-dimensional vortices obtained by the Ω-criterion (Liu *et al.*, 2016; Zhang *et al.*, 2019):

$$\Omega = \frac{||B||^2}{||A||^2 + ||B||^2 + \varepsilon} \tag{4}$$

where A is the shear strain rate, B the vorticity and ε is a constant to avoid zero values. The Ω-criterion allows the visualization in the range of Ω of 0.51–0.6, what is quite convenient since an alternative would be using the Q-criterion, which require several attempts because the vorticity regions may be more diffuse and dispersed compared to the Ω-criterion. The Q-criterion is based on the evaluation of the Cauchy deformation matrix, which is a measure of the deformation rate of the fluid in the flow field. It identifies regions where the stretching tendency is greater than the compression tendency, which is characteristic of regions of positive vorticity. The Ω-criterion, on the other hand, is based on the relationship between the principal strain rate and the principal vorticity of the flow field, as mentioned before. It identifies regions where vorticity is aligned with strain rate, which is characteristic of regions of intense vortical activity. The range between 0.51 and 0.6 in the Ω-criterion may be specifically significant for identifying coherent structures where the relationships between vorticity and deformation are particularly pronounced. In the present work the value for Ω of 0.6 was used to identify the structures proving to be an appropriate value.

Three-dimensional iso-surfaces were built on top and ground boundaries of the domain to allow the identification of regions where the magnitude of rotation is greater than the magnitude of deformation ($\Omega > 0$). The identified vortices in **Figure 6** are classified by the longitudinal component of the vorticity, ω_x. Positive vorticity values ($\omega_x > 0$) are colored red and negative values ($\omega_x < 0$) are colored blue. The colors show the direction of rotation.

It can be observed that many vortices have an elongated structure close to the top of the domain in **Figure 6a**. These vortices are almost longitudinal structures in the smooth wall. Similar elongated structures can also be seen in free paths between the rugosities where such structures can freely rotate without a breaking impact with cylinders (**Figure 6b**). The highlighted region in **Figure 6c**, aims to present the three-dimensional visualization of vortices which collide with the cylinders, exposing a characteristic of turbulent flow around obstacles: the breakdown of larger coherent structures into smaller ones that rotate in completely different directions, which may or may not meet again and flow in the same direction and same rotation. But the most important fact about visualizing these structures is that, despite being an instantaneous picture, these figures show the development, interrelations, breaks and regrouping of these structures that happens at all times in the domain in different directions.

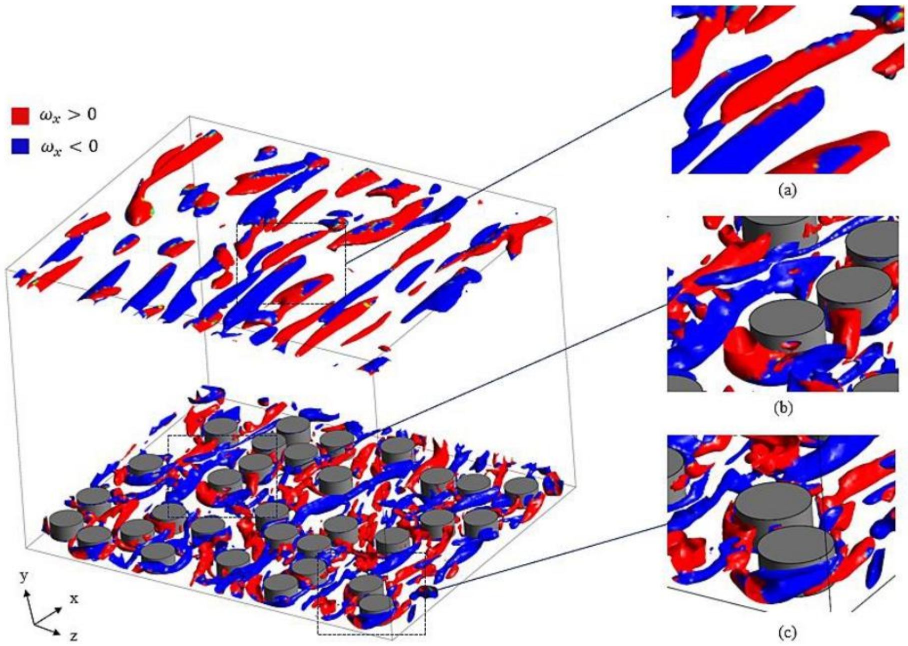

Figure 6. Distribution of three-dimensional vortices obtained by the Ω criterion. Highlighted is (a) elongated structures on the smooth top of the domain without the influence of roughness, (b) elongated structures in free paths and (c) smaller structures around obstacles at the base of the domain.

Figure 7 shows the dimensionless time evolution of turbulent structures in the rough bed in terms of the dimensionless time $t^+ = tu^{*2}/\nu$, where t is the time, u^* is the friction velocity in the smooth wall (0.16 m/s), and ν is the air kinematic viscosity (0.00002 m²/s). It is possible to see that, as the time goes by (**Figure 7a-d**), different configurations and rotation directions are observed between the cylinders. The evolution of turbulent structures between roughness, as already know, is a dynamic phenomenon that unfolds over time, being influenced by a complex interaction between the moving fluid and the rough characteristics that generates turbulent patterns that are not static, but rather subject to continuous change. This allows us to observe how turbulence characteristics develop and interact with roughness over time.

In **Figure 7a**, it is possible to observe an elongated structure with predominant negative rotation in the highlighted yellow region. After $t^+ = 4$ (**Figure 7b**) it is already possible to notice the displacement of this elongated structure and the appearance of smaller structures with negative rotation. After $t^+ = 4$ (**Figure 7c**), only a part of the elongated structure first observed remains. Finally (**Figure 7d**), the observed structure is no longer in the highlighted region, which is now occupied by fragments of structures with positive and negative rotation.

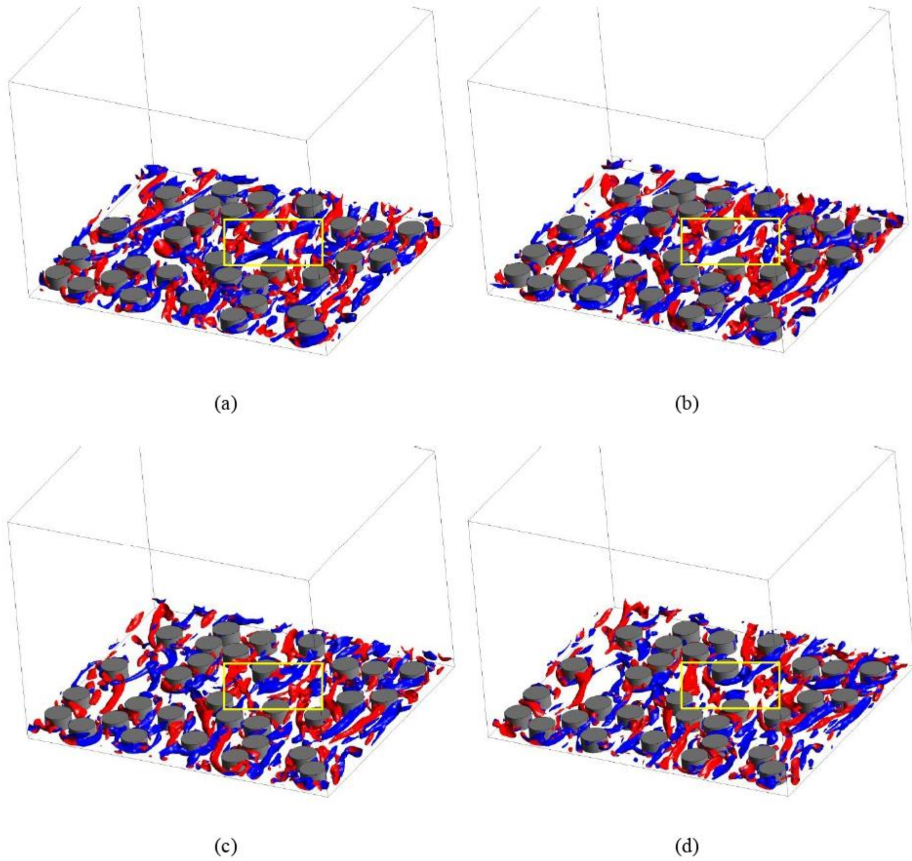

Figure 7. Time evolution of turbulent structures in the rough bed. (a) $t^+ = 57998$, (b) $t^+ = 58002$, (c) $t^+ = 58006$, and (d) $t^+ = 58010$.

5 The influence of near wall turbulence structures on particles transportation from a bed containing non-erodible particle (rough elements)

Particles in a turbulent flow experience several forces and interactions. These forces include drag, lift, and turbulent diffusion, which can influence the trajectory of particles. In near-wall regions, the presence of turbulent structures plays an important role increasing particle emission.

Particles emission generally occurs in the inner region of the turbulent boundary layer which are divided into the viscous sublayer, transition (or buffer) layer and the logarithmic layer (You and Wan, 2017). According to Ziskind et a. (1995), fine particles are generally immersed in the viscous sublayers. In this sublayer, an interesting phenomenon has its origin, and it has been claimed as the most important mechanism responsible for turbulence production. There is a consensus that turbulence is mainly produced close to the walls due to a repetitive cycle of intermittent events called turbulent bursts (Davidson, 2015; You and Wan, 2017).

The viscous sublayer is continually disturbed by turbulent inrushes and bursts going deep in the near wall region where they become very unstable. You and Wan (2017) described the development of bursts with the exactly following words: “a decelerated region is formed due to the wall skin friction and is then subject to the effect of an upstream large-scale disturbance of a high axial velocity. At the transition from the overflowing disturbance to the decelerated region, a strong shear layer is developed and induces an abrupt ejection (burst) of fluid from the decelerated region towards the turbulent core. Chaotic motions are caused by the violent interactions at the shear layer between the ejecting fluids and the faster overflowing fluids. Some chaotic motions induce the wall ward flow (inrush) that could reach all the way up to the wall”. Therefore, when fluid is ejected from the wall there is a high probability of particles being carried out from the viscous sublayer to the outer region.

Figure 8 shows vorticity distribution in plane *y-z* at x = 0.0125 m and friction velocity distribution on the ground. The vorticity distribution varies between 500 s^{-1} and -500 s^{-1}. It is possible to notice that the maximum absolute values are more recurrent near the ground and also near the top wall, showing that in these regions the turbulence in the form of rotational structures is more intense. In the lower part of the domain, the occurrence of these rotational structures is more intense than in the upper part. Probably, the impact of the fluid with the cylindrical roughness leads to their rupture, increasing the quantity observed in relation to the smooth upper wall in addition to the change in the direction of rotation and intensity of the vorticity. The further we move our observation away from the walls of the domain, we observe that the intensity of rotation decreases, it is not in the entire domain that it is possible to observe the occurrence of rotational coherent structures, it may indicate that they are not dissipated but follow an organized vorticity pattern.

In **Figure 8a**, we see next to the marked point, a region where the fluid rotates at 500 s^{-1} and a small region where the fluid rotates at -500 s^{-1}. This shows that between these two regions, there is an intermediate region where the fluid is forced to move upward in relation to the ground wall. Associating this behavior with a friction velocity between 0.15 and 0.30 m/s, we can point to a possible emission region, where a particle positioned there could have its threshold friction velocity reached and once moved, the flow would eject that particle to the atmosphere. In **Figure 8b** and **Figure 8c** it is possible to observe similar behavior. We can observe that between two regions where the fluid rotates in opposite directions, an upward movement of the fluid is observed. The difference between the regions close to points a, b and c would be the intensity and size of the regions where the fluids rotate, which are strongly influenced by the cylindrical roughness and their arrangement in the bed.

Figure 9 shows the same as Figure 8 but in plane *y-z* at x = 0.0325 m. We can see in the highlighted points, vorticity patterns influenced mainly by the shape and arrangement of the roughness, showing in some regions the upward movement of the fluid.

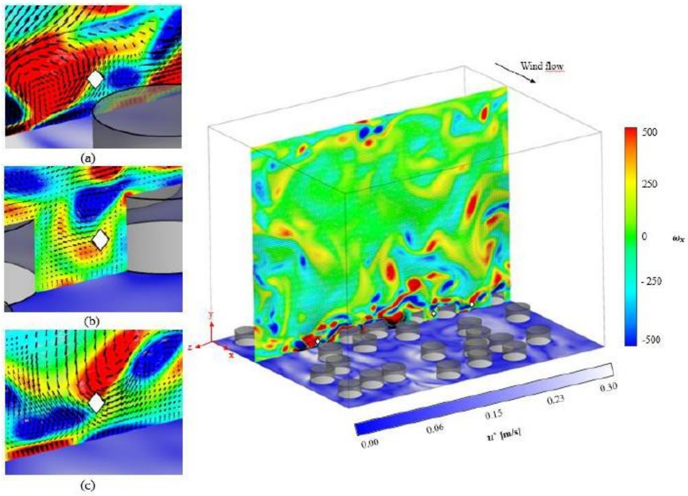

Figure 8. Vorticity distribution at plane x = 0.0125 m and friction velocity distribution on the ground. (a), (b) and (c) are highlights of points 82, 83, and 84, respectively. For point number locations report to Figure 3b.

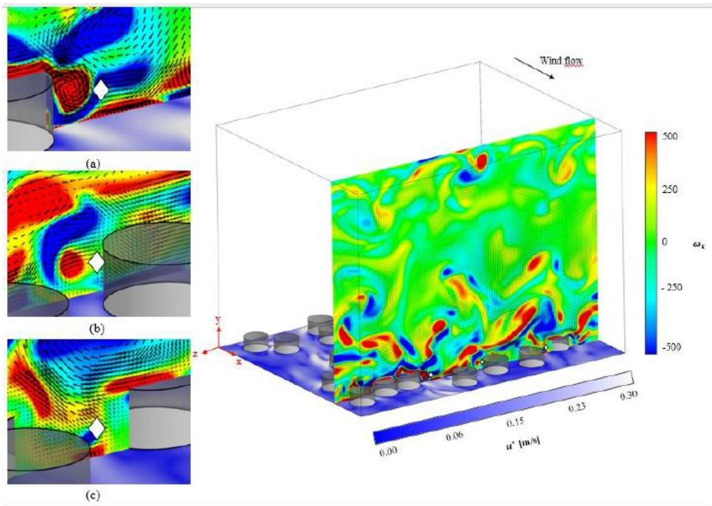

Figure 9. Vorticity distribution at plane x = 0.0325 m and friction velocity distribution on the ground. (a), (b) and (c) are highlights of points 94, 95, and 96, respectively. For point number locations report to Figure 3b.

Exposed that, it is also worth performing the quadrants analysis of turbulent fluctuations at the same above-mentioned points to complement quantitatively the analysis of the relationship between turbulent structures and particle emission.

Turbulent fluctuation quadrant analysis is a widely used technique employed in the investigation of turbulent flows. This method involves partitioning the flow field into quadrants based on the components of velocity fluctuations, enabling an examination of turbulence dynamics. By discerning the occurrences of outward interactions (Quadrant I, $u' > 0$ and $v' > 0$), ejections (Quadrant II, $u' > 0$ and $v' < 0$), inward interactions (Quadrant III, $u' < 0$ and $v' < 0$), and sweeps (Quadrant IV, $u' < 0$ and $v' < 0$) within each quadrant, insights into the relationship between turbulent eddies and structures can be discussed (Franca *et al.*, no date; Giostra, Cava and Schipa, 2002; Yu, Vinkovic and Buffat, 2016; Shih *et al.*, 2017; Jia *et al.*, 2022; Mangan *et al.*, 2022; Wang *et al.*, 2022).

The results obtained with LES are shown in **Figure 10**. **Figure 10a-c** refers to fluctuations observed in points 82, 83, and 84 placed in the bottom rough wall of the domain at x = 0.0125m. **Figure 10d-e** refers to fluctuations observed in points 92, 94, and 96 placed in the bottom rough wall of the domain at x = 0.0325. Quadrants II and IV are associated with ejection and sweep events result, respectively. The proportion in time that each fluctuation remained in the four quadrants are presented in **Figure 10**.

As **Figure 10** shows, the quadrant analysis allows the formation of an ellipse with a predominant area between Quadrants II and IV, since upward vertical movements (ejection) are always associated with downward vertical movements (sweep). Due to the conservation of mass and movement, if fluid moves in one direction, fluids in the opposite direction must occupy the space left by the fluid that ascended. During this process, secondary movements, with less influence, are generated, occupying the part of the area referring to Quadrants I and III.

At all points observed, the percentage of fluctuations in Quadrant II is always greater than in the other Quadrants. Associated with this, the second highest percentage of fluctuations is found in Quadrant IV, highlighting the relationship between Quadrants II and IV, as expected. When dealing with the emission of particles, these points, for instance, could be associated with the emission of particles driven not only by the common movements of entrainment by wind and saltation, but also by the turbulent structures that are in constant movement of ejection and sweep.

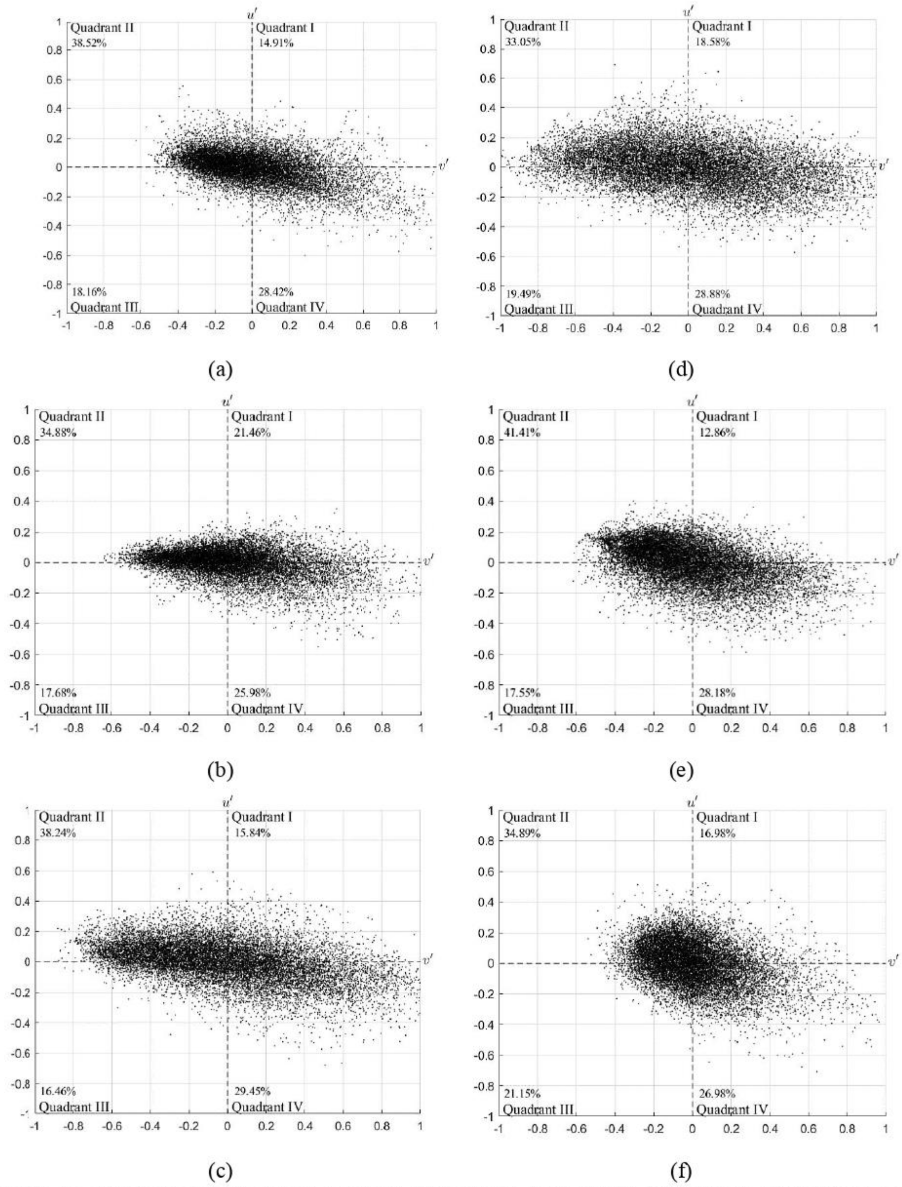

Figure 10. Quadrant analysis for (a) point 82, (b) point 83, (c) point 84, (d) point 93, (e) point 94, and (f) point 96.

6 Near wall shear stress distribution based on probability density functions

In the present section, we delve into the results obtained through numerical simulations, focusing on the probability density function (PDF) of friction velocity description obtained for smooth and rough walls.

6.1. Smooth wall

Figure 11 presents the probability density function of friction velocities obtained by the numerical simulations in four points located in the upper smooth wall and identified as 17, 18, 19, and 20. **Figure 11** shows a prominent peak around 0.1 m/s. No significant outliers were identified that could deform the general understanding of the distributions.

For further analysis, we calculated descriptive measures including mean, standard deviation, skewness, and flatness. These metrics provided additional insights into data centrality and sparsity. These values reflect the friction velocities reached on the upper smooth wall of the domain over time. The mean friction velocity varies from 0.13 to 0.15 m/s. The standard deviation is equal to 0.09 m/s for all points, as an approximation.

If the skewness is 0, the data has a symmetric distribution. If the skewness is positive, the data is biased to the right of the mean. If the skewness is negative, the data is biased to the left of the mean. The calculated skewness varied from 1.01 to 1.23, suggesting a tendency to the right of the mean, as shown **Figure 11** in for all points.

Flatness (or kurtosis) less than 3 indicates a distribution that is less concentrated (flatter) than a normal distribution. Flatness greater than 3 indicates a more concentrated distribution (peak) than a normal distribution. The calculated flatness varies from 4.05 to 4.91, indicating a more concentrated distribution, presenting a peak, as shown **Figure 11** in for all points.

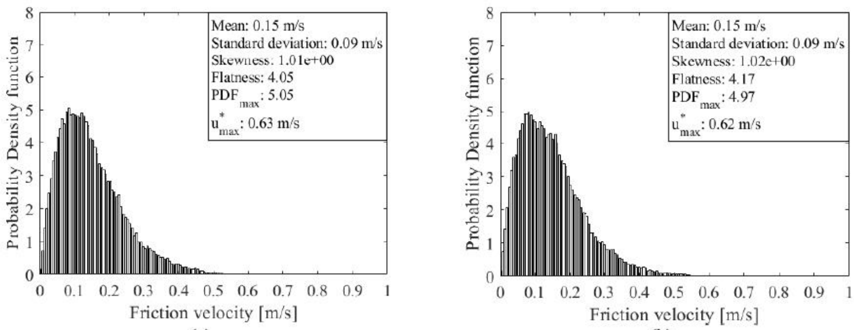

(a) (b)

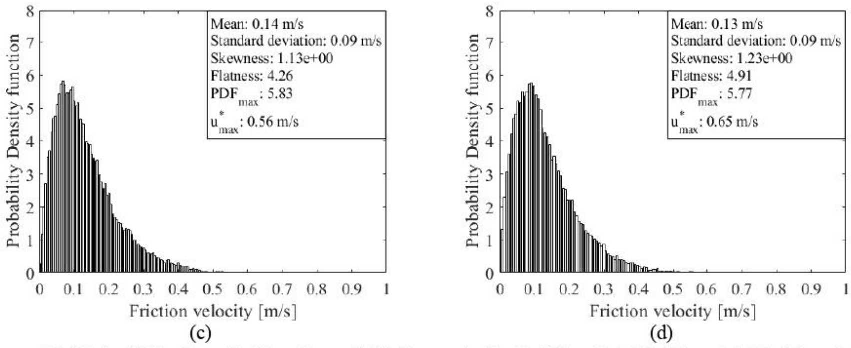

Figure 11. Probability Density Function of friction velocity in (a) point 17, (b) point 18, (c) point 19, and (d) point 20.

So, we can state that the mean friction velocity, standard deviation, skewness, and flatness, at the four points, exhibit very similar behavior, providing a clearer view of the proximity of the data found for different points distributed in a smooth wall.

To improve the analysis of probability density functions, well-known continuous distributions (Beta, Burr, Gamma, Lognormal, Normal and Weibull) were compared with probability density function obtained from LES. **Table 1** presents the mathematical descriptions and the parameters for each tested distribution.

Table 1. Mathematical description of tested probability density functions.

PDF	Mathematical description	Parameter	Parameter description	Support
Beta	$f(x\|a,b) = \frac{1}{B(a,b)} x^{a-1}(1-x)^{b-1} I_{[0,1]}(x)$ where $B(.)$ is the Beta function.	a	First shape parameter	$a > 0$
		b	Second shape parameter	$b > 0$
Burr	$f(x\|\alpha,c,k) = \frac{\frac{kc}{\alpha}\frac{x}{\alpha}^{c-1}}{(1+(\frac{x}{\alpha})^c)^{k+1}}$	α	Scale parameter	$\alpha > 0$
		c	First shape parameter	$c > 0$

		k	Second shape parameter	$k > 0$
Gamma	$f(x\|a,b) = \frac{1}{b^a \Gamma(\mathrm{a})} x^{a-1} e^{\frac{-x}{b}}$ where $\Gamma(.)$ is the gamma function.	a	Shape parameter	$a > 0$
		b	Scale parameter	$b > 0$
Log normal	$f(x\|\mu,\sigma) = \frac{1}{x\sigma\sqrt{2\pi}} \exp\left\{\frac{-(\log x - \mu)^2}{2\sigma^2}\right\}$	μ	Mean of logarithmic values	$-\infty < \mu < \infty$
		σ	Standard deviation of logarithmic values	$\sigma \geq 0$
Normal	$f(x\|\mu,\sigma) = \frac{1}{\sigma\sqrt{2\pi}} e^{\frac{-(x-\mu)^2}{2\sigma^2}}$	μ	Mean	$-\infty < \mu < \infty$
		σ	Standard deviation	$\sigma \geq 0$
Weibull	$f(x\|a,b) = \begin{cases} \frac{b}{a}\left(\frac{x}{a}\right)^{b-1} e^{-(x/a)^b} & if\ x \geq 0 \\ 0\ if\ x < 0 & \end{cases}$	a	Scale parameter	$a > 0$
		b	Shape parameter	$b > 0$

Figure 12 shows the adjustment of the probability density functions obtained using the LES approach to above-mentioned continuous distribution. In addition, the normalized mean square error (NMSE) between LES results and the distributions were calculated. Qualitatively, it is possible to observe that better fit is provided by Gamma distribution.

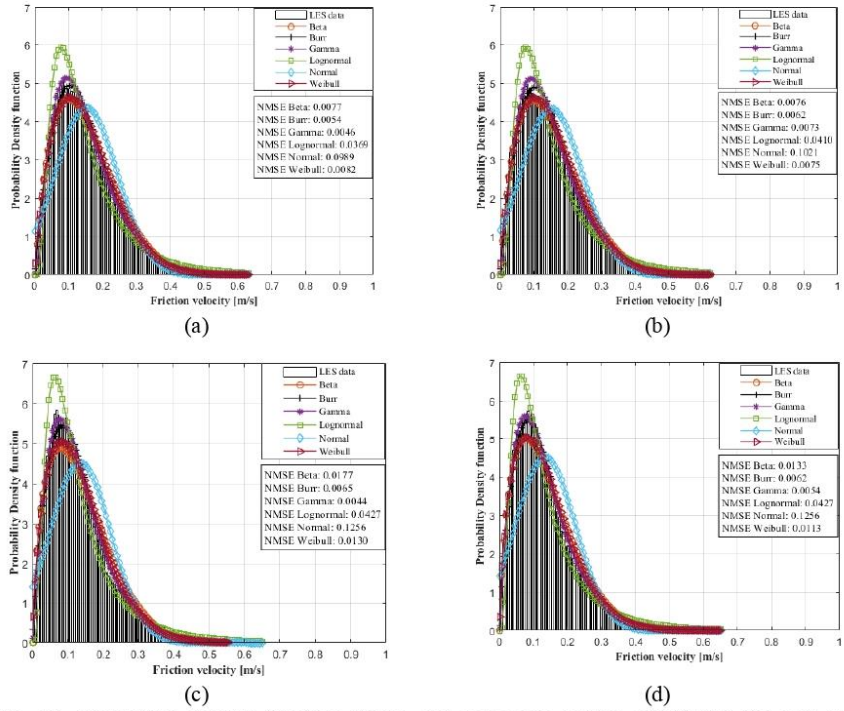

Figure 12. Probability density function fitting and respective values of NMSE for each tested distribution for the point located at $y = 0.03434$ m and coordinates x and z equal to (a) (0.0100, 0.0125) (point 17), (b) (0.0300, 0.0125) (point 18), (c) (0.0100, 0.0375) (point 19), and (d) (0.0300, 0.0375) (point 20).

Table 2 summarizes the calculated NMSE highlighting Gamma distributions as the one with the lowest error in relation to the LES results.

Table 2. NMSE for the four points in the smooth wall for all distribution tested.

Point	Beta	Burr	Gamma	Lognormal	Normal	Weibull
17	0.0077	0.0054	**0.0046**	0.0369	0.0989	0.0082
18	0.0076	0.0062	**0.0073**	0.0410	0.1021	0.0075
19	0.0177	0.0065	**0.0044**	0.0347	0.1330	0.0130
20	0.0133	0.0062	**0.0054**	0.0427	0.1256	0.0113

Table 3 shows the parameters of all tested distributions fitted with LES results. From this result, we can assume that friction velocity probability density function in a smooth wall, for any point, can be described by Gamma distribution with mean a of 2.46 and mean b of 0.06.

Table 3. Parameters for all tested distributions for points 17, 18, 19, and 20 in the smooth wall.

Distribution	Parameters	Point 17	Point 18	Point 19	Point 20
Beta	a	1.93	1.88	1.66	1.76
	b	6.06	5.82	5.12	6.65
Burr	α	0.41	0.45	0.34	0.31
	c	1.92	1.88	1.81	1.83
	k	6.09	6.89	5.02	4.52
Gamma	$\boldsymbol{a}$	**2.64**	**2.57**	**2.33**	**2.31**
	$\boldsymbol{b}$	**0.06**	**0.06**	**0.06**	**0.06**
Lognormal	μ	-2.08	-2.09	-2.23	-2.23
	σ	0.68	0.69	0.73	0.73
Normal	μ	0.15	0.15	0.14	0.14
	σ	0.09	0.09	0.09	0.09
Weibull	a	0.17	0.17	0.15	0.15
	b	1.74	1.72	1.61	1.60

6.2. Rough wall

Figure 13a-c presents the PDF of friction velocity in points 82, 83, and 84 (at $x = 0.0125$ m) on the rough wall (see points locations in Figure 3). **Figure 13d-f** shows the PDF of friction velocity in points 92, 93, and 96 (at $x = 0.0325$ m) on the rough wall. The peaks in **Figure 13** suggest that most friction velocities achieved are within this range of one order of magnitude. The PDFs exhibit asymmetry to the right, indicating that, although unlikely, high values of friction velocity may occur. No significant outliers were identified.

For further analysis, we calculated descriptive measures including mean, standard deviation, skewness, and flatness. We can state that all metrics are quite different for all points evaluated. The flow in the rough bed is quite complex. The flow is influenced by the diameter and height of the cylinders, the distribution of the cylinders and the proportion of the bed that they occupy (cover rate), which is 20% in this work.

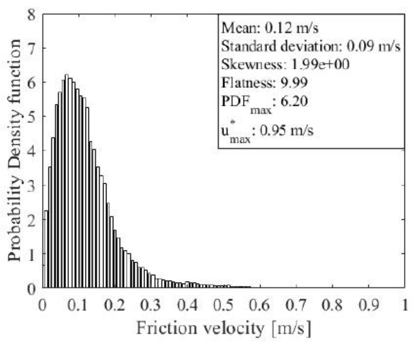

(a)

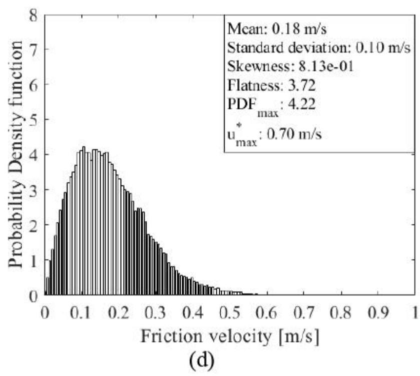

(d)

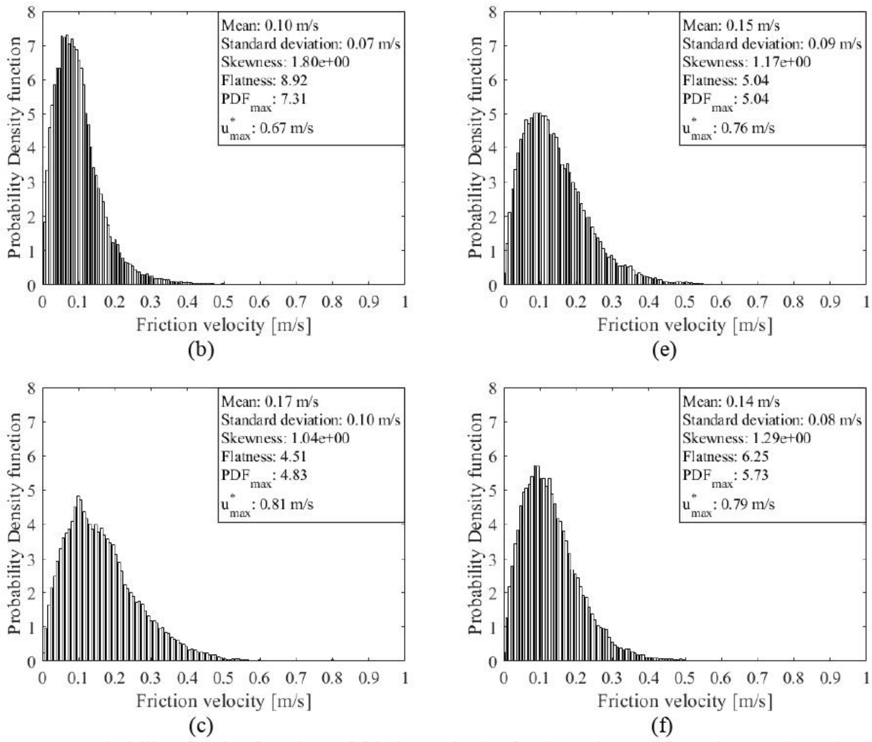

Figure 13. Probability density function of friction velocity for (a) point 82, (b) point 83, (c) point 84, (d) point 93, (e) point 94, and (f) point 96.

Therefore, looking at the results point by point, we see how complex it is to use these results in an emission model, for example. Because, for each point, we have a different PDF for friction velocity description. For this reason, we also calculated the NMSE for each evaluated point to observe how close the PDF obtained from the simulation of wind flow over the roughness is to known distributions.

Figure 14a-c shows the fit for points 82, 83, and 84 at $x = 0.0125$ of the probability density functions from LES to known continuous distributions: Beta, Burr, Gamma, Lognormal, Normal and Weibull. In addition, the NMSE between LES results and the above-mentioned distributions was calculated. The same was performed for points 93, 94, and 96 at $x = 0.0325$ in **Figure 14d-f.**

Qualitatively evaluating **Figure 14a-c**, it is possible to observe that the better fit is provided by the Gamma distribution for points 82, 83, and 84.

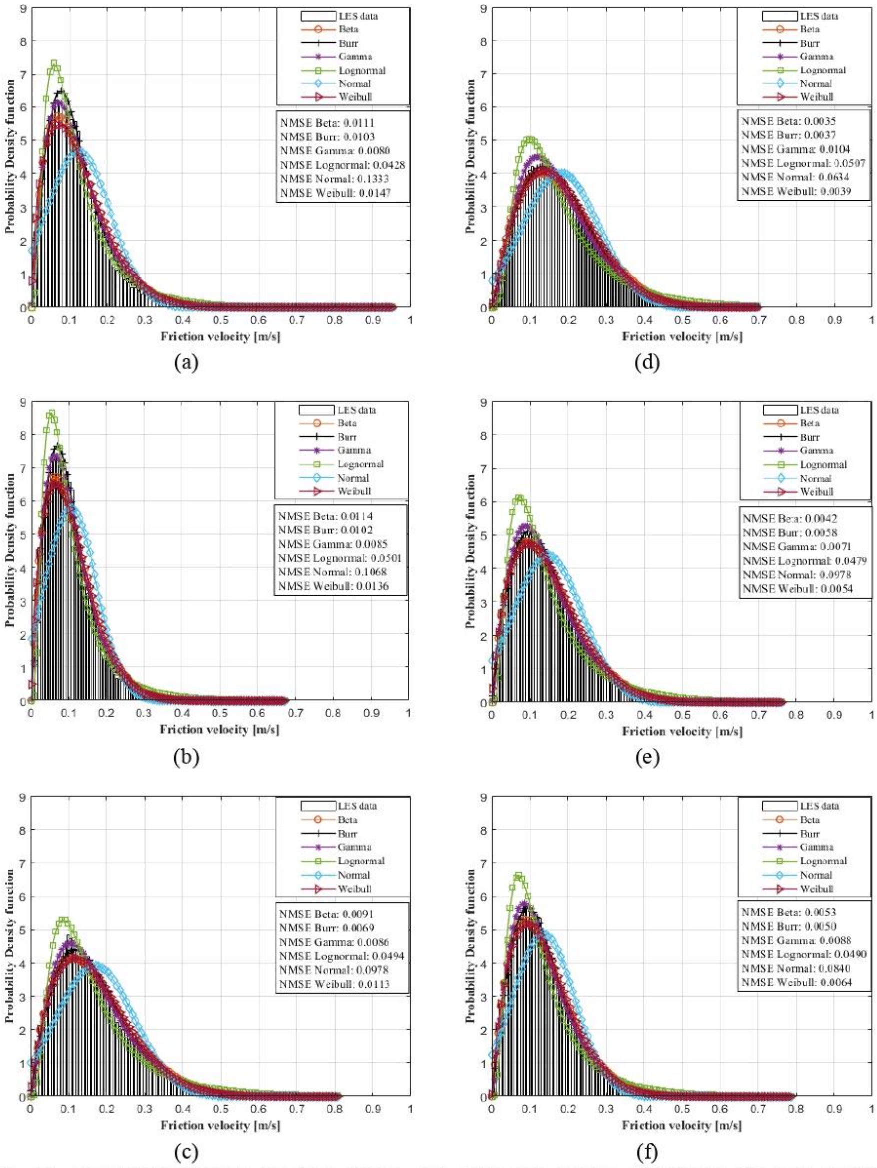

Figure 14. Probability density function fitting and respective values of NMSE for each tested distribution at $y = 0.001$ m and $x = 0.0125$ at z equal to (a) 0.0075 (point 82), (b) 0.0150 (point 83), (c) 0.0375 (point 84). Probability density function fitting and respective values of NMSE for each tested distribution at $y = 0.001$ m and $x = 0.0325$ at z equal to (d) 0.0100 (point 93), (e) 0.0220 (point 94), and (f) 0.0435 (point 96).

Table 4 summarizes the calculated NMSE, highlighting Gamma distribution as the one with the lowest error in relation to the LES results for points 82, 83, and 84.

Table 4. NMSE for the three points at x = 0.0125 m in the rough wall for points 82, 83, and 84 at x = 0.0125 m for all distribution tested.

Point	Beta	Burr	Gamma	Lognormal	Normal	Weibull
82	0.0111	0.0103	**0.0080**	0.0428	0.1333	0.0147
83	0.0114	0.0102	**0.0085**	0.0501	0.1068	0.0136
84	0.0091	0.0069	**0.0086**	0.0494	0.0978	0.0113

Figure 14a-c shows the adjustment for points 92, 93, and 96 of the probability density functions to known continuous distributions: Beta, Burr, Gamma, Lognormal, Normal and Weibull. In addition, the NMSE between LES results and the above-mentioned distributions was calculated. Qualitatively evaluating **Figure 14a-c**, it is possible to observe that the better fit is provided by Beta, Burr, Gamma, and Weibull distributions for points 93, 94, and 96. **Table 5** summarizes the calculated NMSE, highlighting Beta, Burr, Gamma, and Weibull distributions as the ones with the lowest error in relation to the LES results for points 93, 94, and 96.

Table 5. NMSE for the three points at x = 0.0325 m in the rough wall for all distribution tested.

Point	Beta	Burr	Gamma	Lognormal	Normal	Weibull
93	**0.0057**	**0.0058**	**0.0148**	0.0865	0.1006	**0.0058**
94	**0.0071**	**0.0064**	**0.0073**	0.0603	0.1368	**0.0085**
96	**0.0073**	**0.0053**	**0.0078**	0.0596	0.1126	**0.0087**

Erro! Autoreferência de indicador não válida. shows the parameters of the distributions for points 82, 83, 84, 93, 94, and 96. Evaluating the parameters of all adjustments for all points for distributions tested, we were able to find a distribution that meets the low NMSE criterion and that meets the criterion of similar parameters as Gamma distribution, highlighted in blue. From that, the probability density function for a rough surface can be described by Gamma distribution with mean a of 2.6 and mean b of 0.05.

Table 6. Parameters for all tested distributions for points 82, 83, and 84 at x = 0.0125 m, points 93, 94, and 95 at x = 0.0325 m and between the average on the 25 points in the rough bed.

Distribution	**Parameters**	**Point 82**	**Point 83**	**Point 84**	**Point 93**	**Point 94**	**Point 96**
Beta	a	1.91	1.99	1.98	2.11	1.95	2.11
	b	12.77	10.68	7.46	6.09	8.16	10.08
Burr	α	0.18	0.16	0.50	0.70	0.37	0.30
	c	2.04	2.08	1.90	1.99	1.89	2.00
	k	2.41	2.67	7.07	12.53	5.40	4.68

Gamma	***a***	**2.33**	**2.50**	**2.61**	**2.97**	**2.51**	**2.66**
	b	**0.05**	**0.04**	**0.06**	**0.06**	**0.06**	**0.05**
Lognormal	μ	-2.32	-2.47	-1.98	-1.89	-2.13	-2.20
	σ	0.72	0.69	0.69	0.65	0.70	0.68
Normal	μ	0.12	0.10	0.17	0.18	0.15	0.14
	σ	0.09	0.07	0.10	0.10	0.09	0.08
Weibull	a	0.14	0.12	0.19	0.20	0.16	0.15
	b	1.55	1.62	1.74	1.88	1.69	1.74

7. Conclusion

The aim of the present work was to investigate the turbulence structures near a rough wall in which the rough elements would represent non-erodible particles in a bed or in a stockpile of granular material exposed to the atmospheric flow. The turbulent structures are responsible for the emission of erodible particles during wind erosion. Therefore, the understanding of patterns in the turbulence structures could help elucidating further work on emission modeling.

From the observation of the turbulent structures developed on the smooth and rough surfaces it was clear that the flow structures are quite different in both cases. On the rough bed, it was possible to observe that the fluid remains in the ejection and sweep motion for most part of time, according to quadrant analysis. That means that approaches that consider results from smooth walls, as Descamps et al. (2005) work, as spatial and temporal frequency of turbulent structures can carry information far from reality.

The analysis of the friction velocity probability density function for both smooth and rough beds indicates that the Gamma distribution provides a suitable model. For the smooth wall, the Gamma distribution with a mean of 2.46 and a mean of 0.06 shows good agreement, as validated by the NMSE criterion. Similarly, for the rough surface, the Gamma distribution with a mean of 2.6 and a mean of 0.05 also demonstrates a good fit according to the NMSE criterion. These findings underscore the ability of the Gamma distribution in accurately describing the friction velocity probability density function for varying surface conditions.

Exposed that, the present work takes a step forward in the investigation of techniques to perform probabilistic description of the friction velocity for a bed containing non-erodible particles that could be used to improve emission models. The particle emission model proposed by Klose and Shao (2013), for example, is fully probabilistic. The model was written as a function of the probability density functions (PDF) of cohesive, aerodynamic, and gravitational forces (inherent to the particle size distribution), completing the triad normally used in the study of particle emission. However, the PDF of aerodynamic forces, represented by shear stress, was obtained for global scale. In the present work, we proposed the description of the probability density function of aerodynamic forces on a local scale at the particle level by evaluating the friction velocity in a rough bed. The use of LES to calculate the distribution of probability density functions in a rough bed leads us to have more accurate results and includes the effects of non-erodible particles and the influence of the development of turbulent structures simultaneously.

Additionally, the threshold friction velocity of the particles (friction velocity from which the particles begin their movement), an essential variable in determining the emission of particulate matter, can also be described probabilistically. Duan et al. (2013) brings in their work a statistical model for threshold friction velocity for the movement of sand particles developed analytically and experimentally as a function of particle diameter. A suggestion for future work would be to use the PDF of the friction velocity at local scale in Klose and Shao (2013) model, as well as the PDF of the threshold friction velocity proposed by Duan et al. (2013). We would have more accurate particle emission results from a more robust approach to describe the erosion phenomenon.

References

An, Z. *et al.* (2018) 'Particulate Matter', *Current Allergy and Asthma Reports*, 18(15), pp. 3–9. Available at: https://doi.org/https://doi.org/10.1007/s11882-018-0768-8.

Antonia, R.A. (1977) 'Similarity of atmospheric Reynolds shear stress and heat flux fluctuations over a rough surface', *Boundary Layer Meteorology*, 12, pp. 351–364.

Arnastauskaitė, J., Ruzgas, T. and Braženas, M. (2021) 'An exhaustive power comparison of normality tests', *Mathematics*, 9(7). Available at: https://doi.org/10.3390/math9070788.

Badr, T. and Harion, J.L. (2005) 'Numerical modelling of flow over stockpiles: Implications on dust emissions', *Atmospheric Environment*, 39(30), pp. 5576–5584. Available at: https://doi.org/10.1016/j.atmosenv.2005.05.053.

Badr, T. and Harion, J.L. (2007) 'Effect of aggregate storage piles configuration on dust emissions', *Atmospheric Environment*, 41(2), pp. 360–368. Available at: https://doi.org/10.1016/j.atmosenv.2006.07.038.

Badr, T and Harion, J.-L. (2007) 'Quantification of diffuse dust emissions from open air sources on industrial sites', *3rd IASME/WSEAS International Conference on Energy, Environment and Sustainable Development (EEESD '07), ISBN: 978-960-8457-88-1*, (January), pp. 276–280.

Bové, H. *et al.* (2019) 'Ambient black carbon particles reach the fetal side of human placenta', *Nature Communications*, 10(1), pp. 1–7. Available at: https://doi.org/10.1038/s41467-019-11654-3.

Boyerinas, B.M. (2016) *Determining the Statistical Power of the Kolmogorov-Smirnov and Anderson-Darling Goodness-of-Fit Tests via Monte Carlo Simulation*.

Cheng, N.S. (2006) 'Influence of shear stress fluctuation on bed particle mobility', *Physics of Fluids*, 18(9). Available at: https://doi.org/10.1063/1.2354434.

Cheng, N.S., Sumer, B.M. and Fredsøe, J. (2003) 'Investigation of bed shear stresses subject to external turbulence', *International Journal of Heat and Fluid Flow*, 24(6), pp. 816–824. Available at: https://doi.org/10.1016/S0142-727X(03)00088-2.

Cheng, N.S., Tang, H. and Zhu, L. (2004) 'Evaluation of bed load transport subject to high shear stress fluctuations', *Water Resources Research*, 40(5). Available at: https://doi.org/10.1029/2003WR003001.

Cheng, N.-S. and Wing-Keung Law, A. (no date) 'Fluctuations of Turbulent Bed Shear Stress'. Available at: https://doi.org/10.1061/ASCE0733-93992003129:1126.

Colella, K.J. and Keith, W.L. (2003) 'Measurements and scaling of wall', *Experiments in Fluids*, 34, pp. 253–260.

Davidson, P.A. (2015) *Turbulence: an intrduction for scientists and engineers*. 2nd edn. New York: Oxford University Press.

Dentoni, V. *et al.* (2022) 'Emission of Fine Dust from Open Storage of Industrial Materials Exposed to Wind Erosion', *Atmosphere*, 13(2). Available at: https://doi.org/10.3390/atmos13020320.

Derakhshani, S.M., Schott, D.L. and Lodewijks, G. (2013) 'Dust emission modelling around a stockpile by using computational fluid dynamics and discrete element method', *AIP Conference Proceedings*, 1542, pp. 1055–1058. Available at: https://doi.org/10.1063/1.4812116.

Descamps, I., Harion, J.L. and Baudoin, B. (2005) 'Taking-off model of particles with a wide size distribution', *Chemical Engineering and Processing: Process Intensification*, 44(2), pp. 159–166. Available at: https://doi.org/10.1016/j.cep.2004.04.007.

Diego, I. *et al.* (2009) 'Simultaneous CFD evaluation of wind flow and dust emission in open storage piles', *Applied Mathematical Modelling*, 33(7), pp. 3197–3207. Available at: https://doi.org/10.1016/j.apm.2008.10.037.

Dreeben, T.D. and Pope, S.B. (1997) 'Probability density function and Reynolds-stress modeling of near-wall turbulent flows', *Physics of Fluids*, 9(1), pp. 154–163. Available at: https://doi.org/10.1063/1.869157.

Duan, S.Z., Cheng, N. and Xie, L. (2013) 'A new statistical model for threshold friction velocity of sand particle motion', *Catena*, 104, pp. 32–38. Available at: https://doi.org/10.1016/j.catena.2012.04.009.

Ferreira, A.D., Pinheiro, S.R. and Francisco, S.C. (2013) 'Experimental and numerical study on the shear velocity distribution along one or two dunes in tandem', *Environmental Fluid Mechanics*, 13(6), pp. 557–570. Available at: https://doi.org/10.1007/s10652-013-9282-7.

Ferreira, M.C.S., Furieri, B., A., O.E.M., *et al.* (2019a) 'A simple model to estimate emission of wind-blown particles from a granular bed in comparison to wind tunnel experiments', *Geomorphology*, 335, pp. 1–13. Available at: https://doi.org/10.1016/j.geomorph.2019.03.004.

Ferreira, M.C.S., Furieri, B., A., O.E.M., *et al.* (2019b) 'A simple model to estimate emission of wind-blown particles from a granular bed in comparison to wind tunnel experiments', *Geomorphology*, 335, pp. 1–13. Available at: https://doi.org/10.1016/j.geomorph.2019.03.004.

Ferreira, M.C.S., Furieri, B., Santos, J.M., *et al.* (2019) 'An experimental and numerical study of the aeolian erosion of isolated and successive piles', *Environmental Fluid Mechanics* [Preprint], (0123456789). Available at: https://doi.org/10.1007/s10652-019-09702-z.

Ferreira, M.C.S. *et al.* (2020) 'Experimental and numerical investigation of building effects on wind erosion of a granular material stockpile', *Environmental Science and Pollution Research*, 27, p. 14.

Franca, M.J. *et al.* (no date) *Quadrant Analysis of Coherent Structures in Open Channel Flows Over Mobile and Immobile Hydraulically Rough Beds*.

Furieri, B. (2012) *Erosion éolienne de tas de stockage de matières granulares sur sites industriels: amélioration des méthodes de quantification des émissions*. Université de Valenciennes et du Hainaut-Cambrésis.

Furieri, B. *et al.* (2012) 'Experimental surface flow visualization and numerical investigation of flow structure around an oblong stockpile', *Environmental Fluid Mechanics*, 12(6), pp. 533–553. Available at: https://doi.org/10.1007/s10652-012-9249-0.

Furieri, B. *et al.* (2013) 'Numerical modelling of aeolian erosion over a surface with non-uniformly distributed roughness elements', *Earth Surface Processes and Landforms*, 39(2), pp. 156–166. Available at: https://doi.org/10.1002/esp.3435.

Furieri, B. *et al.* (2014) 'Aeolian erosion of storage piles yards: Contribution of the surrounding areas', *Environmental Fluid Mechanics*, 14(1), pp. 51–67. Available at: https://doi.org/10.1007/s10652-013-9293-4.

Gillies, J.A., Nickling, W.G. and King, J. (2006) 'Aeolian sediment transport through large patches of roughness in the atmospheric inertial sublayer', *Journal of Geophysical Research: Earth Surface*, 111(2), pp. 1–13. Available at: https://doi.org/10.1029/2005JF000434.

Giostra, U., Cava, D. and Schipa, S. (2002) *STRUCTURE FUNCTIONS IN A WALL-TURBULENT SHEAR FLOW*.

Hadley, M.B., Vedanthan, R. and Fuster, V. (2018) 'Air pollution and cardiovascular disease: A window of opportunity', *Nature Reviews Cardiology*, 15(4), pp. 193–194. Available at: https://doi.org/10.1038/nrcardio.2017.207.

Hofland, B. and Battjes, J.A. (no date) 'Probability Density Function of Instantaneous Drag Forces and Shear Stresses on a Bed'. Available at: https://doi.org/10.1061/ASCE0733-94292006132:111169.

Huang, W. *et al.* (2009) 'Visibility, air quality and daily mortality in Shanghai, China', *Science of the Total Environment*, 407, pp. 3295–3300.

Iversen, J.D. *et al.* (1991) 'Roughness element effect on local and universal saltation transport', in OleE. Barndorff-Nielsen and BrianB. Willetts (eds) *Aeolian Grain Transport*. Springer Vienna (Acta Mechanica Supplementum), pp. 65–75. Available at: https://doi.org/10.1007/978-3-7091-6703-8_5.

Jia, W. *et al.* (2022) 'Turbulent transport dissimilarities of particles, momentum, and heat', *Environmental Research*, 211. Available at: https://doi.org/10.1016/j.envres.2022.113111.

Jimenez, J. and Moin, P. (1991) 'The minimal flow unit in near wall turbulence', *J. Fluid. Mech*, 225, pp. 213–240.

Keshavarzy, A. and Ball, J.E. (1997) *An analysis of the characteristics of rough bed turbulent shear stresses in an open channel*, *StochasficHydrology and Hydraulics*. Springer-Verlag.

Klose, M. and Shao, Y. (2013) 'Large-eddy simulation of turbulent dust emission', *Aeolian Research*, 8, pp. 49–58. Available at: https://doi.org/10.1016/j.aeolia.2012.10.010.

Liu, B., Qu, J. and Ning, D. (2018) 'Amplification factors to estimate wind erosion of piles of soil with different heights: Numerical simulation and structure-from-motion photogrammetry verification', *Journal of Soil and Water Conservation*, 73(4), pp. 377–385. Available at: https://doi.org/10.2489/jswc.73.4.377.

Liu, C.Q. *et al.* (2016) 'New omega vortex identification method', *Science China: Physics, Mechanics and Astronomy*, 59(8). Available at: https://doi.org/10.1007/s11433-016-0022-6.

López, M. V (1998) 'Wind erosion in agricultural soils: an example of limited supply of particles available for erosion ', *Catena*, 33(1), pp. 17–28. Available at: https://doi.org/http://dx.doi.org/10.1016/S0341-8162(98)00064-2.

Mangan, M.R. *et al.* (2022) 'Integrated Quadrant Analysis: A New Method for Analyzing Turbulent Coherent Structures', *Boundary-Layer Meteorology*, 184(1), pp. 45–69. Available at: https://doi.org/10.1007/s10546-022-00694-w.

Miller, M.R. (2020) 'Oxidative stress and the cardiovascular effects of air pollution', *Free Radical Biology and Medicine* [Preprint], (November 2019). Available at: https://doi.org/10.1016/j.freeradbiomed.2020.01.004.

Mingari, L.A. *et al.* (2017) 'Numerical simulations of windblown dust over complex terrain: The Fiambalá Basin episode in June 2015', *Atmospheric Chemistry and Physics*, 17(11), pp. 6759–6778. Available at: https://doi.org/10.5194/acp-17-6759-2017.

Miri, A., Dragovich, D. and Dong, Z. (2017) 'Vegetation morphologic and aerodynamic characteristics reduce aeolian erosion', *Scientific Reports*, 7(1), pp. 1–9. Available at: https://doi.org/10.1038/s41598-017-13084-x.

Miyagi, N. *et al.* (2000) 'Statistical analysis on wall shear stress of turbulent boundary layer in a channel ¯ow using micro-shear stress imager', *International journal of heat and fluid flow*, 21, pp. 576–581. Available at: www.elsevier.com/locate/ijh.

Mohd Razali, N. and Bee Wah, Y. (2011) *Power comparisons of Shapiro-Wilk, Kolmogorov-Smirnov, Lilliefors and Anderson-Darling tests*, *Journal of Statistical Modeling and Analytics*.

Neuman, Cheryl Mckenna, W.G.N. (1995) 'Aeolian sediment flux decay: Non-linear behaviour on developing deflation lag surfaces', *Earth Surface Processes and Landforms*, 20(5), pp. 423–435.

Niño, Y. and Garcia, M.H. (1996) 'Experiments on particle-turbulence interactions in the near-wall region of an open channel flow: Implications for sediment transport', *J. Fluid Mech*, 326, pp. 285–319.

Novak, L. *et al.* (2015) 'Numerical Modeling of Dust Lifting from a Complex-Geometry Industrial Stockpile', *Strojniski Vestnik/Journal of Mechanical Engineering*, 61(11), pp. 621–631. Available at: https://doi.org/10.5545/sv-jme.2015.2824.

Reeks, M.W. (2005) 'On probability density function equations for particle dispersion in a uniform shear flow', *Journal of Fluid Mechanics*, 522, pp. 263–302. Available at: https://doi.org/10.1017/S0022112004001922.

Richefeu, V., El Youssoufi, M.S. and Radjaï, F. (2006) 'Shear strength properties of wet granular materials', *Physical Review E - Statistical, Nonlinear, and Soft Matter Physics*, 73(5). Available at: https://doi.org/10.1103/PhysRevE.73.051304.

Romeo, A. *et al.* (2017) 'Dust emission and dispersion from mineral storage piles', *Environmental Science and Pollution Research*, 24(28), pp. 22663–22672. Available at: https://doi.org/10.1007/s11356-017-9881-9.

Sarmiento, O.A. and Falcon, M.A. (2006) 'Critical Bed Shear Stress for Unisize Sediment', *Journal od hidraulic engineering*, pp. 172–179. Available at: https://doi.org/10.1061/ASCE0733-94292006132:2172.

Savage, S.B. and Jeffrey, D.D.J. (1951) *The stress tensor in a granular flow at high shear rates*, *J. Fluid Mech.*

Seaton *et al.* (2020) 'Pollution, Particles, and Dementia: A Hypothetical Causative Pathway', *International Journal of Environmental Research and Public Health*, 17(3), p. 862. Available at: https://doi.org/10.3390/ijerph17030862.

Séchet, P. (2000) *Contribution à l'étude des structures cohérentes en turbulence de paroi, de leur influence sur le transport des sédiments dans le cas du charriage*. Institut National Polytechnique de Toulouse, France.

Shih, W.R. *et al.* (2017) 'Accounting for the role of turbulent flow on particle dislodgement via a coupled quadrant analysis of velocity and pressure sequences', *Advances in Water Resources*, 101, pp. 37–48. Available at: https://doi.org/10.1016/j.advwatres.2017.01.005.

Sigaux, J. *et al.* (2019) 'Air pollution as a determinant of rheumatoid arthritis', *Joint Bone Spine*, 86(1), pp. 37–42. Available at: https://doi.org/10.1016/j.jbspin.2018.03.001.

Smith, I.B., Spiga, A. and Holt, J.W. (2015) 'Aeolian processes as drivers of landform evolution at the South Pole of Mars', *Geomorphology*, 240, pp. 54–69. Available at: https://doi.org/10.1016/j.geomorph.2014.08.026.

Swet, N. and Katra, I. (2016) 'Reduction in soil aggregation in response to dust emission processes', *Geomorphology*, 268, pp. 177–183. Available at: https://doi.org/10.1016/j.geomorph.2016.06.002.

Tiwary, A. and Colls, J. (2010) *Air pollution: measurement, modelling and mitigation*. 3rd edn, *Choice Reviews Online*. 3rd edn. New York: Routledge Taylor and Francis Group. Available at: https://doi.org/10.5860/choice.47-4447.

Toraño, J.A. *et al.* (2007) 'Influence of the pile shape on wind erosion CFD emission simulation', *Applied Mathematical Modelling*, 31(11), pp. 2487–2502. Available at: https://doi.org/10.1016/j.apm.2006.10.012.

Toure, A. *et al.* (2011) 'Impact of very low crop residues cover on wind erosion in the Sahel', *Catena*, 85(3), pp. 205–214. Available at: https://doi.org/10.1016/j.catena.2011.01.002.

Turpin, C., Badr, T. and Harion, J.L. (2010) 'Numerical modelling of aeolian erosion over rough surfaces', *Earth Surface Processes and Landforms*, 35(12), pp. 1418–1429. Available at: https://doi.org/10.1002/esp.1980.

Turpin, C. and Harion, J.L. (2009) 'Numerical modeling of flow structures over various flat-topped stockpiles height: Implications on dust emissions', *Atmospheric Environment*, 43(35), pp. 5579–5587. Available at: https://doi.org/10.1016/j.atmosenv.2009.07.047.

Turpin, C. and Harion, J.L. (2010) 'Effect of the topography of an industrial site on dust emissions from open storage yards', *Environmental Fluid Mechanics*, 10(6), pp. 677–690. Available at: https://doi.org/10.1007/s10652-010-9170-3.

USEPA (2006) '13.2.5 Industrial wind erosion', *Compil Air Pollut Emiss Factors*, 1. Available at: https://doi.org/10.1130/0091-7613(1998)026<0363.

Versteeg, H. and Malalasekera, W. (2007) *An Introduction to Computational Fluid Dynamics: The Finite Volume Method*. 2nd edn. Pearson. Available at: https://doi.org/10.2514/1.22547.

Wang, Y. *et al.* (2022) 'Improved Quadrant Analysis for Large-Scale Events Detection in Turbulent Transport', *Atmosphere*, 13(3). Available at: https://doi.org/10.3390/atmos13030489.

Wu, D. *et al.* (2005) 'An extremely low visibility event over Guangzhou region: a study case', *Atmospheric Environment*, 39, pp. 6568–6577.

Xie, Z.T., Coceal, O. and Castro, I.P. (2008) 'Large-Eddy simulation of flows over random urban-like obstacles', *Boundary-Layer Meteorology*, 129(1), pp. 1–23. Available at: https://doi.org/10.1007/s10546-008-9290-1.

You, S. and Wan, M.P. (2017) 'Statistical analysis of fine particle resuspension from rough surfaces by turbulent flows', *Aerosol and Air Quality Research*, 17(4), pp. 843–856. Available at: https://doi.org/10.4209/aaqr.2016.03.0106.

Yu, W., Vinkovic, I. and Buffat, M. (2016) 'Finite-size particles in turbulent channel flow: quadrant analysis and acceleration statistics', *Journal of Turbulence*, 17(11), pp. 1048–1071. Available at: https://doi.org/10.1080/14685248.2016.1215603.

Zhang, Y. ning *et al.* (2019) 'Comparisons and analyses of vortex identification between Omega method and Q criterion', *Journal of Hydrodynamics*, 31(2), pp. 224–230. Available at: https://doi.org/10.1007/s42241-019-0025-1.

Ziskind, G., Fichman, M. and Gutfinger, C. (1995) 'Ressuspension of particulates from surfaces to turbulent flow - Review and analysis', *J. Aero. Sci*, 26, pp. 613–644.

Zou, X. *et al.* (2022) 'Soil wind erosion rate on rough surfaces: A dynamical model derived from an invariant pattern of the shear-stress probability density function of the soil surface', *Catena*, 219. Available at: https://doi.org/10.1016/j.catena.2022.106633.

6.3. Similarity analysis of the flow over a granular material bed

The technical note presented in this section brings an overview and brief discussion about similarity analysis between wind tunnels and full-scale scenarios regarding particles emission and transportation. A methodology is proposed to discuss wind tunnel simulations design take into account the already known requirements for reach similarity for full-scale scenarios in addition to evaluation of $CoSh$ and Stokes number, related to non-erodible and erodible particles, respectively. The main idea is that the kinematic and dynamic similarities can be incorporated directly into the methodology. Kinematic similarity is considered when the velocity profile is equalized on both scales. Dynamic similarity is considered in the dimensionless numbers that are essentially a balance between forces. Unfortunately, it was not possible to directly evaluate the geometric similarity. No parameter in the analysis carried out brings information about any geometric scaling on the two scales. However, the hope is that based on what is raised in the paper, the scientific community can propose advances in the analysis of similarity regarding particle studies, which to date remains a challenge and a gap in the literature.

A discussion on similarity analysis of particles behavior under wind erosion

C. L. Morais [a], B. Furieri [a], M. C. S. Ferreira [b], J.-L. Harion [c], N. C. Reis Jr [a], J. M. Santos [a]

[a] *Federal Univerisity of Espírito Santo, Departament of Environmental Engineering, 29075-910, Brazil*

[b] *Federal Institute of Education, Science and Technology of Espírito Santo, Mathematics Coordination, 29040-780, Brazil*

[c] *IMT Nord Europe, EI, F-59500, France*

Abstract

Wind tunnels are frequently used to simulate aeolian erosion in small-scale studies of particles emission and their modes of transportation. The present work presents a discussion on similarity analysis between wind tunnel and real scale of wind flow over a bed of particles aiming to overcome the limitation of geometric similarity that arises in case of particles of air pollution interest by assuming that the physical principles governing the erodibility of particles (shear stress, gravity and cohesion) and their transportation mode that prevails are the same in both scales as well as the similarity criteria for the atmospheric boundary layer dynamic. We propose the analysis of two dimensionless numbers for non-erodible and erodible particles, respectively, $CoSh$ *and Stokes numbers.* $CoSh$ *number indicates the reason why non-erodible particles resist to the wind shear stress (gravity or cohesion effect) and Stokes number indicates what kind of movement the erodible particles will perform after being emitted based on the interaction between them and the turbulent vortices.*

Keywords: *Dimensional analysis, Particulate matter, Dust emission, Wind erosion, Experimental procedure design.*

1 Introduction

Wind flowing over surfaces composed of loose material can cause aeolian erosion, transporting particles for long distances or even to the near surroundings. How does airflow put particles in motion? How do particles behave according to their size, shape, chemical composition, and wind conditions? These are extremely important questions to the understanding of aeolian erosion. Although this natural process regards atmospheric emissions of particles that can cause an impact on human health, most work found in the literature concerns erosion of soil particles in the order of 0.2-30 mm, while particles of air pollution interest are in the order of 2.5-100 μm.

A wind tunnel is a useful tool to simulate aeolian erosion and is very much used to model, at smaller scale, particles emission and their mode of transportation, allowing simulations in a controlled environment not possible in fields measurements, see for instance, the recent works of Marshall et al. (2021), Jiang et al. (2021), Jiang et al. (2022), Mina et al. (2022) and Zhang et al. (2022). However, despite these advantages, a small-scale study can compromise the reliable reproduction of the large-scale phenomena.

It is well known that to obtain full similarity between a phenomenon occurring on a reduced scale (model) and real scale (prototype), it is necessary to achieve geometric, kinematic, and dynamic similarities. Geometric similarity means that the model has the same shape as the prototype. Kinematic similarity states that the model and the prototype must develop similar fluid flow. Dynamic similarity indicates that the ratio of different forces acting on the fluid particles and boundary surfaces must be identical in both scales.

Raffaele et al. (2021) discussed that studies on similarity requirements for wind tunnel simulation of aeolian erosion started many years ago with the efforts of several authors, mainly for snow drift (Strom et al., 1962; Snyder, 1972; Kind, 1976; Iversen, 1980; Anno, 1984; White, 1996). However, it is important to point out that geometric, kinematic, and dynamic similarities cannot be satisfied simultaneously if one is dealing with aeolian erosion (Aliabadi, 2018; Sherman, 2020; Raffaele et al., 2021). In addition, Reynolds number (Re) independence, about 10^5 (Kato and Hanafusa, 1996; Woodruff and Zingg, 1953), claimed as the condition in which turbulence is such that variations between the model and the prototype could be neglected is questionable. Chew et al. (2018) argued that only the Reynolds independence, is not enough to guarantee the same behavior on prototype and model in a similar flow, since it seems that *Re* is highly influenced by the geometry considered. In general words, there would be different Reynolds number of independence for different cases.

A major problem emerges for the geometric similarity of particles. For most scenarios concerning applications of air pollution interesse, the particles used in wind tunnels should be extremely small to meet similarity to real scale which is even more difficult if erosion is occurring in stockpiles, for instance. This would lead to strong cohesive influences, a very complex phenomenon that might not be happening in real scale particles. Another issue is that working with very small particles leads to enormous technical difficulties, for instance, health and safety for those running the experiments and acquisition of appropriate particles in terms of size distribution and composition, if not to use the actual material (particles) of interest. These are some of the reasons why studies on cohesion and hence, fine particles, are still very limited. Other important reasons arise from the complexity of cohesion phenomenon itself.

This work brings a discussion and proposition on how to evaluate similarity between wind tunnel and real-scaled particle beds that helps overcome some gaps in wind tunnel simulation. To build this discussion, a review of similarity requirements for laboratory simulation of lower Atmospheric Boundary Layer (ABL) and simulation of the flow over a particle bed is presented, as well as a discussion about the problems or vexation related to particle threshold friction velocity determination.

A hypothetical case is discussed to illustrate how to use the similarity analysis methodology proposed in wind tunnel experiments design.

2 Similarity theory applied to particle flow

2.1 Laboratory simulation of the lower Atmospheric Boundary Layer (ABL)

Firstly, we revisit the criteria for achieving similarity for laboratory simulation of lower ABL. Non-dimensional conservation equations or the Buckingham Pi Theorem lead to dimensionless groups or similarity parameters. The equivalence of these groups on the small scale of the wind tunnel and the real scale determines if the phenomenon in both scales is similar. From this procedure on the motion equation, the most used and significant parameter that can be found is the Reynolds number (calculated based on free stream velocity and the boundary layer height). For the wind flow in the ABL, there is a widely accept critical value (10^5) (Kato and Hanafusa, 1996; Woodruff and Zingg, 1953) to assure that the model is dynamically similar to the real scale.

In addition to Reynolds number, it is worth also considering the log wind velocity vertical profile often used in atmospheric emission and dispersion studies. For an adiabatic surface layer over a rough surface, this profile is given by:

$$\bar{u}(z) = \frac{u^*}{\kappa} ln\left(\frac{z}{z_o}\right) \tag{1}$$

where u^* is the wind friction velocity ($\sqrt{\tau_o/\rho}$) [m/s] being ρ is the fluid density [kg/m³] and τ_o the shear stress on the ground [Pa], κ is the von Kárman constant, z is the height [m] where the mean velocity $u(z)$ [m/s] is determined and z_o is the roughness length related to the height of roughness elements on the surface [m].

According to Kato and Hanafusa (1996), the similarity of the vertical velocity distribution can be obtained if u^* and z_0 can be matched in both scales, or if the roughness Reynolds number (based on the friction velocity and the roughness length) is the same in both scales (White, 1996). As turbulent intensity, Reynolds number and Reynolds stress are related to u^*, keeping this variable in both scales necessary brings other parameters to satisfy the flow similarity except the turbulence spectra (Kato and Hanafusa, 1996).

In practice, matching the mean velocity profiles involves setting on the wind tunnel floor rough elements that lead to the surface roughness length (z_0) of interest. White (1996) reports that it is not possible to match the turbulence intensity in the whole vertical profile in the wind tunnel simulation due to turbulence scaling effects. The author suggests that the longer, and the larger, the test section for flow development, the better the turbulent intensity agreement between the wind tunnel and the real scale. Implying the same for the turbulent energy spectra profiles. Additionally, Burke (1982) reported that the introduction of flow spires at the wind tunnel inlet could improve the energy spectra of the wind tunnel, possibly resulting in a reduction in the length of the test section.

To guarantee the boundary layer similarity, it is necessary to assure that both scales are under the same shear stress ($u_R^* = u_{wt}^* = u^*$) and the same vertical velocity profile. So, the roughness of the wind tunnel velocity profile that must be set at the wind tunnel as $z_{0,wt} = (z_{wt})/(z_{0,R}/\, z_R)$ where the subscript wt stands for the small scale in the wind tunnel and R for the real scale.

2.2 Laboratory simulation of the flow over a granular material bed

2.2.1 Initiation of particles movement

After revisiting the criteria for achieving similarity for laboratory simulation of lower ABL, we quest to find similarity parameters regarding the initiation of particles motion. The initiation of motion depends on the forces acting on the particles subject to wind erosion (**Figure 1**). These forces are separated into the ones that act to move the particles (such as drag force F_d and lift force F_l, called aerodynamic forces) and forces that act to resist their movement (such as gravity force F_g and cohesive force between particles F_c).

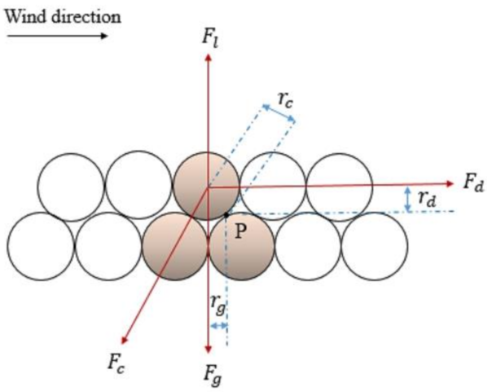

Figure 1. Forces acting on the particle subjected to a velocity gradient: lift, drag, cohesion, and gravity.

To lift the particle, the moments due to F_d and F_l relative to point P must exceed the resisting moments due F_g and F_c:

$$r_d F_D + r_g F_l > r_g F_g + r_c F_c \tag{2}$$

where r_d, r_g and r_c are the corresponding moment arm lengths associated with the forces.

The drag force arises from pressure differences between the frontal and the wake region of the particle and from *momentum* transfer from the surrounding fluid to the particle through molecular motion or the so-called viscous effect. It can be defined as the force in the opposite direction of the relative velocity exerted by the fluid on the particle. This force can be approximated by (Shao, 2008):

$$F_d = K_d D_p{}^2 \rho u^{*2} \quad (3)$$

where K_d is a dimensionless empirical parameter function of the particle Reynolds number ($Re_p^* = u^* D_p/\nu$) suggested to have a magnitude around 4 (Shao and Lu, 2000) and D_p is the particle diameter [m].

An aerodynamic lift emerges from the shear in the direction of decreasing velocity that promotes a normal pressure gradient (Shao, 2008):

$$F_l = K_l D_p{}^2 \rho u^{*2} \quad (4)$$

where K_l is a dimensionless empirical parameter suggested to have a magnitude around 2 by Shao and Lu (2000).

The gravitational force for a particle with density ρ_p is:

$$F_g = \frac{\pi}{6} D_p{}^3 (\rho_p - \rho) g \quad (5)$$

where g is gravity acceleration.

The cohesive force consists of (i) van der Waals, (ii) electrostatic, (iii) capillary (if moisture is considered), and (iv) chemical bonding forces (formed if salts, mainly in soils, interact with clay particles and form chemical bonds). The values of inter-particulate forces can vary widely, depending on the chemical composition of the particles, their shape and surface texture, bulk water content, and processing history (Clayton, 2019). Cohesive forces can be considered the most challenging of all particle-particle interactions and are difficult to quantify and model precisely (Shao, 2008; Clayton, 2019).

As pointed out by Shao and Lu (2000), for spherical particles free of the influence of moisture and chemical bonding, the cohesion can be mainly attributed to the van der Wall and electrostatic forces. The van der Waals forces are responsible for the attraction between uncharged particles of very small diameter. For two same-sized particles of diameter D_p separated by a distance d in which $d/D_p \ll 1$, one approximation for the value of van der Waals force (F_{iv}) between these two particles in *vacuum* is:

$$F_{iv} = \frac{h_w}{32\pi d^2} D_p \tag{6}$$

where h_w is a coefficient varying between $10 - 18$ J and $10 - 21$ J, depending on the material. The smallest value of d is conventionally considered to be 0.4 nm because, below this distance, repulsion between the particles can be noticed (Theodoor and Overbeek, 1985). For $d/D_p > 0.2$, the van der Waals attraction becomes negligible, being of the order of the Brownian forces.

The electrostatic force (F_{ie}) applicable to dust emission is the non-conductor force. For smooth and ideally spherical particles, they can be written as:

$$F_{ie} = \frac{\pi B_p V^2 D_p}{2d} \tag{7}$$

where V is the contact potential difference, which generally ranges from 0 to about 0.5 volts, d is the separation between the two adhering particles and B_p is the permittivity of free space.

Under ideal conditions, such as the absence of moisture and cohesive effects between particles, Bagnold (1941) combined Equations (2),(3), and (5) to find a velocity parameter to describe a threshold for particle emission called threshold friction velocity (u_t^*), showed in Equation (7).

$$u_t^* = A_B \sqrt{\frac{\rho_p - \rho}{\rho} g D_p} \tag{8}$$

where A_B is Bagnols's constant, approximately 0.11 for particle diameters larger than 100 μm. With the development of an equation for the take-off of particles, it becomes possible to evaluate the particle's erodibility. If the friction velocity at the surface does not reach the threshold friction velocity of the material ($u^* < u_t^*$), the particles tend to remain on the surface. If the opposite occurs ($u^* > u_t^*$), the movement of the particles begins.

However, Bagnold's proposal had limitations, such as considering the balance only between drag and gravity forces and not being well defined for small diameters (strongly affected by cohesion) which leads to the fact that u_t^* tends to zero for very small particles. Thus, subsequent experimental and theoretical studies emerged resulting in other expressions for u_t^* (see Kok et al. (2012)). The most recent attempt to model the threshold friction velocity was carried out by Shao and Lu (2000), who developed an expression based on the balance between drag, lift, gravitational, and cohesive forces:

$$u_t^* = A_N \sqrt{\frac{\rho_p - \rho}{\rho} g D_p + \frac{\gamma}{\rho D_p}} \tag{9}$$

where A_N is a constant equal to A_B for particle diameters greater than 100 μm (0.11) and γ is the surface energy that characterizes the cohesion $[Pa\ s$ or $kg/(m\ s)]$.

Despite being very promising, Equation (9) represents a challenge in determining the threshold friction velocity for different materials and particle diameters. The reason why this happens is that in Equation (99), A_N and γ, are unknown for diameters smaller than 100 μm and for different materials, respectively. Regarding the surface energy (γ), Shao and Lu (2000) consider that it includes all possible cohesive effects (van der Walls, electrostatic, capillary, etc.). According to the same authors, A_N would be a function of the particle friction Reynolds number. However, it is not yet known for sure how to carry out the estimation of these variables and there are still many disagreements among authors in literature. Sherman (2020) interprets that γ accounts only electrostatic effects and the other factors that could cause cohesion between small particle would be represented in A_N, in disagreement with Shao and Lu (2000). Burr et al. (2020) follow another line, going back to the use of the Bagnold equation, which leads us to believe that all cohesive effects would be included in A_B. The formulations, however, do not clearly indicate that A_B take into account any inter-particle interaction.

Clayton (2019) points out that one of the most challenging factors in threshold friction velocity determination is the cohesive effects, especially if dealing with fine particles. The values of inter-particulate forces can vary widely, depending on the chemical composition of the particles, their shape and surface texture, bulk water content, processing history, and other constraint mechanisms (Clayton, 2019). Cohesive forces are difficult to quantify and model (Shao, 2008; Clayton, 2019) bringing a source of uncertainty to the study of dust emission. Laboratory experiments (Shao, 2008) indicate that a wide range of dispersion in the measurements of cohesive forces may occur for nearly identical macroscopic conditions. This dispersion increases with the decrease in particle size, and the spread can be as large as several orders of magnitude.

To exemplify this randomness, Shao and Klose (2016) used the values of the surface energy of 0.75×10^{-4} and 1.5×10^{-4} kg/s^2 for the estimation of friction velocity using Shao and Lu (2000) (Equation (9)). The results showed that there is a very important shift between the curves using the two values of γ if particle diameters less than 100 μm are observed (see **Figure 2**). This clearly shows how dispersive the cohesive forces can be, separating a potentially deterministic part of the curve (for diameters larger than 100 μm) and an extremely stochastic part of the curve (for diameters less than 100 μm).

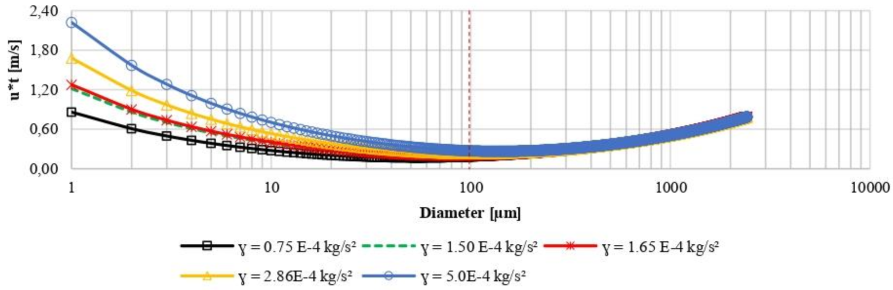

Figure 2. Shao and Lu's (2000) take-off criterion plotted for $\gamma = 0.75 \times 10^{-4}$ kg/s², $\gamma = 1.50 \times 10^{-4}$ kg/s², $\gamma = 1.65 \times 10^{-4}$ kg/s², $\gamma = 2.86 \times 10^{-4}$ kg/s² and $\gamma = 5.00 \times 10^{-4}$ kg/s². It is possible to observe that not only for particles less than $100\ \mu$m the take-off curve behaves in a stochastic way. The statement of a more stochastic part (diameters less than $100\ \mu$m) and a more deterministic part (diameters higher than $100\ \mu$m) is valid for specific ranges of superficial energy (γ).

It is important to state that measuring the surface energy of solid particles is not an impossible task. However, it must be performed specifically for the material of interest. There are a few methods to perform such measurements, for instance, by Atomic Force Microscopy. Shao and Lu (2000) proposed the use of values from 1.65×10^{-4} to 5.00×10^{-4}kg/s² and Kok and Renno (2009) obtained 2.86×10^{-4} kg/s² from experiments.

2.2.2 Non-erodibility of particles

Finally, we applied the Buckingham Pi Theorem to find the similarity parameters that guarantee that the force responsible for the particles non-erodibility is the same in both scales, meaning cohesion or gravity.

The variables listed for the Buckingham Pi Theorem were those involved in particles emission representing aerodynamic, gravity, and cohesion forces: shear stress (ρu_*^2), particle density (ρ_p), air density (ρ), gravity (g), particle diameter (D_p) and the surface energy (γ). After the selection, the variables were grouped into two Pi groups: Cohesion and Shields numbers (Shields number was initially proposed by Shields (1936)). The Cohesion number is the ratio of the cohesion force related to particles properties to the shear force exerted by the flow:

$$Co = \frac{\gamma}{\rho u_*^2 D_p} \tag{10}$$

The Shields number represents the ratio of the shear force exerted by the air on a particle at the bed surface to the effective particle mass:

$$Sh = \frac{\rho u_*^2}{(\rho_p - \rho) g D_p} \quad (11)$$

By multiplying Cohesion and Shields numbers, the shear stress can be disregarded. Therefore, the $CoSh$ number directly gives information about which effect prevails to explain the non-erodibility of particles, cohesion, or gravity.

$$CoSh = \frac{\gamma}{(\rho_p - \rho_{air}) g D_p^2} \quad (12)$$

If a particle is identified as non-erodible (through the calculation of its threshold friction velocity), cohesion force influences particles non-erodibility for larger values of $CoSh$. While small values of $CoSh$ indicates that particles non-erodibility is governed by gravity. The critical values of $CoSh$ can only be determined by experiments. Nevertheless, the important point here is that it must be assured that in the wind tunnel and the real scale, the reason why particles are non-erodible is the same.

Another important issue to be discussed in this context is that the Shao and Lu (2000) equation (Equation (9)) for the emission criterion obtained analytically from the equilibrium of forces is directly related to the $CoSh$ number obtained through Buckingham Pi Theorem. Note that $CoSh$ number is identical to the ratio between the two terms inside the square root of Equation (9). For instance, let us apply Equation (9) to sand particles of $100\ \mu m$ of diameter. The term $(\rho_p - \rho_{air}) g D_p / \rho_{air}$ takes a value of about 1, since the particle density ($2650\ kg/m^3$) is much higher that then the air density ($1.225\ kg/m^3$), $\rho_p - \rho_{air} \approx \rho_p \approx 10^3$, and gravity acceleration is $g \approx 10$. Thus $(\rho_p - \rho_{air}) g D_p / \rho_{air} \approx 10^3 \times 10 \times 10^{-4} \approx 1$. The same happens with the term $\gamma / \rho_{air} D_p$, since the superficial energy has order of magnitude of 10^{-4}. Thus, $\gamma / \rho_{air} D_p \approx 10^{-4} / 10^{-4} \approx 1$. This shows that the two terms inside the square root of Equation (9) have the same order of magnitude and this value is 1, the same value that shows the total equilibrium between cohesion and gravity forces in the $CoSh$ number. This rises the attention to the $CoSh$ number for dynamic similarity analysis of the dominant force responsible for the particles non-erodibility.

2.2.3 Particles transport mechanism

In addition to achieve similarity regarding the forces responsible for the particles non-erodibility, it is also important to find similarity parameters, which guarantees that once the threshold friction velocity is exceeded, the entrained erodible particles transportation mode is the same in both scales.

According to Bagnold (1941), depending on particle properties and wind conditions, there are three modes of particle motion: suspension (pure or modified), saltation (pure or modified), and creep. Suspension movement is associated with small particles that are taken-off from the surface by lift forces and entrained due to turbulent movements of air flow. Modified suspension movements occur to slightly heavier particles that do not follow the small-scale turbulent eddies due to their inertia. Particles eroded with pure suspension movements reach distances from the take-off point further than those under modified suspension movements. Particles in saltation mode rebound hitting a bed of particles as after take-off, gravity force becomes more important than the lift force. A saltation particle can disturb the surface during its rebounds causing an extra emission. Heavier particles are likely to perform a creep motion, rolling over the surface.

Shao (2008) proposes that there are three mechanisms by which particles of small diameters are suspended: Aerodynamic lift, saltation bombardment, and disaggregation. In the aerodynamic lift, particles are lifted from the bed surface directly by aerodynamic forces (Loosmore and Hunt, 2000). However, this mechanism occurs with a smaller probability compared to the two others. This happens because, for very small particles, the importance of gravity and aerodynamic forces decreases as inter-particle cohesion becomes important. Saltation bombardment or sandblasting (Alfaro *et al.*, 1997) causes emission of small particles by the impact of the large ones on the surface overcoming the bonding forces that act to maintain the particles on the bed. According to Shao et al. (1993), the saltation bombardment is one order more effective than the aerodynamic lift. Disaggregation or auto-abrasion occurs if a set of dust particles attached to sand grains disintegrate during a strong wind erosion event or saltation.

The particles transport mode of saltation or suspension can be identified by the Stokes Number (St). The Stokes number is a dimensionless parameter characterizing the particle inertia to the flow. The Stokes number based on the Kolmogorov scale (Balachandar, 2009; Berk and Coletti, 2020; Oujia et al., 2020) is defined by the ratio of the characteristic time scale of the particle (τ_p) to the characteristic time scale of turbulence (τ_t):

$$St = \frac{\tau_p}{\tau_t} \tag{13}$$

The parameter τ_p is the particle relaxation time which defines the time required for the particle to adjust its velocity if a sudden change occurs in flow conditions:

$$\tau_p = \frac{\rho_p D_p^2}{18\mu} \tag{14}$$

where μ is the air dynamic viscosity [Pa.s].

A turbulent flow is made up of vortex movements of scales extending over a whole range of values. Two categories of vortices can be distinguished within the ABL. Large vortices, which carry energy and have a characteristic time scale equal to (Tanière et al., 1997):

$$\tau_L = \delta/0.1U_\infty \tag{15}$$

where U_∞ is the free stream velocity [m/s] and δ is boundary layer thickness [m] and the characteristic height used to parameterize the largest vortices possible to be developed in the airflow over a particle bed. And small vortices, called dissipative vortices, which have a characteristic time equal to (Tanière et al., 1997):

$$\tau_l = (\mu\delta/(0.1U_\infty)^3)^{\frac{1}{2}} \tag{16}$$

The particle relaxation time τ_p is compared to the time scales τ_l and τ_L. For small values of $St_l = \tau_p/\tau_l$ and $D_p \ll \eta$ (Kolmogorov length scale), particles are weightless and small enough to be driven by the turbulent flow to be suspended. According to Wyngaard (2010), η can be approximated by the relationship it has with the large scales, defined by the height of the boundary layer (δ), and the Reynolds number:

$$\eta = \frac{\delta}{(Re)^{3/4}} \tag{17}$$

On the other hand, saltation is observed for particles whose behavior is not mainly influenced by turbulence effects but governed by inertia, gravity, and particle-wall collision phenomena (Tanière et al., 1997). Such particles are characterized by large values of $St_L = \tau_p/\tau_L$. Tanière et al. (1997) call these movements pure suspension and pure saltation. See Tanière et al. (1997) for more details. The critical values of St_L and St_l for saltation or suspension can only be determined by experimental simulations. Nevertheless, the important point here is that it must be assured that in the wind tunnel and the real scale, the mode of transportation is the same.

As discussed by Taniere et al. (1997), the behavior of particles after taking off can be also determined by the crossing trajectory parameter calculated as the ratio between the particle free fall velocity and the friction velocity:

$$C_{tp} = \frac{V_g}{u_t^*} \tag{18}$$

where V_g terminal particle velocity and u_t^* is the friction velocity. If $C_{tp} > 1$, the particle is in saltation or modified saltation mode. If $C_{tp} < 1$, the particle is in suspension or modified suspension mode.

Particles that are neither in pure suspension nor in pure saltation have their behavior related to both turbulence and particle inertia effects as a velocity lag between the fluid and the particles may exist, and some particle—wall interaction can occur. These behaviors can be indicated by the comparison between particles relaxation time and the time scale for larger eddies for saltation and the Kolmogorov time scale for suspension.

3 A case study for analyzing the influence of cohesion or gravity and mechanism of transport

To verify which force is dominant on the particle non-erodibility (cohesion or gravity) and to identify the mode of transport for erodible particles (see **Figure 3** for non-erodible particles and **Figure 4** for erodible particles), it is necessary to gather information about the real scale: atmospheric data (ρ_{air}, μ_{air}, g), the boundary layer height (δ_R), the measured velocity (U_R) at the referent height ($z_{r,R}$), reference height where velocity is being measured, the roughness of the terrain ($z_{0,R}$) and the wind friction velocity (u_R^*) upwind the surface being eroded, particle diameter ($D_{p,R}$), particle density ($\rho_{p,R}$), the threshold friction velocity ($u_{t,R}^*$) and the real particle surface energy ($\gamma_{p,R}$). The real scale Reynolds number (Re_R) is calculated based on the free stream velocity and the boundary layer height. $u_R^* < u_{t,R}^*$ corresponds to the case of non-erodible particles and one should determine which cohesion or gravity is responsible for the non-erodibility. If $u_R^* < u_{t,R}^*$, it is the case of erodible particles, and one should determine the mechanism of transport (saltation or suspension).

To determine what particles would be suitable for representing the non-erodible particles from a real case scenario in the wind tunnel, $D_{p,wt}$ and $\rho_{p,wt}$ should be initially chosen (as a first choice for the first set of particles, which should be non-erodibles) and $u_{t,wt}^*$ should be calculated to verify if $u^* < u_{t,wt}^*$ (non-erodible particles), if it is not, the chosen particles must be reevaluated. Then, the $CoSh$ number should be calculated for both scales. Ideally $CoSh_{wt} = CoSh_R$, and one option would be using the same material from the real scale in the wind tunnel. However, as discussed earlier, if particles of air pollution relevance are considered, for instance, particles smaller than 10 µm (that causes health effects on humans), it may not be practical to use the same particles diameter in the wind tunnel. In that case, if particles in the wind tunnel are chosen much larger (order of magnitudes larger) than the ones in real scale, then, their density should be drastically reduced and, in practice, unrealistic. Or yet, even if the real scale concerns larger particles, but it is desired to use a different material in the wind tunnel, it will not be possible to keep the same exact $CoSh$ number in both scales. In that case, we propose an assumption that there is a critical $CoSh$ number. Thus, instead of matching this number in both scales, we could assume that for $CoSh$ number larger than a critical value, the cohesion forces would be responsible for the non-erodibility, and for $CoSh$ number smaller than the critical value, gravity forces would be the dominant force responsible for the non-erodibility. It would guarantee that a non-erodible particle would be non-erodible due to the same force type in both scales, and it would give more flexibility to find appropriate particles (size and material) to represent the real scale phenomena in the wind tunnel. Let us assume that the critical $CoSh$ is equal to unity. Therefore, for the purpose of the present work, if $CoSh_R$ is larger than one, then $CoSh_{wt}$ must also be larger than one so to reach similarity. And for that to be achieved appropriate values of $D_{p,wt}$, $\rho_{p,wt}$ and U_{wt} must be found. If

$CoSh_R > 1$ and $CoSh_{wt} < 1$, the chosen values of $D_{p,wt}$ and $\rho_{p,wt}$ should be reevaluated. Analogously if $CoSh_R < 1$ and $CoSh_{wt} > 1$.

To determine what particles would be suitable for representing the erodible particles from a real case scenario in the wind tunnel, $D_{p,wt}$ and $\rho_{p,wt}$ should be initially chosen (as a first choice for the second set of particles, which must be erodible) and $u^*_{t,wt}$ should be calculated to verify if $u^* > u^*_{t,wt}$ (erodible particles), if it is not, the chosen particles must be reevaluated. Then, analogously to the set of non-erodible particles, now, the Stokes number should be calculated for both scales and compared to the critical Stokes number. Let us assume that the critical Stokes is equal to unity. Therefore, for the purpose of the present work, if Stokes in the real scenario is larger than one, then Stokes in the wind tunnel must also be larger than one so to reach similarity. And for that to be achieved appropriate values of $D_{p,wt}$, $\rho_{p,wt}$ and U_{wt} must be found. If $\eta >> D_p$ and $St_l < 1$, the mode of transportation is suspension. If $St_L > 1$, the mode of transportation is saltation. If $C_{tp} > 1$, the particle is in saltation or modified saltation mode. If $C_{tp} < 1$, the particle is in suspension or modified suspension mode.

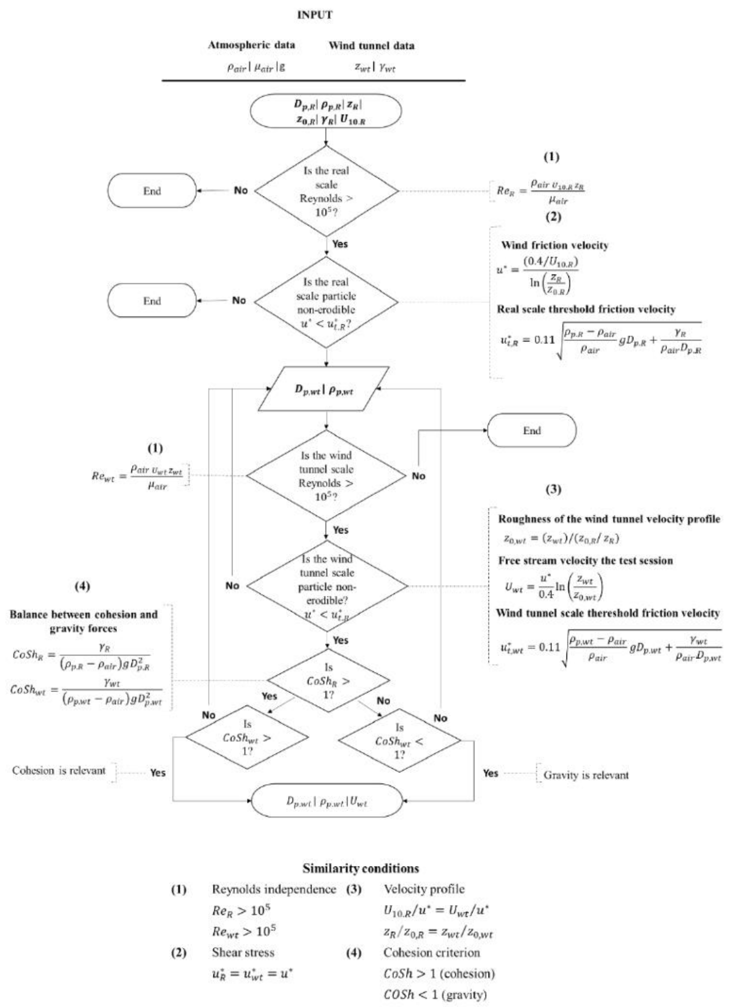

Figure 3. Flowchart of the methodology applied to non-erodible cases.

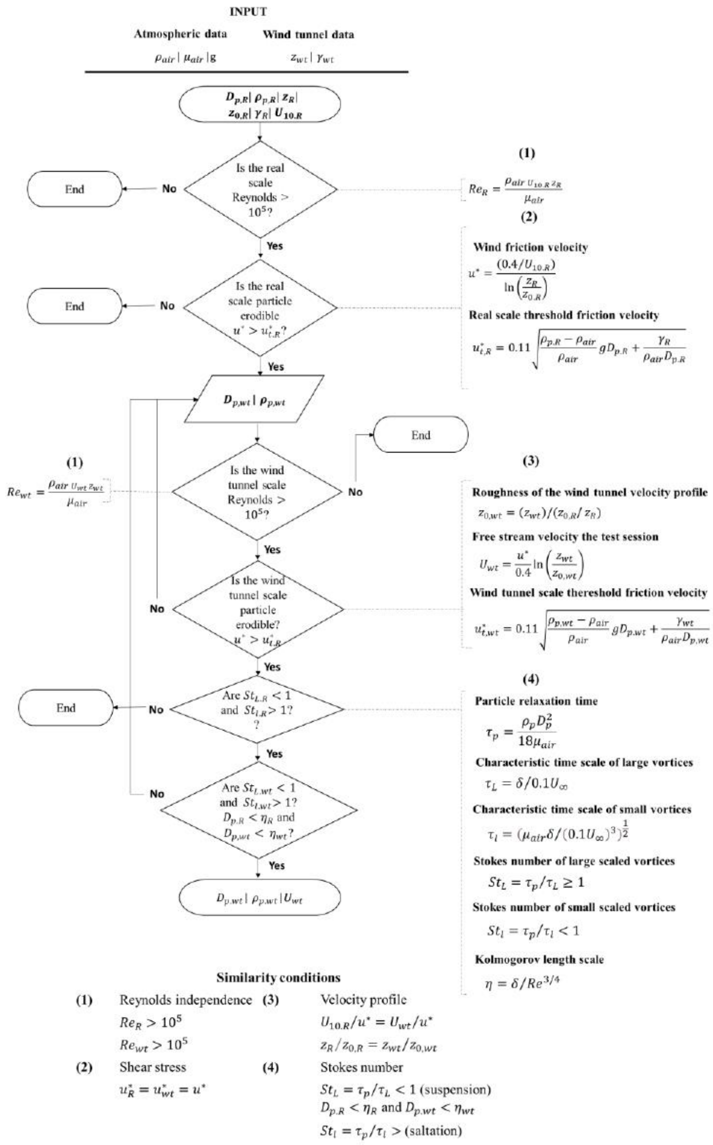

Figure 4. Flowchart of the methodology applied to erodible cases.

3.1 The hypothetical real case scenario and the wind tunnel experimental configuration

Then, let us consider in the hypothetical real scenario of a bed containing a mixture of iron ore particles of different diameters (2.5, 10, 30, 100 and 250 μm) exposed to an upwind flowing over sea surface ($z_{0,R} = 0.001\ m$) to apply the methodology proposed in the present work. **Table 1** presents iron ore particles and air flow properties taken here as the hypothetical real case scenario. **Table 2** presents the parameters used to determine erodibility and mode of transport according to particles diameter and the information presented in **Table 1**.

Let us assume that there is an existing wind tunnel for the experiments that has a cross sectional area 0.80 m height, thus, the height where the free stream velocity can be measured in the wind tunnel is $z_{wt} = 0.40\ m$ which is half the height of the wind tunnel test section (reference height). If the wind tunnel is still under planning or construction, it would add another degree of freedom. As discussed in Section 2.1, to guarantee the boundary layer similarity, we can set the same wind velocity and friction velocity in both scales and imposes a roughness in the wind tunnel given by Equation (1).

Table 1. Particles and fluid flow properties for a hypothetical real case scenario (iron ore).

Particles density ($\rho_{p,R}$)	5,350 kg/m^3	Von Karman constant	0.40
Particles surface energy ($\gamma_{p,R}$)	1.65×10^{-4} kg/s^2	Reference height (z_R)	10.00 m
Air density (ρ_{air})	1.22 kg/m^3	Roughness length (m)	1.00×10^{-4} m
Gravity (g)	9.81 m/s^2	Friction velocity (m/s)	0.28 m/s
Air viscosity (μ_{air})	1.75×10^{-5} $Pa\ s$	Reynolds number (Re_R)	2.80×10^8
Boundary layer height (δ_R)	500 m	Time scale for larger eddies ($\tau_{R,L}$)	625 s
Free stream velocity (U_R)	8.00 m/s	Kolmogorov time scale ($\tau_{R,l}$)	0.13 s
A_N constant	0.11	Kolmogorov length scale (η_R)	2.31×10^{-4} m

Table 2. Parameters used to determine erodibility and mode of transport according to particles diameter considered in the hypothetical real case scenario.

Particles diameter ($D_{p,R}$)	2.5 μm	10 μm	30 μm	100 μm	250 μm
Threshold friction velocity ($u^*_{t,R}$)	0.81 m/s	0.41 m/s	0.26 m/s	0.26 m/s	0.37 m/s
Erodibility	**Non-Erodible**	**Non-Erodible**	**Erodible**	**Erodible**	**Non-Erodible**
CoSh	503.13	31.45			0.05
Particle relaxation time ($\tau_{p,R}$)			1.53×10^{-2} s	1.70×10^{-1} s	
Particle free fall velocity ($V_{gp,R}$)			0.15 m/s	1.67 m/s	
St_L			2.00×10^{-5}	3.00×10^{-4}	
			Suspension	**Suspension**	
St_l			0.12	1.30	
			Supension	**Saltation**	
Kolmogorov lenght scale (η_R)			2.31×10^{-4} m	2.31×10^{-4} m	
			Suspension	**Suspension**	
Crossing trajectory parameter ($V_{gp,R}/u^*_{t,R}$)			0.57	6.38	
			Suspenstion or modified suspension	**Saltation or modified saltation**	

Figure 5 shows the possible wind tunnel scenarios (ρ_{wt} and $D_{p,wt}$) that could represent the investigated real scenario. The set of density and diameter (ρ_{wt} and $D_{p,wt}$) of possible cases that could be representative of the real scenario occupies the area on the left side of curve for particles diameter of $D_{p,R} = 2.5\ \mu m$ and $D_{p,R} = 10\ \mu m$ (**Figure 5a**), the area on the right side of curve for particles diameter of $D_{p,R} = 250\ \mu m$ (**Figure 5b**), the area between the two curves for particles diameter of $D_{p,R} = 30\ \mu m$ (**Figure 5c**), and the area on the right side of curve for particles diameter of $D_{p,R} = 100\ \mu m$ (**Figure 5d**). Therefore, if it is assumed that any $CoSh$ value larger than unity is enough to indicate that cohesion is the effect responsible for the non-erodibility, then any combination of ρ_{wt} and $D_{p,wt}$ chosen from the inside of the limited area in **Figure 5a** would guarantee that the cohesion is the relevant force in the wind tunnel experiments. The opposite is also valid. Any $CoSh$ value lower than unity is enough to indicate that gravity is the effect responsible for the non-erodibility, then any combination of ρ_{wt} and $D_{p,wt}$ chosen from the inside of the limited area in **Figure 5b** would guarantee that the gravity is the relevant force in the wind tunnel experiments.

Figure 5c-d show the results for erodible particles in pure or modified suspension (**Figure 5c**) and for erodible particles in pure or modified saltation (**Figure 5d**) according to Stokes number and crossing trajectory parameter (see **Table 2**).

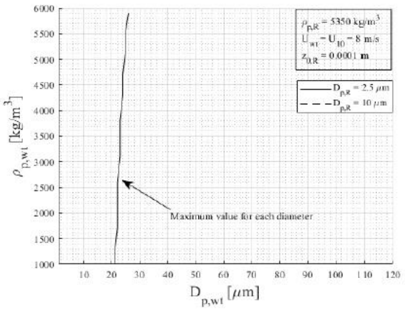

(a)

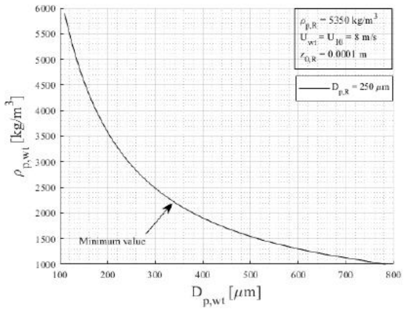

(b)

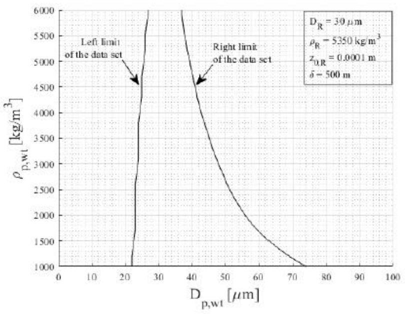

(c)

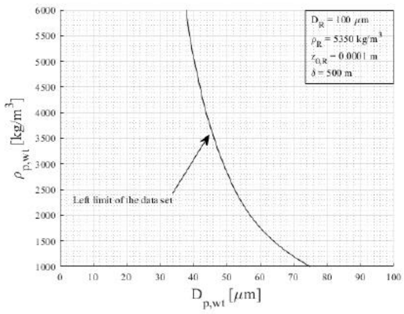

(d)

Figure 5. Possible wind tunnel scenarios (ρ_{wt} and $D_{p,wt}$) that can represent real iron ore (5350 kg/m³) particles of $D_{p.R} = 2.5\ \mu m$, $10\ \mu m$, $30\ \mu m$, $100\ \mu m$, $250\ \mu m$ for flow conditions presented in Table 1. In (a) particles with diameters of $D_{p,R} = 2.5\ \mu m$ and $D_{p,R} = 10\ \mu m$ are non-erodible by cohesion ($CoSh > 1$). In (b) particles with diameters of $D_{p,R} = 250\ \mu m$ are non-erodible by gravity ($CoSh < 1$). In (c) erodible particles are in suspension or modified suspension. In (d) erodible particles are in saltation or modified saltation.

Table 3 summarizes similarity analysis for the real case study (shown in **Tables 1** and **2**) and present suggestion of similar diameter and density set for wind tunnel simulation set up. For erodible particle of $30\ \mu m$, $St_{l,R} < 1$ indicates pure suspension, as well as $St_{L,R} < 1$. In addition, the crossing trajectory parameter $V_g/u^* < 1$ indicates pure or modified suspension. From results obtained from **Figure 5c**, similar diameter in the wind tunnel could vary in a range of 25-40 μm and similar density could vary in a range of 1000-4000 kg/m^3, for instance. For erodible particle of $100\ \mu m$, $St_{l,R} > 1$ indicates pure saltation, but $St_{L,R} < 1$ indicates pure suspension. One way to get around this discrepancy is to consider what the crossing trajectory parameter indicates. For particles diameter of $100\ \mu m$, $V_g/u^* > 1$ indicates pure or modified saltation. Thus, as an approximation, it is considered that particles with this diameter under the conditions already mentioned perform pure or modified saltation, which is also presented in

Table 2. From results obtained from **Figure 5c**, similar diameter in the wind tunnel could vary in a range of 55-100 μm and similar density could vary in a range of 2500-6000 kg/m^3, for instance.

Table 3. Summary of similarity analysis for the case study (shown in Tables 1 and 2) and suggestion of a representative range of diameter and density for wind tunnel simulation design.

$D_{p,R}$ $[\mu m]$	Erod.	$CoSh_R$	$St_{l,R}$	$St_{L,R}$	$\frac{V_g}{u_t^*}$	Possible wind tunnel scenarios $D_{p,wt}$ $[\mu m]$	$\rho_{p,wt}$ $[kg/m^3]$
2.5	NEP	503.13	-	-	-	1-20	1000-6000
10	NEP	31.45	-	-	-	1-20	1000-6000
30	EP	-	0.12	0.00002	0.57	25-40	1000-4000
100	EP	-	1.30	0.0003	6.38	55-100	2500-6000
250	NEP	0.05	-	-	-	300-800	2500-6000

3.2 Influence of wind flow velocity on possible non-erodible wind tunnel scenarios

It is important to highlight that the proposed hypothetical real scenario investigated in case study assumes the free stream velocity equal to 8 m/s. However, there is an influence of wind flow velocity on the possible wind tunnel scenarios that could represent the real one. **Figure 6a-b** show that for non-erodible cases by cohesion ($D_{p,R} = 2.5\ \mu m$ and $D_{p,R} = 10\ \mu m$), as wind flow velocity increases the number of possible wind tunnel scenarios that could represent the proposed hypothetical real scenario, decrease. This happens because increasing the free stream velocity increases the magnitude of aerodynamic forces in relation to cohesive ones, causing emission of previously non-erodible particles. **Figure 6c** show that for erodible cases by gravity ($D_{p,R} = 250\ \mu m$), as wind flow velocity increases the number of possible wind tunnel scenarios that could represent the proposed hypothetical real scenario, increase. Increasing free stream velocity increases the magnitude of aerodynamic forces in relation to gravity forces. However, this increase in the number of possible cases in the wind tunnel according to the increase in free stream velocity is accompanied by an increase in particle diameter and density.

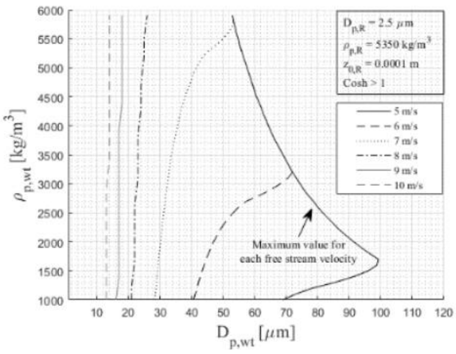

(a)

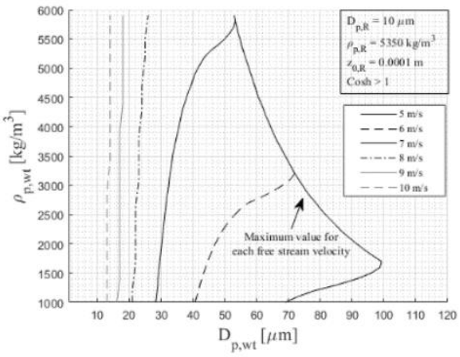

(b)

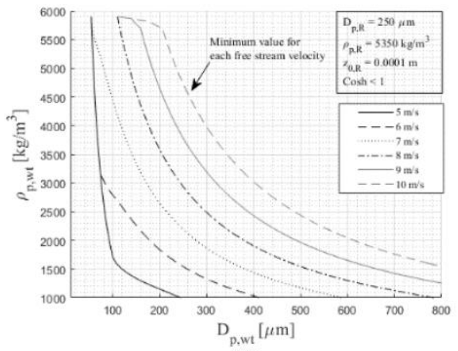

(c)

Figure 6. Possible wind tunnel scenarios that could represent the proposed hypothetical real scale scenario considering different stream flow velocities for non-erodible cases by cohesion (a) $D_{p,R}$= 2.5 μm , (b) $D_{p,R}$= 10 μm and, and non-erodible case by gravity (c) $D_{p,R}$= 250 μm .

3.3 Influence of upper and lower limits of $Cosh$ on possible non-erodible wind tunnel scenarios

Figure 7a-b show that if it is assumed that the $CoSh$ number is not equal to unity, then, the possible wind tunnel scenarios that could represent the proposed hypothetical non-erodible real scenario by cohesion ($D_{p,R}$= 2.5 μm and $D_{p,R}$ = 10 μm) would decrease as the $CoSh$ upper limit increases. In addition, **Figure 7c** shows that the possible wind tunnel scenarios that could represent the proposed hypothetical non-erodible real scenario by gravity ($D_{p,R}$= 250 μm) would decrease as the $CoSh$ lower limit increases.

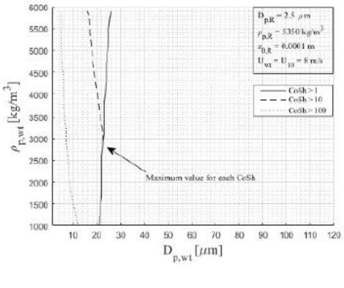

(a)

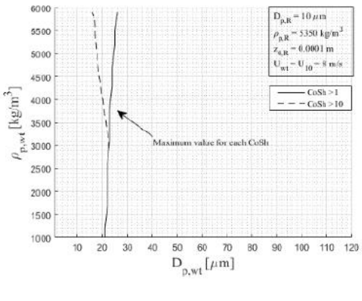

(b)

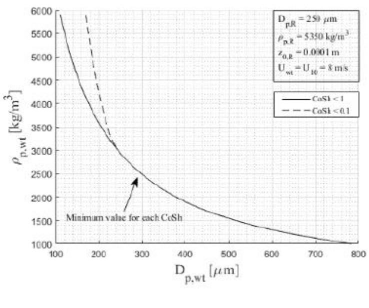

(c)

Figure 7. Possible wind tunnel scenarios that could represent the proposed hypothetical real scale scenario considering different $CoSh$ upper limits for non-erodible cases by cohesion (a) $D_{p,R}$= $2.5\ \mu m$, (b) $D_{p,R}\ =\ 10\ \mu m$ and, different $CoSh$ lower limits for non-erodible case by gravity (c) $D_{p,R}$= $250\ \mu m$.

4 Discussions and conclusions

The experimental simulation of aeolian erosion can become technically emblematic as particles size has to be reduced to suit the wind tunnel scale. This reduction in particle size may result in the emergence of cohesion effects which may not be occurring in the real scale. In addition, the experimental simulation must be designed using particles with commercially available diameters. Therefore, it is necessary to evaluate the similarity between wind tunnels and real scale particle beds to overcome the particle size limitation. The well know similarity criteria for the simulation of atmospheric boundary layer (Reynolds independence, wind shear stress and vertical velocity profile conservation) are taken into account as well as other criteria to guarantee that the effect responsible for erodibility and the mode of particles transportation are the similar in both scales.

From the application of Buckingham similarity theory, a dimensionless number arose for non-erodible, the $CoSh$ number. For erodible particles, dimensionless Stokes numbers was applied. $CoSh$ number evaluates the reason why non-erodible particles resist to the wind shear stress, if they stand in the particle bed by gravity or by cohesion effects. If $CoSh \gg 1$, cohesion force strongly influences particles non-erodibility. If $CoSh \ll 1$, gravity is the main force on particles non-erodibility. In turn, Stokes number evaluates what kind of movement the erodible particles will perform after being emitted based on the interaction between them and the turbulent vortices. The particle relaxation time τ_p is compared to the small-time scales τ_l and large time scales τ_L. Particles that satisfy $St_L = \tau_p/\tau_L << 1$ are weightless and small enough to be driven by the turbulent flow in suspension. In opposition, saltation is observed for particles whose behavior is not influenced by turbulence effects but is governed by inertia, gravity, and particle-wall collision phenomena. Such particles are characterized by $St_l = \tau_p/\tau_l >> 1$.

For the non-erodible scenario, the sensitivity of the possible wind tunnel cases representative of the real ones was tested to evaluate the increase in the $CoSh$ number by three orders of magnitude ($CoSh > 1$, $CoSh > 10$, and $CoSh > 100$), decrease in the $CoSh$ number by three orders of magnitude ($CoSh < 1$, $CoSh < 0.1$, and $CoSh < 0.01$), and increase of free stream velocities six times (5, 6, 7, 8, 9, and 10 m/s). The influence of free stream velocity on particle erodibility is evident. As the free stream velocity increases, non-erodible particles tend to become erodible, resulting in fewer possible wind tunnel scenarios. For erodible particles, the increase in the number of possible cases in the wind tunnel due to the increase in free stream velocity is accompanied by an increase in particle diameter and density, leading to more possible wind tunnel scenarios.

The increase in $CoSh$ number highlights the increased influence of the cohesion force on particles non-erodibility. This also leads to a reduction in possible wind tunnel cases since the similarity criterion becomes increasingly restrictive. As it is not possible to say what is much greater than 1, is reasonable to establish that a moderate $CoSh$ (> 10), it may be the best choice, since $CoSh > 1$ is very close to 1, which can lead to cases with significant influence of gravity and $CoSh > 100$ is a very rigid value that can guarantee non-erodibility due to cohesion, but can limit the execution of experiments. For real particles with diameter of 10 μm no possible cases were found for $CoSh > 100$.

The decrease in $CoSh$ number highlights the increased influence of the gravity force on the particles non-erodibility. This also leads to a reduction in possible wind tunnel cases since the similarity criterion becomes increasingly restrictive. It is also reasonable to establish a moderate $CoSh$ (< 0.1), that may be the best choice in the similarity analysis since $CoSh < 1$ is very close to 1, which can lead to cases with significant influence of cohesion, and $CoSh < 0.01$ did not result in any possible cases for particles with 250 μm.

But even so, in cases where gravity is the major responsible for particles non-erodibility, the restriction is much more flexible than the restriction for cases dominated by cohesion. Experiments for these cases are easier to design due larger particles size.

It is important to highlight that kinematic similarity was considered when the velocity profile was equalized in both scales. Dynamic similarity was considered in dimensionless numbers that are essentially a balance between forces. The difficulties in obtaining geometric similarity were overcame by assuming that equality of physical principles governing the erodibility of particles and their respective movement were achieved.

5 References

Alfaro, S.C. *et al.* (1997) 'Modeling the size distribution of a soil aerosol produced by sandblasting', *J Geophys Res*, 102(11), pp. 239–249.

Aliabadi, A.A. (2018) *Theory and applications of turbulence*. Amir A. Aliabadi Publications.

Anno, Y. (1984) 'Requirements for modeling of a snowdrift', *Cold Regions Science and Technology*, 8(3), pp. 241–252. Available at: https://doi.org/10.1016/0165-232X(84)90055-7.

Bagnold, R.A. (1941) 'An aprroach to the sediment transport problem from general physics', *Physiographic and Hidraulic studies of rivers* [Preprint].

Bagnold, R A (1941) *The physics of blown sand and desert dunes*. Reprint. Methuen, London.

Balachandar, S. (2009) 'A scaling analysis for point-particle approaches to turbulent multiphase flows', *International Journal of Multiphase Flow*, 35(9), pp. 801–810. Available at: https://doi.org/10.1016/j.ijmultiphaseflow.2009.02.013.

Berk, T. and Coletti, F. (2020) 'Transport of inertial particles in high-Reynolds-number turbulent boundary layers', *Journal of Fluid Mechanics* [Preprint]. Available at: https://doi.org/10.1017/jfm.2020.597.

Burke, J.P. (1982) *A wind-tunnel study of low speed turbulent boundary layer flow over a rough-to-smooth transition with and without vortex generators (spires)*. University of California, Davis.

Burr, D.M. *et al.* (2020) 'A wind tunnel study of the effect of intermediate density ratio on saltation threshold', *Aeolian Research*, 45(August 2019), p. 100601. Available at: https://doi.org/10.1016/j.aeolia.2020.100601.

Chew, L.W., Aliabadi, A.A. and Norford, L.K. (2018) 'Flows across high aspect ratio street canyons: Reynolds number independence revisited', *Environmental Fluid Mechanics*, 18(5), pp. 1275–1291. Available at: https://doi.org/10.1007/s10652-018-9601-0.

Clayton, J. (2019a) *An Introduction to Powder Characterization*, *Handbook of Pharmaceutical Wet Granulation*. Elsevier Inc. Available at: https://doi.org/10.1016/b978-0-12-810460-6.00021-x.

Clayton, J. (2019b) *An Introduction to Powder Characterization*, *Handbook of Pharmaceutical Wet Granulation*. Elsevier Inc. Available at: https://doi.org/10.1016/b978-0-12-810460-6.00021-x.

Iversen, J.D. (1980) 'Drifting-Snow Similitude—Transport-Rate and Roughness Modeling', *Journal of Glaciology*, 26(94), pp. 393–403. Available at: https://doi.org/10.1017/s0022143000010923.

Jiang, C.W. *et al.* (2022) 'Wind-tunnel experiments of Aeolian sand transport reveal a bimodal probability distribution function for the particle lift-off velocities', *Catena*, 217(February), p. 106496. Available at: https://doi.org/10.1016/j.catena.2022.106496.

Kato, M. and Hanafusa, T. (1996) 'Wind tunnel simulation of atmospheric turbulent flow over a flat terrain', *Atmospheric Environment*, 30(16), pp. 2853–2858.

Kind, R.J. (1976) 'A critical examination of the requirements for model simulation of wind-induced erosion/deposition phenomena such as snow drifting', *Atmospheric Environment (1967)*, 10(3), pp. 219–227. Available at: https://doi.org/10.1016/0004-6981(76)90094-9.

Kok, J. and Renno, N. (2009) 'A comprehensive numerical model of steady state saltation (COMSALT)', *Journal of Geophysical Research Atmospheres*, 114(17), pp. 1–20. Available at: https://doi.org/10.1029/2009JD011702.

Kok, L. *et al.* (2012) 'The physics of wind-blown sand and dust', *Reports on Progress in Physics*, 75(10), p. 106901.

Loosmore, G.A. and Hunt, J.R. (2000) 'Below-threshold, non-abraded dust resuspension', *J Geophys Res*, 105(20), p. ,663–20.

Marshall, J., Fenton, L.K. and Harlow, J.J.B. (2021) 'Limitations of applying grain weight similitude in aeolian studies with NASA Mars Wind Tunnel', *Aeolian Research*, 53(August), p. 100732. Available at: https://doi.org/10.1016/j.aeolia.2021.100732.

Mina, M. *et al.* (2022) 'Predicting wind erosion rate using portable wind tunnel combined with machine learning algorithms in calcareous soils, southern Iran', *Journal of Environmental Management*, 304(November 2021), p. 114171. Available at: https://doi.org/10.1016/j.jenvman.2021.114171.

Oujia, T., Matsuda, K. and Schneider, K. (2020) 'Divergence and convergence of inertial particles in high-Reynolds-number turbulence', *Journal of Fluid Mechanics*, 905. Available at: https://doi.org/10.1017/jfm.2020.672.

Raffaele, L., van Beeck, J. and Bruno, L. (2021) 'Wind-sand tunnel testing of surface-mounted obstacles: Similarity requirements and a case study on a Sand Mitigation Measure', *Journal of Wind Engineering and Industrial Aerodynamics*, 214, p. 104653. Available at: https://doi.org/10.1016/j.jweia.2021.104653.

Shao, Y. (2008) *Physics and modelling of wind erosion*. 2nd edn. Springer.

Shao, Yaping (2008) *Physics and modelling of wind erosion*. 2nd edn. Cologne: Springer.

Shao, Y. and Klose, M. (2016) 'A note on the stochastic nature of particle cohesive force and implications to threshold friction velocity for aerodynamic dust entrainment', *Aeolian Research*, 22, pp. 123–125. Available at: https://doi.org/10.1016/j.aeolia.2016.08.004.

Shao, Yaping and Lu, H. (2000) 'A simple expression for wind erosion threshold friction velocity', *Journal of Geophysical Research*, 105, pp. 22437–22443. Available at: https://doi.org/https://doi.org/10.1029/2000JD900304.

Shao, Y. and Lu, H. (2000) 'A simple expression for wind erosion threshold friction velocity', *Journal of Geophysical Research*, 105, pp. 437–443.

Shao, Y., Raupach, M.R. and Findlater, P.A. (1993) ‘On the Entrainment of Dust by Wind’, *Journal of Geophysical Research*, 98(D7), pp. 12719–12726.

Sherman, D.J. (2020) ‘Understanding wind-blown sand: Six vexations’, *Geomorphology*, 366, p. 107193. Available at: https://doi.org/10.1016/j.geomorph.2020.107193.

Shields, A. (1936) *Application of similarity principles and turbulence research to bed-load movement*.

Snyder, W.H. (1972) ‘Similarity criteria for the application of fluid models to the study of air pollution meteorology’, *Boundary-Layer Meteorology*, 3(1), pp. 113–134. Available at: https://doi.org/10.1007/BF00769111.

Strom, G.H. *et al.* (1962) *Scale model studies on snow drifting*. Virginia.

Tanière, A., Oesterlé, B. and Monnier, J.C. (1997) ‘On the behaviour of solid particles in a horizontal boundary layer with turbulence and saltation effects’, *Experiments in Fluids*, 23(6), pp. 463–471. Available at: https://doi.org/10.1007/s003480050136.

Theodoor, J. and Overbeek, G. (1985) *Modern Trends in Colloid Science in Chemistry and Biology*, *Birth, life and death of colloids*. Edited by H.F. Eicke. Berlin: Springer.

White, B.R. (1996a) ‘Laboratory simulation of aeolian sand transport and physical modelling’, *Annals of Arid Zone*, 35(3), pp. 187–213.

White, B.R. (1996b) ‘Laboratory simulation of aeolian sand transport and physical modelling’, *Annals of Arid Zone*, 35(3), pp. 187–213.

Woodruff, N.P. and Zingg, A.W. (1953) ‘Wind tunnel studies of shelter belt models’, *J. Forestry*, 51, p. 173.

Zhang, J. *et al.* (2022) ‘Impact of turbulence on aeolian particle entrainment: results from wind-tunnel experiments’, *Atmospheric Chemistry and Physics*, 22(14), pp. 9525–9535. Available at: https://doi.org/10.5194/acp-22-9525-2022.

7. CONCLUSION AND RECOMMENDATIONS FOR FUTURE WORKS

The main issues addressed in the present thesis consisted in (*i*) investigating the impact of multiple stockpiles configuration on particles re-emission from its surroundings due to wind erosion, (*ii*) assessing the influence of non-erodible particles on the development of fluid flow structures responsible for the entrainment of erodible particles, comprehending the primary effects of particle bed configurations on the evolution of the aerodynamic probability density function distribution and on the mathematical modeling of wind erosion phenomena, and (*iii*) evaluating the similarity requirements of wind flow, particle entrainment, and particle transport in wind tunnel experiments discussing about a representative simulation of real-scale scenarios.

The influence of multiple stockpiles on total particles re-emission revealed that increasing wind velocity (from 5 to 15 m/s), the erodible areas surrounding the piles and the erodible area on the pile increases as well as the emission of particles on these areas. For the configuration of pile orientation 60° and 90° to the incoming flow, respectively, highest, and lowest values of re-emitted particles on the surrounding areas were found for all tested configurations. On the other hand, the gap between piles did not show a significant influence on the total particle's emission. This result is extremely important for industries that store particulate matter in open yards, as it provides valuable insights into how different factors influence particle re-emission. Understanding how increasing wind velocity increases particle emissions can help in adopting preventive measures. For example, knowing that specific orientations of the piles relative to the wind flow, such as 60° and 90°, result in different levels of re-emission, industries can optimize the orientation of the piles to minimize particle emission. Additionally, the finding can help the management of yard layouts, allowing industries to focus on controlling wind velocities by wind fences implementations, for instance, or moving storage yards to areas with low probability of erosion. This knowledge can lead to the implementation of more effective strategies to reduce air pollution and improve occupational health and safety in industries.

In addition to the importance of non-local evaluation of the main variables influencing the wind erosion, the present thesis performed simulations to investigate how non-erodible particles modify the airflow (local turbulence) and the potential of particles emission (erodibility). The presence of non-erodible particles on the development of fluid flow structures responsible for the entrainment of erodible particles was accessed using LES, highlighting the differences in the turbulent structures developed on smooth and rough surfaces. On the rough bed, it was possible to observe the ejection and sweep motions for most part of time.

Probability density functions that best represent the friction velocity on smooth and rough walls were investigated, aiming to give support to the improvement of emission models based on probabilistic approach. The analysis of the friction velocity probability density function for both smooth and rough beds indicates that the Gamma distribution provides a suitable model. For the smooth wall, the Gamma distribution with a mean of 2.46 and a mean of 0.06 shows good agreement, as validated by the NMSE criterion. Similarly, for the rough surface, the Gamma distribution with a mean of 2.6 and a mean of 0.05 also demonstrates a good fit according to the NMSE criterion. These findings underscore the ability of the Gamma distribution in accurately describing the friction velocity probability density function for varying surface conditions.

Similarity requirements of wind flow, particle entrainment and particle transport on wind tunnel experiments aiming for a representative simulation of real scale scenarios were discussed. By identifying dimensionless numbers and the main forces involved in particle entrainment and transport, the study provides a framework for understanding how variables such as particle diameter, particle density, fluid density, wind velocity, and bed configurations influence particle behavior in both reduced (wind-tunnel) and full-scale (atmosphere) scenarios. The analysis discusses the significance of the $CoSh$ and Stokes numbers in assessing the similarity between erodible and non-erodible particles. Evaluating the critical $CoSh$ number is essential for predicting the thresholds at which gravity or cohesion forces prevail over particle non-erodibility. The Stokes number reveals that ensuring similarity in particle movement between real and wind tunnel scales becomes increasingly challenging as particle size decreases. Further investigation into the underlying physics of this phenomenon is necessary to enhance our understanding and predictive capabilities.

Recommendations for future work include:

- Numerical simulation of wind flow over rough beds using LES for different proportions and shapes of rough elements.
- Improving the understanding of PDFs for generalization of rough surface (different non-erodible elements distribution) by using multivariate analysis to describe the relationship between the PDFs obtained in different relative positions in relation to the rough elements.
- Carrying out experimental campaigns to obtain data to validate the numerical simulations proposed above. Experimental work should be conducted on a flat plate

with rough elements of different shapes and proportions using sand in the empty spaces in order to evaluate the movement of particles and subsequent comparison with numerical simulation results to evaluate the relationship between the vertical movement of coherent structures and particles emission.

- Carrying out experimental campaigns to analyze the non-dimensional parameters and their relationship obtained in this work to help achieving similarity for wind tunnel experiments concerning wind erosion of small particles of air pollution interest.
- Measuring the particle surface energy parameter for diverse materials in order to estimate the importance of the cohesion force for small particles of air pollution interest.

REFERENCES

Alfaro, S.C., Gaudichet, A., Gomes, L., Maille, M., 1997. Modeling the size distribution of a soil aerosol produced by sandblasting. J Geophys Res 102, 239–249.

Aliabadi, A.A., 2018. Theory and applications of turbulence. Amir A. Aliabadi Publications.

Amtonopoulos-Domis, 1981. Large-Eddy simulation of a passive scalar in isotropic turbulence. J. Fluid Mechanics 104, 55–79.

An, Z., Jin, Y., Li, J., Li, W., Wu, W., 2018. Particulate Matter. Curr Allergy Asthma Rep 18, 3–9. https://doi.org/https://doi.org/10.1007/s11882-018-0768-8

Anno, Y., 1984. Requirements for modeling of a snowdrift. Cold Reg Sci Technol 8, 241–252. https://doi.org/10.1016/0165-232X(84)90055-7

Antonia, R.A., 1977. Similarity of atmospheric Reynolds shear stress and heat flux fluctuations over a rough surface. Boundary Layer Meteorology 12, 351–364.

Badr, T, Harion, J.-L., 2007. Quantification of diffuse dust emissions from open air sources on industrial sites. 3rd IASME/WSEAS International Conference on Energy, Environment and Sustainable Development (EEESD ’07), ISBN: 978-960-8457-88-1 276–280.

Badr, T., Harion, J.L., 2007. Effect of aggregate storage piles configuration on dust emissions. Atmos Environ 41, 360–368. https://doi.org/10.1016/j.atmosenv.2006.07.038

Badr, T., Harion, J.L., 2005. Numerical modelling of flow over stockpiles: Implications on dust emissions. Atmos Environ 39, 5576–5584. https://doi.org/10.1016/j.atmosenv.2005.05.053

Bagnold, R.A., 1941. An aprroach to the sediment transport problem from general physics. Physiographic and Hidraulic studies of rivers.

Bagnold, R A, 1941. The physics of blown sand and desert dunes, Reprint. ed. Methuen, London.

Baitimerov, R., Lykov, P., Zherebtsov, D., Radionova, L., Shultc, A., Prashanth, K.G., 2018. Influence of powder characteristics on processability of AlSi12 alloy fabricated by selective laser melting. Materials 11. https://doi.org/10.3390/ma11050742

Boussenesq, J., 1877. Theorie de lecoulement tourbillant. Mem. Acad. Sci 23, 1–680.

Bové, H., Bongaerts, E., Slenders, E., Bijnens, E.M., Saenen, N.D., Gyselaers, W., Van Eyken, P., Plusquin, M., Roeffaers, M.B.J., Ameloot, M., Nawrot, T.S., 2019. Ambient black carbon particles reach the fetal side of human placenta. Nat Commun 10, 1–7. https://doi.org/10.1038/s41467-019-11654-3

Brown, S., Nickling, W.G., Gillies, J.A., 2008. A wind tunnel examination of shear stress partitioning for an assortment of surface roughness distributions. J Geophys Res Earth Surf 113. https://doi.org/10.1029/2007JF000790

Caliman, M.C.F.S., 2017. Influence de particules dans le processus d'érosion éolienne. Université de Rennes.

Cheng, N.S., 2006. Influence of shear stress fluctuation on bed particle mobility. Physics of Fluids 18. https://doi.org/10.1063/1.2354434

Cheng, N.S., Sumer, B.M., Fredsøe, J., 2003. Investigation of bed shear stresses subject to external turbulence. Int J Heat Fluid Flow 24, 816–824. https://doi.org/10.1016/S0142-727X(03)00088-2

Cheng, N.S., Tang, H., Zhu, L., 2004. Evaluation of bed load transport subject to high shear stress fluctuations. Water Resour Res 40. https://doi.org/10.1029/2003WR003001

Cheng, N.-S., Wing-Keung Law, A., n.d. Fluctuations of Turbulent Bed Shear Stress. https://doi.org/10.1061/ASCE0733-93992003129:1126

Chew, L.W., Aliabadi, A.A., Norford, L.K., 2018. Flows across high aspect ratio street canyons: Reynolds number independence revisited. Environmental Fluid Mechanics 18, 1275–1291. https://doi.org/10.1007/s10652-018-9601-0

Clark, R.A., Ferzinger, J.H., Reynolds, W.C., 1979. Evaluation of subgrid-scale models using and accurately simulated turbulent flow. J. Fluid Mech 91, 1–6.

Clayton, J., 2019. An Introduction to Powder Characterization, Handbook of Pharmaceutical Wet Granulation. Elsevier Inc. https://doi.org/10.1016/b978-0-12-810460-6.00021-x

Colella, K.J., Keith, W.L., 2003. Measurements and scaling of wall. Exp Fluids 34, 253–260.

Crawley, D.M., Nickling, W.G., 2003. Drag partition for regularly-arrayed rough surfaces. Boundary Layer Meteorol 107, 445–468. https://doi.org/10.1023/A:1022119909546

Davidson, P.A., 2015. Turbulence: an intrduction for scientists and engineers, 2nd ed. Oxford University Press, New York.

De Morais, C.L., Ferreira, M.C.S., Santos, J.M., Furieri, B., Harion, J.L., 2018. Influence of non-erodible particles with multimodal size distribution on aeolian erosion of storage piles of granular materials. Environmental Fluid Mechanics. https://doi.org/10.1007/s10652-018-9640-6

de Morais, C.L., Ferreira, M.C.S., Santos, J.M., Furieri, B., Harion, J.L., 2018. Influence of non-erodible particles with multimodal size distribution on aeolian erosion of storage piles of granular materials. Environmental Fluid Mechanics. https://doi.org/10.1007/s10652-018-9640-6

Deardorff, J.W., 1970a. A numerical study of three-dimensional turbulent channel flow at large Reynolds numbers. J Fluid Mech 41, 453–480. https://doi.org/10.1017/S0022112070000691

Deardorff, J.W., 1970b. A numerical study of three-dimensional turbulent channel flow at large Reynolds numbers. J Fluid Mech 41, 453–480. https://doi.org/10.1017/S0022112070000691

Dentoni, V., Grosso, B., Pinna, F., Lai, A., Bouarour, O., 2022. Emission of Fine Dust from Open Storage of Industrial Materials Exposed to Wind Erosion. Atmosphere (Basel) 13. https://doi.org/10.3390/atmos13020320

Derakhshani, S.M., Schott, D.L., Lodewijks, G., 2013. Dust emission modelling around a stockpile by using computational fluid dynamics and discrete element method. AIP Conf Proc 1542, 1055–1058. https://doi.org/10.1063/1.4812116

Descamps, I., Harion, J.L., Baudoin, B., 2005a. Taking-off model of particles with a wide size distribution. Chemical Engineering and Processing: Process Intensification 44, 159–166. https://doi.org/10.1016/j.cep.2004.04.007

Descamps, I., Harion, J.L., Baudoin, B., 2005b. Taking-off model of particles with a wide size distribution. Chemical Engineering and Processing: Process Intensification 44, 159–166. https://doi.org/10.1016/j.cep.2004.04.007

Desreumaux, O., Bourez, J.P., 1989. Préparation de bouillies pour visualisation pariétales sur maquette de sous-marin à cepra 19. France.

Diego, I., Pelegry, A., Torno, S., Toraño, J., Menendez, M., 2009. Simultaneous CFD evaluation of wind flow and dust emission in open storage piles. Appl Math Model 33, 3197–3207. https://doi.org/10.1016/j.apm.2008.10.037

Dreeben, T.D., Pope, S.B., 1997. Probability density function and Reynolds-stress modeling of near-wall turbulent flows. Physics of Fluids 9, 154–163. https://doi.org/10.1063/1.869157

Duran, J., 2000. Sands, powder, and grains : an introduction to the physics of granular materials, Teaching History. Springer-Verlag New York. https://doi.org/10.1007/978-1-4612-0499-2

Durst, F., Jovanovic, J., Kanevce, L., 1987. Durst et al (1987) - Probability density distribution in turbulent wall, in: Turbulent Shear Flows 5: Selected Papers from the Fifth International Symposium on Turbulent Shear Flows, Cornell University, Ithaca, New York, USA, August 7–9, 1985. Springer Berlin Heidelberg, Berlin, pp. 197–220.

Farmer, A.M., 1993. The effects of dust on vegetation - a review. Environmental Pollution 79, 63–75.

Ferreira, A.D., Pinheiro, S.R., Francisco, S.C., 2013. Experimental and numerical study on the shear velocity distribution along one or two dunes in tandem. Environmental Fluid Mechanics 13, 557–570. https://doi.org/10.1007/s10652-013-9282-7

Ferreira, M.C.S., Furieri, B., A., O.E.M., Harion, J.L., Valance, A., Dupont, P., Reis, N.C., Santos, J.M., 2019a. A simple model to estimate emission of wind-blown particles from a granular bed in comparison to wind tunnel experiments. Geomorphology 335, 1–13. https://doi.org/10.1016/j.geomorph.2019.03.004

Ferreira, M.C.S., Furieri, B., A., O.E.M., Harion, J.L., Valance, A., Dupont, P., Reis, N.C., Santos, J.M., 2019b. A simple model to estimate emission of wind-blown particles from a granular bed in comparison to wind tunnel experiments. Geomorphology 335, 1–13. https://doi.org/10.1016/j.geomorph.2019.03.004

Ferreira, M.C.S., Furieri, B., A., O.E.M., Harion, J.L., Valance, A., Dupont, P., Reis, N.C., Santos, J.M., 2019c. A simple model to estimate emission of wind-blown particles from a granular bed in comparison to wind tunnel experiments. Geomorphology 335, 1–13. https://doi.org/10.1016/j.geomorph.2019.03.004

Ferreira, M.C.S., Furieri, B., de Morais, C.L., Stocco, J.F., Reis Jr, N.C., Harion, J.-L., Santos, J.M., 2020. Experimental and numerical investigation of building effects on wind erosion of a granular material stockpile. Environmental Science and Pollution Research 27, 14.

Ferreira, M.C.S., Furieri, B., Santos, J.M., El Moctar, A.O., Harion, J.-L., Valance, A., Dupont, P., Reis, N.C., 2019d. An experimental and numerical study of the aeolian erosion of isolated and successive piles. Environmental Fluid Mechanics. https://doi.org/10.1007/s10652-019-09702-z

Ferziger, J.H., 1977. Large Eddy Numerical Simulations of Turbulent Flows. AIAA J 15, 1261–1267.

Findikakis, A., Streeter, R., 1979. An algebraic model for subgrid-scale turbulence in stratified flows. J. Atmos. Sciences 36, 1934–1949.

Foucaut, J.M., Stanislas, M., 1996. Take-off threshold velocity of solid particles lying under a turbulent boundary layer. Exp Fluids 20, 377–382. https://doi.org/10.1007/BF00191019

Furieri, B., 2012a. Erosion éolienne de tas de stockage de matières granulares sur sites industriels: amélioration des méthodes de quantification des émissions. Université de Valenciennes et du Hainaut-Cambrésis.

Furieri, B., 2012b. Erosion éolienne de tas de stockage de matières granulares sur sites industriels: amélioration des méthodes de quantification des émissions. Université de Valenciennes et du Hainaut-Cambrésis.

Furieri, B., Harion, J.L., Milliez, M., Russeil, S., Santos, J.M., 2013a. Numerical modelling of aeolian erosion over a surface with non-uniformly distributed roughness elements. Earth Surf Process Landf 39, 156–166. https://doi.org/10.1002/esp.3435

Furieri, B., Russeil, S., Harion, J.L., Turpin, C., Santos, J.M., 2012. Experimental surface flow visualization and numerical investigation of flow structure around an oblong stockpile. Environmental Fluid Mechanics 12, 533–553. https://doi.org/10.1007/s10652-012-9249-0

Furieri, B., Russeil, S., Santos, J.M., Harion, J.L., 2013b. Effects of non-erodible particles on aeolian erosion: Wind-tunnel simulations of a sand oblong storage pile. Atmos Environ 79, 672–680. https://doi.org/10.1016/j.atmosenv.2013.07.026

Furieri, B., Russeil, S., Santos, J.M., Harion, J.L., 2013c. Effects of non-erodible particles on aeolian erosion: Wind-tunnel simulations of a sand oblong storage pile. Atmos Environ 79, 672–680. https://doi.org/10.1016/j.atmosenv.2013.07.026

Furieri, B., Santos, J.M., Russeil, S., Harion, J.L., 2014. Aeolian erosion of storage piles yards: Contribution of the surrounding areas. Environmental Fluid Mechanics 14, 51–67. https://doi.org/10.1007/s10652-013-9293-4

Gillette, D.A., Stockton, P.H., 1989a. The effect of nonerodible particles on wind erosion of erodible surfaces. Journal of Geophysical Research: Atmospheres 94, 12885–12893. https://doi.org/10.1029/JD094iD10p12885

Gillette, D.A., Stockton, P.H., 1989b. The effect of nonerodible particles on wind erosion of erodible surfaces. Journal of Geophysical Research: Atmospheres 94, 12885–12893. https://doi.org/10.1029/JD094iD10p12885

Gillies, J.A., Green, H., McCarley-Holder, G., Grimm, S., Howard, C., Barbieri, N., Ono, D., Schade, T., 2015. Using solid element roughness to control sand movement: Keeler Dunes, Keeler, California. Aeolian Res 18, 35–46. https://doi.org/10.1016/j.aeolia.2015.05.004

Gillies, J.A., Nickling, W.G., King, J., 2007. Shear stress partitioning in large patches of roughness in the atmospheric inertial sublayer. Boundary Layer Meteorol 122, 367–396. https://doi.org/10.1007/s10546-006-9101-5

Gillies, J.A., Nickling, W.G., King, J., 2006. Aeolian sediment transport through large patches of roughness in the atmospheric inertial sublayer. J Geophys Res Earth Surf 111, 1–13. https://doi.org/10.1029/2005JF000434

Hadley, M.B., Vedanthan, R., Fuster, V., 2018. Air pollution and cardiovascular disease: A window of opportunity. Nat Rev Cardiol 15, 193–194. https://doi.org/10.1038/nrcardio.2017.207

Hofland, B., Battjes, J.A., n.d. Probability Density Function of Instantaneous Drag Forces and Shear Stresses on a Bed. https://doi.org/10.1061/ASCE0733-94292006132:111169

Hoonhout, B.M., Vries, S. de, 2016. A process-based model for aeolian sediment transport and spatiotemporal varying sediment availability. J Geophys Res Earth Surf 121, 1555–1575. https://doi.org/10.1002/2015JF003692

Huang, W., Tan, J., Kan, H., Zhao, N., Song, W., Song, G., Chen, G., Jiang, L., Jiang, C., Chen, R., Chen, B., 2009. Visibility, air quality and daily mortality in Shanghai, China. Science of the Total Environment 407, 3295–3300.

Iversen, J.D., 1980. Drifting-Snow Similitude—Transport-Rate and Roughness Modeling. Journal of Glaciology 26, 393–403. https://doi.org/10.1017/s0022143000010923

Iversen, J.D., Rasmussen, K.R., 1994. The effect of surface slope on saltation threshold. Sedimentology 41, 721–728. https://doi.org/10.1111/j.1365-3091.1994.tb01419.x

Iversen, J.D., Wang, W.P., Rasmussen, K.R., Mikkelsen, H.E., Leach, R.N., 1991a. Roughness element effect on local and universal saltation transport, in: Barndorff-Nielsen, OleE., Willetts, BrianB. (Eds.), Aeolian Grain Transport, Acta Mechanica Supplementum. Springer Vienna, pp. 65–75. https://doi.org/10.1007/978-3-7091-6703-8_5

Iversen, J.D., Wang, W.P., Rasmussen, K.R., Mikkelsen, H.E., Leach, R.N., 1991b. Roughness element effect on local and universal saltation transport, in: Barndorff-Nielsen, OleE., Willetts, BrianB. (Eds.), Aeolian Grain Transport, Acta Mechanica Supplementum. Springer Vienna, pp. 65–75. https://doi.org/10.1007/978-3-7091-6703-8_5

Iversen, J.D., White, B.R., 1982. Saltation threshold on Earth, Mars and Venus. Sedimentology 29, 111–119.

Jiang, C.W., J. R. Parteli, E., Dong, Z.B., Zhang, Z.C., Qian, G.Q., Luo, W.Y., Lu, J.F., Xiao, F.J., Mei, F.M., 2022. Wind-tunnel experiments of Aeolian sand transport reveal a bimodal probability distribution function for the particle lift-off velocities. Catena (Amst) 217, 106496. https://doi.org/10.1016/j.catena.2022.106496

Jimenez, J., Moin, P., 1991. The minimal flow unit in near wall turbulence. J. Fluid. Mech 225, 213–240.

Keshavarzy, A., Ball, J.E., 1997. An analysis of the characteristics of rough bed turbulent shear stresses in an open channel, StochasficHydrology and Hydraulics. Springer-Verlag.

Kim, J., Moin, P., Moser, R., 1987. Turbulence statistics in fully developed channel flow at low Reynolds number. J. Fluid Mech 177, 133–166.

Kind, R.J., 1976. A critical examination of the requirements for model simulation of wind-induced erosion/deposition phenomena such as snow drifting. Atmospheric Environment (1967) 10, 219–227. https://doi.org/10.1016/0004-6981(76)90094-9

King, J., Nickling, W.G., Gillies, J.A., 2005. Representation of vegetation and other nonerodible elements in aeolian shear stress partitioning models for predicting transport threshold. J Geophys Res Earth Surf 110, 1–15. https://doi.org/10.1029/2004JF000281

Klose, M., Shao, Y., Li, X., Zhang, H., Ishizuka, M., Mikami, M., Leys, J.F., 2014. Further development of a parameterization for convective turbulent dust emission and evaluation based on field observations. J Geophys Res 119, 10,441-10,457. https://doi.org/10.1002/2014JD021688

Kok, J., Renno, N., 2009. A comprehensive numerical model of steady state saltation (COMSALT). Journal of Geophysical Research Atmospheres 114, 1–20. https://doi.org/10.1029/2009JD011702

Kok, J.F., Mahowald, N.M., Fratini, G., Gillies, J.A., Ishizuka, M., Leys, J.F., Mikami, M., Park, M.-S., Park, S.-U., Van Pelt, R.S., Zobeck, T.M., 2014. An improved dust emission model – Part 1: Model description and comparison against measurements. Atmos Chem Phys 14, 13023–13041. https://doi.org/10.5194/acp-14-13023-2014

Kok, L., Parteli, E., Michaels, T., Karam, D., 2012. The physics of wind-blown sand and dust. Reports on Progress in Physics 75, 106901.

Kolmogorov, A.N., 1941. The Local Structure of Turbulence in Incompressible Viscous Fluid for Very Large Reynolds Numbers. Proceedings of the Royal Society A: Mathematical, Physical and Engineering Sciences 434, 9–13. https://doi.org/10.1098/rspa.1991.0075

Leonard, A., 1974. Energy cascade in large-eddy simulations of turbulent fluid flows. Advances in Geophysics 18, 237–248. https://doi.org/10.1016/S0065-2687(08)60464-1

Li, A.N., Shao, Y., 2003. Numerical Simulation of Drag Partition Over Rough.Pdf 317–342.

Lilly, D.K., 1967. The Representation of Small-scale Turbulence in Numerical Simulation Experiments. Proceedings of the IBM Scientific Computing Symposium on Environmental Science 195.

Lilly, D.K., 1966. On the Application of the Eddy Viscosity Concept in the Inertial Sub-range of Turbulence.

Liu, B., Qu, J., Ning, D., 2018. Amplification factors to estimate wind erosion of piles of soil with different heights: Numerical simulation and structure-from-motion photogrammetry verification. J Soil Water Conserv 73, 377–385. https://doi.org/10.2489/jswc.73.4.377

Loosmore, G.A., Hunt, J.R., 2000. Below-threshold, non-abraded dust resuspension. J Geophys Res 105, ,663–20.

López, M. V, 1998. Wind erosion in agricultural soils: an example of limited supply of particles available for erosion . Catena (Amst) 33, 17–28. https://doi.org/http://dx.doi.org/10.1016/S0341-8162(98)00064-2

Lyles, L., Allison, B.E., 1975. Wind erosion: The protective role of simulated standing stubble. American Society of Agricultural Engineering 19, 61–64.

Marshall, J., Fenton, L.K., Harlow, J.J.B., 2021. Limitations of applying grain weight similitude in aeolian studies with NASA Mars Wind Tunnel. Aeolian Res 53, 100732. https://doi.org/10.1016/j.aeolia.2021.100732

Marshall, J.K., 1971a. Drag measurements in roughness arrays of varying density and distribution. Agricultural Meteorology 8, 269–292. https://doi.org/10.1016/0002-1571(71)90116-6

Marshall, J.K., 1971b. Drag measurements in roughness arrays of varying density and distribution. Agricultural Meteorology 8, 269–292. https://doi.org/10.1016/0002-1571(71)90116-6

McKenna Neuman, C., Nickling, W.G., 1995. Aeolian sediment fl ux decay: Nonlinear behaviour on developing defl ation lag surfaces. Earth Surf Process Landf 20, 423–435.

Miller, M.R., 2020. Oxidative stress and the cardiovascular effects of air pollution. Free Radic Biol Med. https://doi.org/10.1016/j.freeradbiomed.2020.01.004

Mina, M., Rezaei, M., Sameni, A., Ostovari, Y., Ritsema, C., 2022. Predicting wind erosion rate using portable wind tunnel combined with machine learning algorithms in calcareous soils, southern Iran. J Environ Manage 304, 114171. https://doi.org/10.1016/j.jenvman.2021.114171

Mingari, L.A., Collini, E.A., Folch, A., Báez, W., Bustos, E., Osores, M.S., Reckziegel, F., Alexander, P., Viramonte, J.G., 2017. Numerical simulations of windblown dust over complex terrain: The Fiambalá Basin episode in June 2015. Atmos Chem Phys 17, 6759–6778. https://doi.org/10.5194/acp-17-6759-2017

Miri, A., Dragovich, D., Dong, Z., 2017a. Vegetation morphologic and aerodynamic characteristics reduce aeolian erosion. Sci Rep 7, 1–9. https://doi.org/10.1038/s41598-017-13084-x

Miri, A., Dragovich, D., Dong, Z., 2017b. Vegetation morphologic and aerodynamic characteristics reduce aeolian erosion. Sci Rep 7, 1–9. https://doi.org/10.1038/s41598-017-13084-x

Miyagi, N., Kimura, M., Shoji, H., Saima, A., Ho, C.-M., Tung, S., Tai, Y.-C., 2000. Statistical analysis on wall shear stress of turbulent boundary layer in a channel ¯ow using micro-shear stress imager. Int J Heat Fluid Flow 21, 576–581.

Mullis, A.M., Farrell, L., Cochrane, R.F., Adkins, N.J., 2013. Estimation of cooling rates during close-coupled gas atomization using secondary dendrite arm spacing measurement. Metallurgical and Materials Transactions B: Process Metallurgy and Materials Processing Science 44, 992–999. https://doi.org/10.1007/s11663-013-9856-2

Musick, H.B., Gillette, D.A., 1990. Field evaluation of relationships between a vegetated structural parameter and sheltering against wind erosion. Land Degradation and Rehabilitation 1, 87–94.

Nascimento, E.L., 2014. Suspensão e deposição de material particulado emitido por pilhas de estocagem de granulados: umas abordagem numérica empregando LES.

Nazarenko, S., 2011. Lecture Notes in Physics Vol 825: Wave Turbulence. Lecture Notes in Physics 825. https://doi.org/10.1007/978-3-642-15942-8

Neuman, Cheryl Mckenna, W.G.N., 1995. Aeolian sediment flux decay: Non-linear behaviour on developing deflation lag surfaces. Earth Surf Process Landf 20, 423–435.

Niño, Y., Garcia, M.H., 1996. Experiments on particle-turbulence interactions in the near-wall region of an open channel flow: Implications for sediment transport. J. Fluid Mech 326, 285–319.

Onder, S., Dursun, S., 2006. Air borne heavy metal pollution of Cedruslibani (A. Rich.) in the city centre of Konya (Turkey). Atmos Environ 40, 1122–1133.

Patankar, S. V., 1980. Numerical Heat Transfer and Fluid Flow. Hemisphere Publishing Corporation, Taylor & Francis Group, New York.

Raffaele, L., van Beeck, J., Bruno, L., 2021. Wind-sand tunnel testing of surface-mounted obstacles: Similarity requirements and a case study on a Sand Mitigation Measure. Journal of Wind Engineering and Industrial Aerodynamics 214, 104653. https://doi.org/10.1016/j.jweia.2021.104653

Raupach, R., Gillette, D.A., Leys, J.F., Management, L., Wales, N.S., 1993a. The Effect of Roughness Elements on Wind Erosion Threshold 98, 3023–3029.

Raupach, R., Gillette, D.A., Leys, J.F., Management, L., Wales, N.S., 1993b. The Effect of Roughness Elements on Wind Erosion Threshold 98, 3023–3029.

Reeks, M.W., 2005. On probability density function equations for particle dispersion in a uniform shear flow. J Fluid Mech 522, 263–302. https://doi.org/10.1017/S0022112004001922

Richefeu, V., El Youssoufi, M.S., Radjaï, F., 2006. Shear strength properties of wet granular materials. Phys Rev E Stat Nonlin Soft Matter Phys 73. https://doi.org/10.1103/PhysRevE.73.051304

Rogallo, R.S., Moin, P., 1984. Numerical Simulation of Turbulent Flows. Ann. Rev. Fluid Mech 16, 99–137.

Romeo, A., Capelli, L., Sironi, S., Nano, G., Rota, R., Busini, V., 2017. Dust emission and dispersion from mineral storage piles. Environmental Science and Pollution Research 24, 22663–22672. https://doi.org/10.1007/s11356-017-9881-9

Sagaut, P., 2006. Large Eddy Simulation for Incompressible Flows – An Introduction. Springer, Berlin Heidelberg. https://doi.org/10.1108/aeat.2001.12773eae.001

Sarmiento, O.A., Falcon, M.A., 2006. Critical Bed Shear Stress for Unisize Sediment. Journal od hidraulic engineering 172–179. https://doi.org/10.1061/ASCE0733-94292006132:2172

Savage, S.B., Jeffrey, D.D.J., 1951. The stress tensor in a granular flow at high shear rates, J. Fluid Mech.

Schumann, U., 1975. Subgrid scale model for finite difference simulations of turbulent flows in plane channels and annuli. J Comput Phys 18, 376–404. https://doi.org/10.1016/0021-9991(75)90093-5

Seaton, Tran, Chen, Maynard, Whalley, 2020. Pollution, Particles, and Dementia: A Hypothetical Causative Pathway. Int J Environ Res Public Health 17, 862. https://doi.org/10.3390/ijerph17030862

Séchet, P., 2000. Contribution à l'étude des structures cohérentes en turbulence de paroi, de leur influence sur le transport des sédiments dans le cas du charriage. Institut National Polytechnique de Toulouse, France.

Shaanan, S., Ferzinger, J.H., Reynolds, W.C., 1975. Numerical simulation of turbulence in presence of shear, Rep. TF-6.

Shao, Yaping, 2008. Physics and modelling of wind erosion, 2nd ed. Springer, Cologne.

Shao, Y., 2008. Physics and modelling of wind erosion, 2nd ed. Springer.

Shao, Y., Klose, M., 2016. A note on the stochastic nature of particle cohesive force and implications to threshold friction velocity for aerodynamic dust entrainment. Aeolian Res 22, 123–125. https://doi.org/10.1016/j.aeolia.2016.08.004

Shao, Y., Lu, H., 2000. A simple expression for wind erosion threshold friction velocity. J Geophys Res 105, 437–443.

Shao, Yaping, Lu, H., 2000. A simple expression for wind erosion threshold friction velocity. J Geophys Res 105, 22437–22443. https://doi.org/https://doi.org/10.1029/2000JD900304

Shao, Y., Raupach, M.R., Findlater, P.A., 1993. On the Entrainment of Dust by Wind. J Geophys Res 98, 12719–12726.

Sherman, D.J., 2020. Understanding wind-blown sand: Six vexations. Geomorphology 366, 107193. https://doi.org/10.1016/j.geomorph.2020.107193

Sigaux, J., Biton, J., André, E., Semerano, L., Boissier, M.C., 2019. Air pollution as a determinant of rheumatoid arthritis. Joint Bone Spine 86, 37–42. https://doi.org/10.1016/j.jbspin.2018.03.001

Silveira-Neto, A., Grand, D., Métais, 0., Lesieur, M., 1993. A numerical investigation of the coherent structures of turbulence behind a backward-facing step. Int. Joumal of Fluid Mech 256, 1–25.

Smagorinsky, J., 1963. General circulation experiments with the primitive equations. Mon Weather Rev 91, 99–164.

Smith, I.B., Spiga, A., Holt, J.W., 2015. Aeolian processes as drivers of landform evolution at the South Pole of Mars. Geomorphology 240, 54–69. https://doi.org/10.1016/j.geomorph.2014.08.026

Snyder, W.H., 1972. Similarity criteria for the application of fluid models to the study of air pollution meteorology. Boundary Layer Meteorol 3, 113–134. https://doi.org/10.1007/BF00769111

Strom, G.H., Kelly, G.R., Keitz, E.L., Weiss, R.F., 1962. Scale model studies on snow drifting. Virginia.

Swet, N., Katra, I., 2016. Reduction in soil aggregation in response to dust emission processes. Geomorphology 268, 177–183. https://doi.org/10.1016/j.geomorph.2016.06.002

Tan, L., Zhang, W., Qu, J., Zhang, K., An, Z., Wang, X., 2013. Aeolian sand transport over gobi with different gravel coverages under limited sand supply: A mobile wind tunnel investigation. Aeolian Res 11, 67–74. https://doi.org/10.1016/j.aeolia.2013.10.003

Theodoor, J., Overbeek, G., 1985. Modern Trends in Colloid Science in Chemistry and Biology, Birth, life and death of colloids. Springer, Berlin.

Tiwary, A., Colls, J., 2010. Air pollution: measurement, modelling and mitigation, 3rd ed, Choice Reviews Online. Routledge Taylor and Francis Group, New York. https://doi.org/10.5860/choice.47-4447

Toraño, J.A., Rodriguez, R., Diego, I., Rivas, J.M., Pelegry, A., 2007. Influence of the pile shape on wind erosion CFD emission simulation. Appl Math Model 31, 2487–2502. https://doi.org/10.1016/j.apm.2006.10.012

Toure, A., Rajot, J.L., Garba, Z., Marticorena, B., Petit, C., Sebag, D., 2011. Impact of very low crop residues cover on wind erosion in the Sahel. Catena (Amst) 85, 205–214. https://doi.org/10.1016/j.catena.2011.01.002

Turpin, C., Badr, T., Harion, J.L., 2010a. Numerical modelling of aeolian erosion over rough surfaces. Earth Surf Process Landf 35, 1418–1429. https://doi.org/10.1002/esp.1980

Turpin, C., Badr, T., Harion, J.L., 2010b. Numerical modelling of aeolian erosion over rough surfaces. Earth Surf Process Landf 35, 1418–1429. https://doi.org/10.1002/esp.1980

Turpin, C., Harion, J.L., 2010. Effect of the topography of an industrial site on dust emissions from open storage yards. Environmental Fluid Mechanics 10, 677–690. https://doi.org/10.1007/s10652-010-9170-3

Turpin, C., Harion, J.L., 2009. Numerical modeling of flow structures over various flat-topped stockpiles height: Implications on dust emissions. Atmos Environ 43, 5579–5587. https://doi.org/10.1016/j.atmosenv.2009.07.047

USEPA, 2006a. 13.2.5 Industrial wind erosion. Compil Air Pollut Emiss Factors 1. https://doi.org/10.1130/0091-7613(1998)026<0363

USEPA, 2006b. 13.2.5 Industrial wind erosion. Compil Air Pollut Emiss Factors 1. https://doi.org/10.1130/0091-7613(1998)026<0363

Versteeg, H., Malalasekera, W., 2007. An Introduction to Computational Fluid Dynamics: The Finite Volume Method, 2nd ed. Pearson. https://doi.org/10.2514/1.22547

White, B.R., 1996. Laboratory simulation of aeolian sand transport and physical modelling. Ann Arid Zone 35, 187–213.

Woodruff, N.P., Zingg, A.W., 1953. Wind tunnel studies of shelter belt models. J. Forestry 51, 173.

Wu, D., Tie, X., Chengcai, L., Zhuming, Y., Lau, A.K.H., Huang, J., 2005. An extremely low visibility event over Guangzhou region: a study case. Atmos Environ 39, 6568–6577.

Xie, Z., Castro, I.P., 2006. LES and RANS for turbulent flow over arrays of wall-mounted obstacles. Flow Turbul Combust 76, 291–312. https://doi.org/10.1007/s10494-006-9018-6

Xie, Z.T., Coceal, O., Castro, I.P., 2008. Large-Eddy simulation of flows over random urban-like obstacles. Boundary Layer Meteorol 129, 1–23. https://doi.org/10.1007/s10546-008-9290-1

You, S., Wan, M.P., 2017. Statistical analysis of fine particle resuspension from rough surfaces by turbulent flows. Aerosol Air Qual Res 17, 843–856. https://doi.org/10.4209/aaqr.2016.03.0106

Zhang, J., Li, G., Shi, L., Huang, N., Shao, Y., 2022. Impact of turbulence on aeolian particle entrainment: results from wind-tunnel experiments. Atmos Chem Phys 22, 9525–9535. https://doi.org/10.5194/acp-22-9525-2022

Zimon, A., 1982. Adhesion of Dust and Powder. Consultants Bureau, Nwe York.

Ziskind, G., Fichman, M., Gutfinger, C., 1995. Ressuspension of particulates from surfaces to turbulent flow - Review and analysis. J. Aero. Sci 26, 613–644.

Zou, X., Li, H., Kang, L., Zhang, C., Jia, W., Gao, Y., Zhang, J., Yang, Z., Zhang, M., Xu, J., Cheng, H., Wu, X., 2022. Soil wind erosion rate on rough surfaces: A dynamical model derived from an invariant pattern of the shear-stress probability density function of the soil surface. Catena (Amst) 219. https://doi.org/10.1016/j.catena.2022.106633

Zou, X.Y., Zhang, C.L., Cheng, H., Kang, L.Q., Wu, Y.Q., 2015. Cogitation on developing a dynamic model of soil wind erosion. Sci China Earth Sci 58, 462–473. https://doi.org/10.1007/s11430-014-5002-5

APPENDIX

Additional work developed during this thesis.

Environmental Science and Pollution Research
https://doi.org/10.1007/s11356-020-10202-7

URBAN AIR QUALITY, CLIMATE AND POLLUTION: FROM MEASUREMENT TO MODELING APPLICATIONS

Check for updates

Experimental and numerical investigation of building effects on wind erosion of a granular material stockpile

Maria Clara S. Ferreira[1] · Bruno Furieri[2] · Cristina L. de Morais[2] · Jamily F. Stocco[2] · Neyval C. Reis Jr[2] · Jean-Luc Harion[3] · Jane Meri Santos[2]

Received: 25 September 2019 / Accepted: 20 July 2020

Abstract

In the present work, wind tunnel experiments and numerical simulations were carried out to evaluate the physical behaviour of the fluid flow of a stockpile in the presence of an isolated cubic building. Comparing the obtained experimental results with those for the isolated stockpile configuration and observing the differences in the erosion patterns and emission estimates was possible to conclude that (i) the emissions considerably increase due to the presence of the building; (ii) the higher the free stream velocity, due to the presence of the obstacle, the more efficient the dynamics of the pavement process; and (iii) the increase of the gap between the building and the pile does not generate expressive changes in the emitted mass measurements. These findings play an important role since it is possible to obtain an optimal industrial open yard configuration where fewer particles are emitted to the atmosphere.

Keywords Air pollution · Particulate emission control · Industrial site arrangement · Wind tunnel · CFD · Turbulent flows

Introduction

Wind erosion process can lead to several environmental consequences as desertification, land degradation, loss of material and increase of particulate concentrations to the atmosphere. The air pollution is of particular interest since it has a direct impact on human health, mainly in regions with high availability of diffuse sources such as ore and coal stored in piles on open yards of industrial units.

Wind erosion is dominated by the aerodynamic forces (drag and lift forces) that act to remove the particle from the surface and by the gravity and cohesion forces that act to restrain its movement. The aerodynamic forces are usually quantified by means of the friction velocity, u_* (square root of the ratio between wall shear stress and density), a variable characteristic of the boundary layer flow that represents the conceptual value of shear stress, τ, on the surface. The gravity and cohesion forces are considered by the threshold friction velocity (u_{*t}), which defines the minimum friction velocity in which particle movement is initiated (Shao 2008). The balance between the friction velocity and the threshold friction velocity determines a criterion (Bagnold 1941; Iversen and White 1982; Foucaut and Stanislas 1996; Shao and Lu 2000) that is used to verify if particles will take-off. If the wind friction velocity is greater than the particles threshold friction velocity ($u_* > u_{*t}$), the particles will move. These particles are known as erodible for the referred wind flow velocity. Otherwise, if the friction velocity does not trespass the threshold value ($u_* < u_{*t}$), they will be called non-erodible and they will not take-off. A very common take-off criterion used is from (Shao and Lu 2000):

$$u_{*t} = 0.11\sqrt{\frac{\rho_p - \rho}{\rho} g D + \frac{\gamma}{\rho D}} \tag{1}$$

Responsible Editor: Philippe Garrigues

✉ Bruno Furieri
bruno.furieri@ufes.br

1 Department of Mathematics, Instituto Federal do Espírito Santo, 29056-255 Vitória, ES, Brazil

2 Environmental Engineering Department, Universidade Federal do Espírito Santo, 29060-970 Vitória, ES, Brazil

3 IMT Lille-Douai, F-59500 Douai, France

Published online: 20 August 2020

Journal of the Brazilian Society of Mechanical Sciences and Engineering (2023) 45:653
https://doi.org/10.1007/s40430-023-04587-y

TECHNICAL PAPER

Wind tunnel and CFD analysis of dust re-emission potential from ground regions around successive stockpiles

B. Furieri[1] · C. L. de Morais[1] · J. M. Santos[1] · J.-L. Harion[2]

Received: 18 April 2023 / Accepted: 6 November 2023 / Published online: 30 November 2023

Abstract

Open industrial yards of granular materials can result in a large amount of particles emitted into the atmosphere due to wind erosion, offering risks to the environment and to the human health. It is important to estimate these emissions in order to manage dust control techniques and environmental polices requirements. There are several studies on particles emission from stockpiles surfaces, but there are few studies considering the re-emission that can occur from the regions around the stockpiles. Therefore, the present work aims to investigate the influence of the fluid flow complex structures near the ground region surrounding stockpiles and how they can influence the re-emission of particles. Experimental work using the oil-film technique and numerical simulations of the flow over one and two successive stockpiles oriented 30°, 60° and 90° to the incoming flow were performed. The results showed that a stockpile or successive stockpiles oriented 60° must be avoided in industrial sites as they promote high values of re-emitted mass around the piles. On the other hand, piles oriented 90° to the incoming flow showed the lowest re-emission potential for the surroundings. Finally, the gap between successive stockpiles showed insignificant influence on the emission estimates.

Keywords Computational fluid dynamics · Particulate matter · Air pollution · Steel industry

1 Introduction

Open industrial yards are widely used to storage granular material exposed to wind erosion that can cause particles emission into the atmosphere. In steel industry, for instance, large quantities of fine particulate matter of coal, iron ore and limestone are emitted from stockpiles to the atmosphere, offering risks to the environment and to human health [1–8]. To reinforce dust control techniques and environmental policies, it is necessary to estimate the amount of particles that can be emitted which depends on the local meteorology, the properties of the materials, and the way these materials are stored (shape and size of the stockpiles). The most widely used model for estimating particle emission from stockpiles in industrial sites was proposed by United Stated Environmental Protection Agency [9]. Several numerical works have been carried out in order to improve this model by refining results of the shear stress distribution (or friction velocity distribution) over the stockpile surface [10–19].

However, there is still a lack in the literature concerning the emission that occurs around the stockpiles [20]. The particles around the piles may originate from the transport of material within the industrial site [21, 22] as well as from the stockpiles wind erosion characterized as re-emission, re-entrainment or resuspension phenomenon [23–27]. Therefore, the present work aims to continue the investigation initially carried out by Furieri et al. [20] by further analyzing the influence of fluid flow complex structures generating shear stress near the ground region surrounding successive stockpiles which is a more usual arrangement in industrial yards. In addition, the influence of the stockpiles orientation (regarding the prevailing wind direction) on re-emission is also investigated.

Technical Editor: Erick Franklin.

✉ C. L. de Morais
cristinalimademorais@gmail.com

1 Department of Environmental Engineering, Universidade Federal do Espírito Santo, Vitória, ES 29075-910, Brazil

2 IMT Nord Europe Douai, 59500 Douai, France